Methods for controlling deformable mirrors with hysteresis

Kazasidis, O.

DOI
10.4233/uuid:3647c9bb-97d1-442a-9d3e-49cd1c9e3baf

Publication date
2021

Document Version
Final published version

Citation (APA)
Kazasidis, O. (2021). *Methods for controlling deformable mirrors with hysteresis*. [Dissertation (TU Delft), Delft University of Technology]. https://doi.org/10.4233/uuid:3647c9bb-97d1-442a-9d3e-49cd1c9e3baf

METHODS FOR CONTROLLING DEFORMABLE MIRRORS WITH HYSTERESIS

METHODS FOR CONTROLLING DEFORMABLE MIRRORS WITH HYSTERESIS

Dissertation

for the purpose of obtaining the degree of doctor
at Delft University of Technology
by the authority of the Rector Magnificus, Prof. dr. ir. T. H. J. J. van der Hagen,
chair of the Board for Doctorates
to be defended publicly on
Monday 1 March 2021 at 10:00 o'clock

by

Orestis KAZASIDIS

Master of Science in Photonics, FH Münster University of Applied Sciences, Germany
born in Athens, Greece

This dissertation has been approved by the promotors.

Composition of the doctoral committee:

Rector Magnificus,	chairperson
Prof. dr. ir. M. Verhaegen	Delft University of Technology, promotor
Prof. dr. rer. nat. U. Wittrock	FH Münster University of Applied Sciences, Germany, promotor

Independent members:	
Prof. dr. B. Rieger	Delft University of Technology
Prof. dr. W. M. J. M. Coene	Delft University of Technology
Prof. dr. ir. N. J. Doelman	TNO
Dr. N. Devaney	National University of Ireland Galway, Ireland

Other member:	
Prof. dr. ir. G. V. Vdovine	Delft University of Technology

FH MÜNSTER
University of Applied Sciences

Keywords: active optics, adaptive optics, wavefront sensing, hysteresis, mathematical optimization

Front: Design by the author, inspired by the drawings accompanying the essay *„Tanzkurven: Zu den Tänzen der Palucca“* by Wassily Kandinsky, Das Kunstblatt, Akademische Verlagsgesellschaft Athenaion, Potsdam, vol. 10, no. 3 (1926).

ISBN 978-94-6384-169-6

An electronic version of this dissertation is available at
http://repository.tudelft.nl/.

Τί θὰ πεῖ φῶς; Νὰ κοιτᾶς μὲ ἀθόλωτο μάτι ὅλα τὰ σκοτάδια.

Νίκος Καζαντζάκης

What is meant by light? To gaze with undimmed eyes on all darknesses.[*]

Nikos Kazantzakis

[*]Translated by Kimon Friar

CONTENTS

SUMMARY

Fast adaptive optics and comparatively slower active optics are cornerstones of modern-day astronomy. Such systems are installed on most current large ground-based observatories in the visible or infrared and are included in the design of all future observatories. Their role is twofold; first, to compensate for astronomical seeing, and second, to correct for design and manufacturing errors, as well as thermal and mechanical distortions. What's more, the science goals of future large space observatories in the visible or infrared rely on active and adaptive optics systems for reaching the required wavefront accuracy and stability, with imminent examples the folded segmented primary mirror of the James Webb Space Telescope (JWST) and the deformable mirrors of the Roman Space Telescope, previously called the Wide Field Infrared Survey Telescope (WFIRST). Besides astronomy, adaptive optics find laser applications, for aberration correction and for beam shaping.

This thesis was set to explore methods for controlling deformable mirrors with hysteresis, specifically for controlling unimorph deformable mirrors developed and manufactured at the Photonics Laboratory of the FH Münster University of Applied Sciences in Germany. The technology for manufacturing unimorph deformable mirrors has been developed in the past at the Photonics Laboratory and has been expanded in a series of industrial and research projects, both for astronomical and for laser applications. Unimorph deformable mirrors are a promising technology for adaptive and active optics systems, thanks to their paramount mechanical properties and their versatility. However, their piezoelectric actuators exhibit higher hysteresis than most other actuators. The focus of this thesis lies in accurate and precise wavefront control with unimorph deformable mirrors despite their intrinsic hysteresis.

Hysteresis can be compensated with two different approaches. In the feedforward scheme, a mathematical model of the hysteresis is constructed and its inverse model is used in open-loop to drive the deformable mirror. In the feedback scheme, the wavefront deviation – including the hysteresis influence – is measured by a wavefront sensor and the deformable mirror is controlled in closed-loop. These two approaches can be combined for optimal performance. The open-loop compensation using the Prandtl-Ishlinskii formalism has previously been implemented at the Photonics Laboratory and was found to reduce the hysteresis from 15% to about 2%. Nevertheless, the residual uncompensated hysteresis still limits the performance of optical systems that have to be almost diffraction-limited. This thesis consists of two parts that manifest the two activities carried out during this PhD project. The first is image-based aberration correction using extended scenes. This aspires to complement existing technologies for the wavefront control in future space telescopes using active optics. The second is fast defocus sensing for the implementation of a closed-loop focus-shifter, with potential application in laser micromachining.

In the first part, the feedback for controlling the unimorph deformable mirror is generated from the imaging detector. This control should correct for constant or slow-changing effects and is classified as "active optics." We designed and built a testbed to evaluate control strategies for compensating for aberrations generated in a conjugate plane. The image-based wavefront correction is designed as a blind optimization with the following configuration parameters: the merit function, the control domain, and the algorithm. We use a common image-sharpness metric as merit function and study it extensively in the domain of the Zernike modes. We show that for a severely aberrated system, the Zernike modes are not orthogonal to each other with respect to the merit function. This effect, that we call "aberration balancing," means that the performance of wavefront-free adaptive and active optics systems can be improved by adding specific low-order aberrations in the case of uncorrectable high-order aberrations, where the amount of the additional aberration depends on the power spectral density of the spatial frequencies of the object. We use this technique in simulation to show how a moon that was hidden in the halo of its planet comes into sight, by balancing secondary astigmatism 0° with astigmatism 0°; and in experiment to increase the limiting resolution of our testbed, by balancing spherical aberration with defocus.

With the knowledge of the merit function landscape, we design the control algorithm to account for valleys, plateaus and the aberration balancing. The algorithm is based on the heuristic hill climbing technique, which minimizes the influence of hysteresis. We compare image-based aberration correction in three different control domains, namely the voltage domain, the domain of the Zernike modes, and the domain of the singular modes of the deformable mirror. We demonstrate a combined control scheme that deals with the residual hysteresis left over by the open-loop compensation and with the high dimensionality of the control domains. Moreover, we experimentally show that the control in the domain of the singular modes of the deformable mirror is advantageous for the correction of random aberration in comparison to the domain of the Zernike modes.

In the second part of this thesis, the feedback for controlling the unimorph deformable mirror is generated from an additional sensor. Here, the goal is to perform fast focus control, the simplest kind of beam shaping, that falls into the category of "adaptive optics." Recently, the Photonics Laboratory presented a novel unimorph deformable mirror that allows for dynamic focus shift with an actuation rate of 2 kHz. Because of hysteresis and creep, this mirror has to be operated in closed-loop. In the past, a chromatic confocal sensor measured the displacement of the back side of the mirror and the signal was fed back to a PID controller. In the course of this PhD project, a novel defocus sensor based on an astigmatic detection system has been developed. It has a bandwidth higher than 18 kHz and meets the requirements, with high-frequency performance and noise level comparable to those of the commercial chromatic confocal sensor. This sensor can open the way towards a commercial fast focus-shifter based on this mirror, circumventing the limited bandwidth and the complexity of wavefront sensors.

SAMENVATTING

Snelle adaptieve optiek en de langzamere actieve optiek zijn de hoekstenen van de hedendaagse astronomie. Dergelijke systemen zijn geïnstalleerd op de meeste huidige grote grondgebonden observatoria in het zichtbare of infrarode licht en zijn opgenomen in het ontwerp van alle toekomstige observatoria. Hun rol is tweeledig: ten eerste, het compenseren van het astronomische seeing, en ten tweede, het corrigeren van ontwerp- en fabricagefouten, alsmede thermische en mechanische vervormingen. Bovendien zijn de wetenschappelijke doelen van toekomstige grote ruimteobservatoria in het zichtbare of infrarode licht afhankelijk van actieve en adaptieve optische systemen voor het bereiken van de vereiste nauwkeurigheid en stabiliteit van het golffront, bijvoorbeeld de gevouwen gesegmenteerde primaire spiegel van de James Webb-ruimtetelescoop (JWST) en de vervormbare spiegels van de Roman-ruimtetelescoop, die voorheen de Wide Field Infrared Survey Telescope (WFIRST) werd genoemd. Naast de astronomie, vindt de adaptieve optiek ook toepassingen bij lasers, voor aberratiecorrectie en voor bundelvorming.

Deze dissertatie had tot doel om methoden te onderzoeken voor het regelen van vervormbare spiegels met hysteresis, specifiek voor het regelen van unimorfe vervormbare spiegels die ontwikkeld en geproduceerd zijn in het Photonics Laboratory van de FH Münster University of Applied Sciences in Duitsland. De technologie voor het vervaardigen van unimorfe vervormbare spiegels is in het verleden ontwikkeld in het Photonics Laboratory en is uitgebreid in een reeks industriële en onderzoeksprojecten, zowel voor astronomische als voor lasertoepassingen. Unimorfe vervormbare spiegels zijn een veelbelovende technologie voor adaptieve en actieve optische systemen, dankzij hun zeer opperste mechanische eigenschappen en hun veelzijdigheid. Hun piëzo-elektrische actuatoren vertonen echter een hogere hysteresis dan de meeste andere actuatoren. De focus van dit proefschrift ligt op een nauwkeurige en precieze golffrontcontrole met unimorfe vervormbare spiegels ondanks hun intrinsieke hysteresis.

Hysterese kan worden gecompenseerd met twee verschillende benaderingen. In het feedforward schema wordt een wiskundig model van de hysteresis geconstrueerd en het omgekeerde model wordt in open-loop gebruikt om de vervormbare spiegel aan te drijven. In het terugkoppelingsschema wordt de golffrontafwijking – inclusief de hysterese-invloed – gemeten door een golffrontsensor en wordt de vervormbare spiegel in closed-loop aangestuurd. Deze twee benaderingen kunnen worden gecombineerd voor optimale prestaties. De open-loop compensatie met behulp van het Prandtl-Ishlinskii formalisme is eerder geïmplementeerd in het Photonics Laboratory en bleek de hysteresis te verminderen van 15% tot ongeveer 2%. De resterende niet-gecompenseerde hysteresis beperkt echter nog steeds de prestaties van optische systemen die bijna diffractie-beperkt moeten zijn. Deze thesis bestaat uit twee delen die corresponderen met de twee activiteiten die tijdens dit doctoraatsproject werden uitgevoerd. De eerste is beeldgebaseerde aberratiecorrectie met behulp van uitgebreide scènes. Hiermee wordt beoogd

de bestaande technologieën voor de golffrontcontrole in toekomstige ruimtetelescopen met behulp van actieve optiek aan te vullen. De tweede is snelle defocusdetectie voor de implementatie van een closed-loop focus-shifter, met mogelijke toepassing in de laser-micromachinebouw.

In het eerste deel wordt de terugkoppeling voor het aansturen van de unimorfe vervormbare spiegel gegenereerd door de beelddetector. Deze controle moet corrigeren voor constante of langzaam veranderende effecten en wordt geclassificeerd als "actieve optiek." We ontwierpen en bouwden een testbed om strategieën te evalueren voor het compenseren van aberraties die gegenereerd worden in een geconjugeerd vlak. De beeldgebaseerde golffrontcorrectie is ontworpen als een blinde optimalisatie met de volgende configuratieparameters: de meritefunctie, het controledomein en het algoritme. We gebruiken een gemeenschappelijke beeldscherptemaat als merit-functie en bestuderen deze uitgebreid in het domein van de Zernike modi. We tonen aan dat de Zernike-modi voor een sterk afwijkend systeem niet loodrecht op elkaar staan wat betreft de merit-functie. Dit effect, dat we "aberratiebalancering" noemen, betekent dat de prestaties van golffront-vrije adaptieve en actieve optische systemen kunnen worden verbeterd door het toevoegen van specifieke lage-orde aberraties in het geval van niet-corrigeerbare hoge-orde aberraties, waarbij de hoeveelheid van de extra aberratie afhankelijk is van de vermogensspectrale dichtheid van de ruimtelijke frequenties van het object. We gebruiken deze techniek in de simulatie om te laten zien hoe een maan die verborgen was in de halo van zijn planeet in het zicht komt, door het balanceren van secundair astigmatisme 0° met astigmatisme 0°; en in het experiment om de beperkende resolutie van ons testbed te verhogen, door het balanceren van sferische aberratie met defocus.

Met de kennis van het merite-functielandschap ontwerpen we het regelalgoritme om rekening te houden met valleien, plateaus en de aberratiebalancering. Het algoritme is gebaseerd op de heuristische hill-climbing techniek, die de invloed van hysteresis minimaliseert. We vergelijken de beeldgebaseerde aberratiecorrectie in drie verschillende controledomeinen, namelijk het spanningsdomein, het domein van de Zernike modi, en het domein van de singuliere modi van de vervormbare spiegel. We demonstreren een gecombineerd controleschema dat zich bezighoudt met de resthysteresis die overblijft door de open-loop compensatie en met de hoge dimensionaliteit van de controledomeinen. Bovendien tonen we experimenteel aan dat de controle in het domein van de singuliere modi van de vervormbare spiegel voordelig is voor de correctie van willekeurige aberratie in vergelijking met het domein van de Zernike modi.

In het tweede deel van dit proefschrift wordt de terugkoppeling voor het aansturen van de unimorfe vervormbare spiegel gegenereerd door een extra sensor. Hier is het doel om een snelle focuscontrole uit te voeren, de eenvoudigste vorm van bundelvorming, die valt in de categorie "adaptieve optiek." Onlangs presenteerde het Photonics Laboratory een nieuwe unimorfe vervormbare spiegel die een dynamische focusverschuiving met een activeringssnelheid van 2 kHz mogelijk maakt. Vanwege hysteresis en kruip moet deze spiegel in een gesloten kringloop worden bediend. In het verleden heeft een chromatische confocale sensor de verplaatsing van de achterzijde van de spiegel gemeten en werd het signaal teruggekoppeld naar een PID-regelaar. In de loop van dit doctoraatsproject is een nieuwe defocussensor ontwikkeld op basis van een astigmatisch detectiesysteem. Het heeft een bandbreedte van meer dan 18 kHz en voldoet aan de eisen,

met hoogfrequente prestaties en een ruisniveau dat vergelijkbaar is met dat van de commerciële chromatische confocale sensor. Deze sensor kan de eerste stap zijn naar een commerciële snelle focus-shifter op basis van deze spiegel, waardoor de beperkte bandbreedte en de complexiteit van golffrontsensoren wordt omzeild.

1

INTRODUCTION

Adaptive and active optics are improving astronomical imaging, allowing humans to see their place in the universe more clearly. They also find several industrial and medical applications, aiming to improve human well-being. Unimorph deformable mirrors are one of the most promising technologies in this field, thanks to their paramount mechanical properties and their versatility. However, they employ piezoelectric actuators that exhibit higher hysteresis than most other actuators. Hysteresis is not a unique characteristic of piezoelectric materials. Mechanical backlash and friction are other common examples of hysteretic behavior. The focus of this thesis lies in the reduction of hysteresis influence on adaptive and active optics systems based on unimorph deformable mirrors and in the enhancement of their performance.

This chapter introduces the basic concepts that are explored in the thesis. It starts with the historical evolution of adaptive and active optics and their present-day applications. After a short description of the Zernike modes and their role in the wavefront representation, it continues with a review of the unimorph deformable mirror technology and its hysteretic behavior. These lead to the motivation of the thesis that aims to present its scope and challenges to the reader. The chapter concludes with the organization of the thesis.

Parts of this chapter have been published in Proceedings of SPIE 10695 (2018) [1] and 11180 (2019) [2].

1

1.1. ADAPTIVE AND ACTIVE OPTICS

Hopefully, it would require only slight effort to convince anyone of the detrimental consequences of war. Death, destruction, and desperation are only a few words to characterize them. Nevertheless, governments consistently seem more eager to invest in war than in any other sector that would actually improve their citizens' quality of life. The latter does indeed come from time to time as a silver lining, after the war clouds pass over.

So starts the history of adaptive and active optics. After a relevant legend from the antiquity, this section follows the development of the technology in the 20th century and lands in the present with their most notable applications in science, medicine and industry.

1.1.1. BEGINNINGS

Archimedes is considered to have been the first to employ a primitive version of large-scale active optics. During the siege of Syracuse (3rd c. BCE), he supposedly invented an array of "burning mirrors" that destroyed enemy ships by focusing sunlight.[1] Modern scholars, though, doubt this incident [3–5]. Archimedes' technique has been subjected to scientific feasibility studies. J. Scott provided an overview until the middle of 19th century [6]. In the end of the 20th century, A. Mills and R. Clift concluded after thorough research that *the story is no more than an exaggerated myth* [7]. As much fictive as this narration may be, its very existence demonstrates that segmented mirrors were well within the conceptual frame of early scholars.

Adaptive optics bares similarities to the Space Race of the middle of the 20th century, that led to the exploration of space and the landing of the first humans on the Moon. The Space Race is often cited as a positive side effect of the Cold War between the United States of America and the Soviet Union. Adaptive optics can be seen as another offspring of this catastrophic liaison. The technology as we know it today was initially developed during the Cold War by the defense industry, which is rather an euphemism and as close to the truth as the term "Ministry of Peace."[2] In his review paper in 1978, J. Hardy presented adaptive optics[3] as a conscious human evolution [8]. Looking back, the transition from rigid optics to flexible optics seems a rational step indeed. However, it took many decades for the technology to get partially detached from the toxic environment where it was hatched and find its way to becoming a driving force for the evolution of the human species.

Every adaptive optics system comprises at least two elements: 1. a wavefront corrector, such as a deformable mirror (DM), an adaptive lens, a spatial light modulation (SLM), a digital micromirror device (DMD) or a segmented mirror, and 2. a control unit

[1] Most references originate from the early (5–6 c. CE) and middle (12th c. CE) Byzantine period. According to a preceding – rather vague – reference in *Hippias* by Lucian of Samosata (2nd c. CE), Archimedes *burned the ships of the enemy by means of his science.* English translation from ancient Greek by A. M. Harmon (London, 1913).

[2] One of the government ministries in the novel "1984" by George Orwell (Secker and Warburg, London, 1949).

[3] This term is used here anachronistically. J. Hardy actually used the term "active optics," which in that context described open-loop systems, whereas "adaptive optics" referred to closed-loop systems. As mentioned later, nowadays the distinction of the two terms is based on the operational bandwidth, rather than on the existence of feedback or not.

that calculates the required shape for the wavefront corrector. Commonly a wavefront sensor (WFS), such as a Shack–Hartmann WFS, is added as feedback element, so that the correction speed increases or the correction error is minimized.

The earliest reference to adaptive optics in the frame of a scientific problem is dated to 1953 by H. W. Babcock [9]. He proposed a mirror covered by a thin oil layer in a feedback loop with a rudimentary WFS, for compensating seeing. Atmospheric seeing was indeed the first implementation of adaptive optics systems in classified research since the mid 1960s. Publications until the declassification in 1991 were scarce, but hinted to enhancing the resolution of ground-based optical telescopes, that was limited by atmospheric turbulence [10–12]. As revealed much later, there were two main motivations [13]. First, imaging and tracking of space objects from the ground, necessary for assessing the threat from hostile satellites and for managing proper operation of friendly satellites. Another possible application was Earth-imaging from satellites, but it soon turned out that it was not limited by the atmosphere. Only recently, with increasing telescope sizes in geostationary satellites, active optics is becoming necessary to achieve the required wavefront stability. The second motivation was to achieve focusing of laser beams through the atmosphere by compensating thermal blooming. The application fields were laser communications and destruction of hostile missiles, commonly using a relay mirror in space. Although most of the classified projects related to adaptive optics were unsuccessful, they did initiate the research, by building hardware and investigating control strategies, thus addressing all key components of every current adaptive optics system.

In the 1980s, the European Southern Observatory (ESO) developed and employed the first active and adaptive optics systems in astronomical ground-based telescopes. The contemporary use of the terms “active” and “adaptive” dates back to that research. “Active optics” compensates the telescope errors, or in that sense the fixed and slow-changing errors of any optical system, with a low bandwidth up to about 2 Hz. On the other hand, “adaptive optics” compensates astronomical seeing and other errors that require higher bandwidth [14]. These terms get still commonly mixed up, with “adaptive optics” (AO) often used as a generic term to refer to all wavefront correction systems.

Until the 1980s, most optical and near-infrared ground-based telescopes were limited to primary mirrors of up to 3 – 3.6 m. It was and still is extremely troublesome to manufacture and accurately polish large monolithic mirrors. With pioneers, such as R. N. Wilson, ESO’s New Technology Telescope (NTT) in Chile became the first active telescope, with 75 actuators installed on its primary mirror [15–17]. Active optics soon became standard and was either installed on existing telescopes or incorporated in the design of new ones, with an early notable mention being the Nordic Optical Telescope in the Canary Islands [18].

Even with technological advancements, gravity imposes a fundamental limitation to the possible size of monolithic active primary mirrors. The workaround engineers found was to construct several smaller mirror segments and combine them in forming a large segmented mirror. The pieces of this puzzle have to be accurately placed relative to each other to ensure high light-gathering capability and resolution. The first two segmented telescopes were inaugurated in the W. M. Keck Observatory in Hawaii in the early 1990s

and have a diameter of 10 m. The primary mirror of each telescope comprises 36 segments, each controlled with three degrees of freedom: piston, and x and y tilts [19].

Active optics can effectively minimize the surface errors of primary mirrors. Nevertheless, much faster and accurate wavefront correction is required for compensating fast-changing aberrations and high-order modes, such as those arising from the astronomical seeing. This can be performed by a deformable mirror much smaller than the primary mirror, placed at a plane conjugate to the atmospheric turbulence layer. The small dimensions of the DM allow accurate wavefront shaping with a bandwidth dependent on its mass and stiffness. The first adaptive optics systems of a large astronomical telescope was installed on the ESO-La Silla 3.6 m telescope in Chile in 1989 as a preliminary test for the system of ESO's then-under-design Very Large Telescope (VLT) array also in Chile [20]. This first system, called COME-ON, operated in closed-loop with feedback from a Shack–Hartmann WFS and two mirrors: one tip/tilt mirror with 4 piezoelectric actuators to correct image motion and one deformable mirror with 19 piezoelectric actuators to correct aberrations [21].

Closed-loop adaptive optics systems in ground-based astronomical telescopes rely on a reference source for the wavefront estimation by a WFS. To increase the sensitivity and the control bandwidth, a bright star had to be inside the telescope field of view, which in the beginning limited the observation to certain patches of the sky [22]. This has been circumvented by employing laser beacons. These beacons create the so-called artificial guide stars, either via Rayleigh backscattering at 10–20 km altitude or by exciting the sodium layer at 90 km altitude [23], and thus allow the observation of up to 70% of the sky. The isoplanatic angle still limits the field of view to a few tens of arcseconds. Multi-Conjugate Adaptive Optics (MCAO) employs two or more deformable mirrors, each controlled by a wavefront sensor and conjugated to a different atmospheric layer [24, 25]. It thus allows to overcome anisoplanatism and reach fields of view of some arcminutes [26].

The Hubble Space Telescope (HST) that has revolutionized astronomy in the ultraviolet, visible and near-infrared since its launch in 1990 has active primary and secondary mirrors. Its 2.4-m primary mirror has 24 actuators for low-order deformation correction that have not been used [27]. These actuators could not correct for the spherical aberration caused by the polishing flaw, which was compensated for by the corrective optics space telescope axial replacement (COSTAR) instrument installed in 1993. The actuators of HST's secondary mirror are periodically used in axial motion for focus correction. Until 2006, about 20 adjustments were performed in total, ranging from 20 µm in the beginning of the mission, to 3 µm to 5 µm since 2000 [28]. After the installation of COSTAR, HST is diffraction-limited at 500 nm. At this wavelength, the Ultraviolet-Visible (UVIS) channel of its Wide Field Camera 3 (WFC3) is undersampled and reaches an angular resolution of about 80 mas.[4]

[4] Although also slightly undersampled, the High Resolution Channel (HRC) of HST's Advanced Camera for Surveys (ACS) instrument could reach an even finer angular resolution of about 50 mas. However, HRC is defect and remains off-operation since 2007 [29].

1.1.2. PRESENT AND WAY AHEAD

Nowadays, adaptive and active optics find a wide variety of imaging and laser applications. This section by no means intends to provide an exhaustive list. We shortly introduce the most prominent application fields, with emphasis on ground-based and space optical and near-infrared astronomical telescopes, and refer the reader to the literature for an extensive discussion.

IMAGING APPLICATIONS

Because of astronomical seeing, ground-based observatories could not reach a resolution better than about 500 mas without active and adaptive optics. Therefore, these technologies are indispensable for large ground-based optical and near-infrared telescopes. Active optics, such as actuated monolithic mirrors and segmented mirrors, corrects design and manufacturing errors, as well as thermal and mechanical distortions. Adaptive optics employs deformable mirrors to compensate for tracking errors and atmospheric turbulence. Artificial guide stars drive the wavefront sensors and enable closed-loop bandwidths of a few kHz. Extreme Adaptive Optics (ExAO) have allowed studying exoplanets from the ground, both by spectroscopy and by direct imaging using coronagraphic methods [30, 31].

Currently, the best resolution in the visible and near-infrared is achieved in good seeing conditions by ground-based telescopes with active monolithic primary mirrors in combination with adaptive optics systems. One of the two 6.5-m Magellan telescopes in Chile has an adaptive secondary mirror. Its AO system (MagAO) has reached diffraction-limited resolution of 19 mas at 630 nm [32]. The Gemini South Adaptive Optics Imager (GSAOI) on the Gemini Observatory in Chile with a 8.1-m primary mirror uses the Gemini Multi-Conjugate Adaptive Optics System (GeMS) and reaches an angular resolution of 40 mas at 900 nm [33]. Each of the Subaru Telescope in Hawaii and the telescopes of the Very Large Telescope (VLT) array in Chile have 8.2-m primary mirrors. The Subaru Coronagraphic Extreme Adaptive Optics (SCExAO) instrument at the Subaru Telescope combines adaptive optics with interferometric techniques and reaches sub-diffraction-limited resolution finer than 10 mas at 650 nm [34]. On the other hand, the Narrow Field Mode of the Multi Unit Spectroscopic Explorer (MUSE) instrument in the VLT works with the GALACSI adaptive optics module and reaches an angular resolution of about 50 mas at 650 nm [35].[5]

The two telescopes of the W. M. Keck Observatory in Hawaii with segmented 10-m primary mirrors combine adaptive optics and active optics and reach almost reach diffraction-limited performance of about 35 mas at 1.6 µm [37].[6] AO and MCAO systems are employed even for solar astronomy [39]. Such is the case of the Daniel K. Inouye Solar Telescope (DKIST) in Hawaii that has a 4.24-m active monolithic primary mirror and a deformable mirror with 1600 actuators to compensate for astronomical seeing with 2 kHz. DKIST's Visible Broadband Imager is diffraction-limited, with an angular resolution of 22 mas at 430 nm and 34 mas at 656 nm [40].

[5] The four main telescopes of the VLT can be combined in an interferometric mode reaching an angular resolution of about 4 mas at 2 µm [36].

[6] The interferometric mode of the Keck Observatory was operational from 2003 to 2012 and could reach an angular resolution of 5 mas at 2.2 µm [38].

The designs of all three future large ground-based telescopes, planned for first light in this decade, i.e., the Extremely Large Telescope (ELT), the Giant Magellan Telescope (GMT), and the Thirty Meter Telescope (TMT), include segmented primary mirrors and sophisticated adaptive optics, pushing towards a resolution of 10 mas in the upper part of the visible and the near-infrared, with high sensitivity, hgh contrast and wide field of view [41, 42].

Active optics is also becoming an essential feature of space telescopes to correct for manufacturing errors, gravitational release and slow drifts caused by thermo-elastic effects. Due to mass and volume constraints the lightweight segmented primary mirrors of large space telescopes will be deployed and aligned on orbit. This will be demonstrated in the forthcoming James Webb Space Telescope (JWST). Active optics will co-phase the segments of its 6.5-m primary mirror and align the optical telescope [43]. Active optics will also regularly track the telescope alignment and correct for possible errors [44]. JWST will be diffraction-limited at 2 µm. At this wavelength, the short wavelength detectors of its Near Infrared Camera (NIRCam) are slightly oversampled and will reach an angular resolution of about 70 mas [45].[7] In addition to active optics, future space observatories, such as the planned Roman Space Telescope (RST)[8] [46, 47] and the proposed Large Ultraviolet Optical Infrared Surveyor (LUVOIR) [48], will include deformable mirrors to compensate for residual wavefront aberrations that cannot be corrected in their segmented primary mirrors and achieve picometer-level wavefront stability necessary for their coronagraph instruments.

In microscopy and biomedical imaging, adaptive optics is used to correct off-axis aberrations and to compensate for aberrations induced by scattering specimens, e.g., tissue samples. It thus increases the field of view, the lateral and axial resolution, and the contrast [49–52]. Similarly, in ophthalmology, adaptive optics allows for high-resolution retinal imaging [53, 54] and seems a promising technology even for individuals with severe eye defects, such as cataract [55].

LASER APPLICATIONS

Adaptive optics has two primary laser applications: for aberration correction and for beam shaping. An early commercial use has been in optical disc systems, where a wavefront corrector based on liquid crystals compensates for aberrations caused by the disc tilt, cover layer thickness error, distorted optical elements or improper assembly of the pick-up head [56]. Deformable mirrors, adaptive lenses and spatial light modulators are used to achieve tight focus or to convert the beam to a desirable shape, such as a super-Gaussian [57, 58]. Recently, a unimorph deformable mirror has been developed that allows focus shift with an actuation rate of a few kHz [59].

The research for defense systems that would target airborne missiles by focusing a laser beam through the atmosphere continues as classified. A similar application for adaptive optics is in free-space laser communication, specifically for the uplink from Earth stations to satellites that suffers from intensity fluctuations due to scintillation,

[7] The point spread function (PSF) of JWST at wavelenghts smaller than 1.25 µm will probably be smaller than HST's. However, no finer resolution will be achieved because the PSF in the visible will be undersampled.

[8] The full name of the observatory is Nancy Grace Roman Space Telescope. As of May, 20th 2020, NASA renamed the mission after the former NASA Chief of Astronomy. Its previous name was the Wide Field Infrared Survey Telescope (WFIRST).

and for the downlink that suffers from additional phase errors [60–62]. Adaptive optics is also considered for quantum communication, e.g., for quantum key distribution [63].

Finally, adaptive optics has been suggested for intracavity compensation of thermally-induced phase aberrations in gas lasers [64] and in solid-state lasers [65]. There have been only a few actual demonstrations, such as in [66–70]. Nevertheless, this remains an active research field, since it can potentially increase the laser output power and the beam quality.

1.2. WAVEFRONT REPRESENTATION

The influence of an aberrated optical system on light propagation can be expressed as the wavefront deviation from the ideal planar or spherical shape. Mathematically this is done by altering the phase of the complex pupil function. The Zernike modes offer one of the ways to describe the wavefront. They resemble common aberrations and can accurately represent wavefronts that originate from circular pupils. This section shortly introduces the wavefront representation in Zernike modes and the Zernike notation of Wyant and Creath that is used in this thesis [71].

The Zernike modes are an infinite sequence of polynomials invented by F. Zernike [72]. They are orthogonal to each other over a unit circle with respect to the wavefront, i.e., every circular wavefront can be expressed as a unique linear superposition of Zernike modes, each weighted by a coefficient. We call Z_i the i-th Zernike mode and z_i its coefficient. Then, the wavefront in the polar coordinates (ρ, θ) is:

$$W(\rho,\theta) = \sum_{i}^{\infty} z_i Z_i(\rho,\theta)\,. \tag{1.1}$$

There exist various Zernike notations that differ in the normalization, which leads to a different constant multiplication factor for each mode. The first 13 Zernike modes in the notation of Wyant and Creath [71] are shown in table 1.1, together with their name and functional form. The first three Zernike modes are not considered as aberrations, because they do not affect the image quality. Piston (Z_0) represents a nonzero mean wavefront, and tip and tilt (Z_1 and Z_2) correspond to an image shift. Figure 1.1 shows the pupil wavefront for the low-order Zernike modes when $z_i = 1\,\lambda$, where λ is the wavelength.

Every Zernike mode has zero mean value, with the exception of Z_0. Therefore, neglecting Z_0, the wavefront variance σ_W^2 is given by the relation:

$$\sigma^2 = \overline{W^2} - \overline{W}^2 = \overline{W^2}\,, \tag{1.2}$$

where $\overline{\cdots}$ denotes the mean value. The peak-to-valley (PV) wavefront deformation in the presence of a single Zernike mode equals two times the coefficient value of that Zernike mode, i.e., $PV_{Z_i} = 2\,|z_i|$. The only exceptions are the Zernike modes with zero radial order and even azimuthal order, such as the spherical aberration (Z_8) that has a PV value of $1.5\,\lambda$, as can be seen in Fig. 1.1. In general, $PV_{Z_i,\,\text{for}\,(m=0,n\,\text{even})} = 1.5\,|z_i|$.

The Zernike modes are directly related to primary aberrations. Specifically, they originate from mixing low-order and high-order aberration modes to minimize the wavefront variance. This property is called “aberration balancing” and means that adding any Zernike mode to an aberrated wavefront can only increase its variance [73].

1

Table 1.1: The first 13 Zernike modes in polar coordinates using the notation of Wyant and Creath [71].

Index	Name	Functional form
0	Piston	$Z_0 = 1$
1	Tip (Tilt x)	$Z_1 = \rho\cos\theta$
2	Tilt (Tilt y)	$Z_2 = \rho\sin\theta$
3	Defocus	$Z_3 = 2\rho^2 - 1$
4	Astigmatism 0°	$Z_4 = \rho^2\cos(2\theta)$
5	Astigmatism 45°	$Z_5 = \rho^2\sin(2\theta)$
6	Coma x	$Z_6 = (3\rho^3 - 2\rho)\cos\theta$
7	Coma y	$Z_7 = (3\rho^3 - 2\rho)\sin\theta$
8	Spherical aberration	$Z_8 = 6\rho^4 - 6\rho^2 + 1$
9	Trefoil 0°	$Z_9 = \rho^3\cos(3\theta)$
10	Trefoil 30°	$Z_{10} = \rho^3\sin(3\theta)$
11	Secondary astigmatism 0°	$Z_{11} = (4\rho^4 - 3\rho^2)\cos(2\theta)$
12	Secondary astigmatism 45°	$Z_{12} = (4\rho^4 - 3\rho^2)\sin(2\theta)$

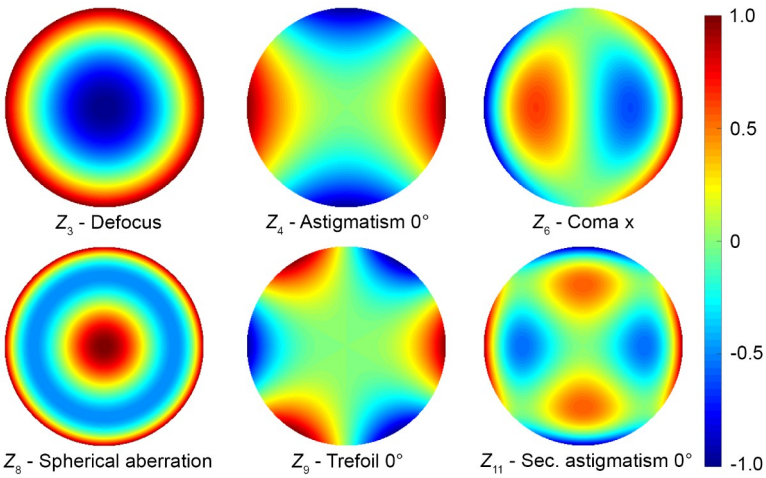

Figure 1.1: The pupil wavefront for 1 λ amplitude of the low-order Zernike modes that are used in this thesis. The common colorbar on the right is in units of λ.

The Zernike modes are ordered by increasing spatial frequency. Usually the low-order modes have higher statistical weight. Since the Zernike modes are an infinite set, a finite set is selected for computational purposes. A good compromise has to be found between accurate wavefront representation and the number of used Zernike modes. For this purpose, first the wavefront is decomposed by least squares fitting to the largest possible set of Zernike modes, e.g., the first 120 modes. Then, the wavefront variance is calculated for smaller sets of Zernike modes, by filtering out high-order modes, e.g., keeping the first 99 or 80 Zernike modes. The selected number of Zernike modes should come from the smallest set for which convergence of the wavefront variance is obtained. If the set of Zernike modes is too small, the truncation error leads to inaccurate wavefront representation. On the other hand, if the set of Zernike modes is too large, the computation becomes unnecessarily time-consuming and numerical errors may emerge.

1.3. UNIMORPH DEFORMABLE MIRRORS

Deformable is a mirror whose surface can be shaped by applying forces, that can be mechanical, piezoelectric, electromagnetic, electrostatic, or magnetostrictive. The most common types of deformable mirrors (DMs) are: membrane mirrors (with electromagnetic or electrostatic actuators, the latter can be also MEMS-based), stacked array piezoelectric mirrors, bimorph and unimorph mirrors. Among others, these types differ in mechanical properties, size and scalability, maximum actuator density and stroke, achievable actuation frequency and power-handling capability. Similar to the "no free lunch" theorem for optimization algorithms,[9] there exists no killer DM type. Each has unique characteristics that render it appropriate for specific applications.

Several companies are dedicated to the manufacturing and dealing of DMs – commonly of one or two types – and complete adaptive optics systems. Some of them, in alphabetical order, are: AKA OPTICS, ALPAO, Boston Micromachines Corporation, CILAS, Dynamic Optics, Flexible Optical B.V., and Imagine Optic.

As its title affirms, this thesis was set to explore methods for controlling deformable mirrors with hysteresis, specifically for controlling unimorph deformable mirrors developed and manufactured at the Photonics Laboratory of the FH Münster University of Applied Sciences in Germany.[10] The technology is described in detail in previous dissertations carried out at the Photonics Laboratory [75–77] and in a series of scientific publications, e.g., [78–82]. For the purposes of this thesis, we shortly describe the technology, briefly review its key parameters and kindly refer the reader to the corresponding literature.

1.3.1. DESCRIPTION AND OPERATION

Unimorph, or also called monomorph, deformable mirrors consist of one active layer, commonly a piezoelectric material. This distinguishes them from bimorph DMs that consist of two active layers. The active layer is bonded to a passive layer, that can be a glass or silicon substrate. Figure 1.2 shows a unimorph deformable mirror developed in

[9] Citing Wolpert and Macready, *for any algorithm, any elevated performance over one class of problems is offset by performance over another class* [74].

[10] Photonics Laboratory, FH Münster University of Applied Sciences, Stegerwaldstrasse 39, 48565 Steinfurt, Germany, website: www.photonics-lab.de

the Photonics Laboratory for space telescopes in the course of a project funded by the European Space Agency [81].

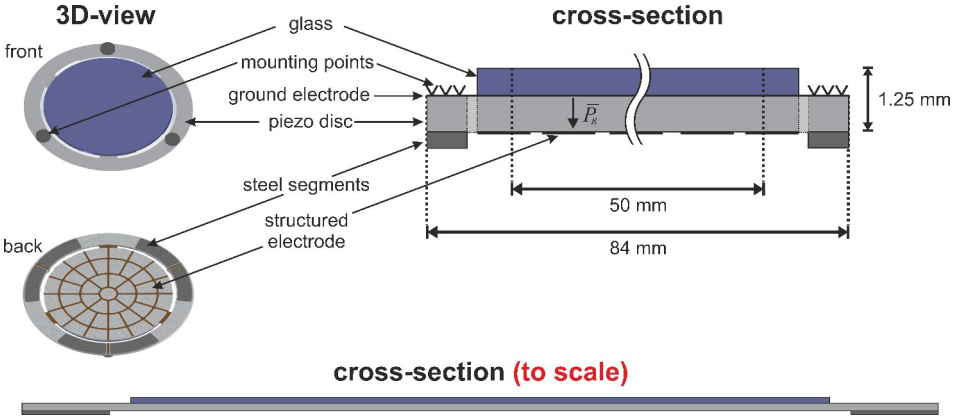

Figure 1.2: The structure of a unimorph deformable mirror. Figure adapted with permission from Rausch *et al.* [81].

A metal electrode is deposited on each side of a piezoelectric disc, which is the active layer (shown in light gray in Fig. 1.2). One side [the front side in Fig. (1.2)] serves as the common ground electrode. The other side [the back side in Fig. (1.2)] is structured with a picosecond-laser system into a keystone electrode pattern. Each electrode can be separately actuated, thus called an "actuator." The piezoelectric disc is adhesively bonded to a glass substrate (shown in dark blue), which is the passive layer. Steel segments (shown in dark gray) bonded to the back side of the piezoelectric disc act as the passive layer on the periphery of the mirror and facilitate the tip/tilt actuation.

The operational principle of the unimorph DM is based on the converse piezoelectric effect and is illustrated in Fig. 1.3. When voltage U is applied to an actuator, the electric field (shown as $\vec{E}$) polarizes the piezoelectric material. A random polarization direction is shown as $\vec{P}_R$. The applied electric field leads to strain in every direction and deformation proportional to the piezoelectric coefficient along each direction. For the radially symmetric disc, the two relevant piezoelectric coefficients are: the longitudinal d_{33} parallel to $\vec{P}_R$ (i.e., perpendicular to the disc) and the transverse d_{31} perpendicular to $\vec{P}_R$ (i.e., at the radial disc direction). Both deformations are in the range of tens of nanometers. Nevertheless, by bonding the passive layer to the active layer, the transverse deformation of the piezoelectric disc creates lateral stress between the two layers. The stress leads to a bending moment (shown as $\vec{M}$) and deformation of the unimorph structure in the order of several micrometers. The same principle is used in audio transducers and piezoelectric buzzers, and resembles the bimetal effect.

The simplest unimorph DM consists of a single electrode that covers the whole piezoelectric disc. This is shown in Fig. 1.4, for a disc with radius R. The thicknesses of the piezoelectric disc and the glass substrate are t_p and t_g, respectively. When the electrode is actuated, the mirror is deformed. In the case illustrated in Fig. 1.4, the piezoelectric disk contracts and the mirror becomes concave. Based on the thin plate theory, it is pos-

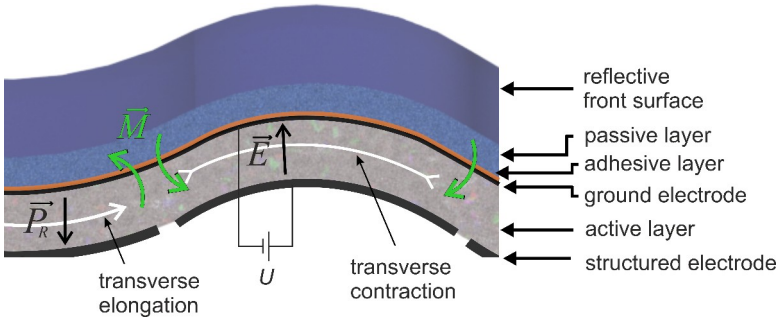

Figure 1.3: Illustration of the actuation principle for the unimorph deformable mirror. The stress in the transition between the active and the passive layer leads to deformation in the order of several micrometers. Figure adapted with permission from Rausch [77].

sible to derive an analytical model for the deflection h of the mirror center relative to its rim [76, 78]:

$$h = \frac{3\, t_p E_p t_g E_g (t_p + t_g)\, d_{31} \left|\vec{E}\right| R^2}{t_p^4 E_p^2 + 4 t_p^3 E_p t_g E_g + 6 t_p^2 E_p t_g^2 E_g + 4 t_g^3 E_g t_p E_p + t_g^4 E_g}, \tag{1.3}$$

where $\left|\vec{E}\right|$ is the electric field strength, and E_p and E_g are the moduli of elasticity of the piezoelectric disc and the glass substrate, respectively.

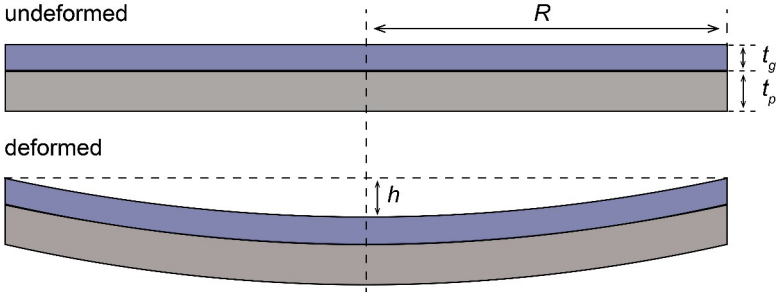

Figure 1.4: A laminate consisting of an active layer (light gray) and a passive layer (dark blue) as an example of the simplest unimorph deformable mirror. The structure is deformed when the active layer contracts or expands transversely. The deformation is exaggerated for illustration purposes.

In the DM shown in Fig. 1.2, the active layer is made of the piezoelectric material PIC 151 from PI Ceramic. The piezoelectric disc has a diameter of 84 mm and a thickness of 700 µm. The glass substrate is made of N-BK10, and has a diameter of 64 mm and a thickness of 550 µm. The ground electrode is made of silver. The backside electrode is made of aluminum and is structured in a 44-electrode keystone pattern. The pattern has been optimized to reproduce low-order Zernike modes with large amplitude in the central 50 mm aperture of the mirror [79, 81]. The glass substrate is coated with a silver highly reflective coating. The actuators are driven in the voltage range from −400 to

+400 V. The maximum deflection h of the center can be calculated by using the specific parameters for this DM: $d_{31} = -210 \cdot 10^{-12}$ C/N, $R = 25$ mm, $t_p = 700$ µm, $t_g = 550$ µm, $E_p = 63$ GPa and $E_g = 72$ GPa. By substituting these values in Eq. (1.3), we obtain $|h_{max}| = 44.7$ µm.

Due to the structured back electrode, the maximum possible deflection is smaller than the value calculated in the previous paragraph. A more accurate representation of the achievable mirror surfaces is obtained by the so-called "influence functions," that describe the mirror deformation when a single actuator is actuated. The influence functions can be numerically estimated by finite element analysis and experimentally measured by an interferometer or a wavefront sensor. The surface of the DM shown in Fig. 1.2 has been measured with a high-resolution phase-shifting interferometer. Figure 1.5 shows four influence functions for actuators in different radial positions. The measured wavefront has been fitted with 99 Zernike modes, which ensures accurate wavefront representation, as discussed in Section 1.2.

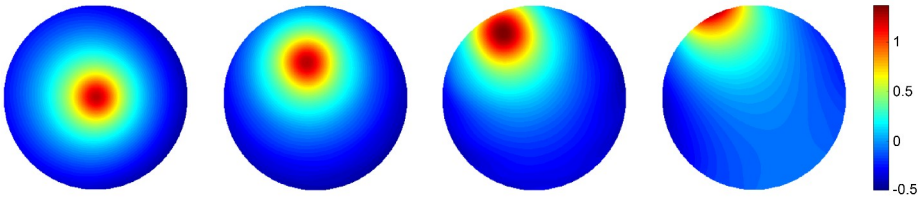

Figure 1.5: Interferometrically measured influence functions for four actuators of the deformable mirror shown in Fig. 1.2. The actuators are arranged approximately colinearly along the mirror radius. The leftmost actuator is located at the mirror center and generates primarily radially symmetric deformation. The rightmost actuator is located outside the central 50 mm aperture of the mirror. The colorbar units are µm/100 V.

1.3.2. CHARACTERISTICS AND APPLICATIONS

The technology of unimorph deformable mirrors offers a series of advantages. In principle, it is scalable to large aperture diameters. Its continuous surface leads to low diffraction losses. It has low complexity, is mechanically robust and reliable. Thanks to its actuation principle, local actuation leads to a global deformation, which is a benefit in case an actuator fails. By carefully selecting the materials and thicknesses for the active and the passive layers, large strokes are possible. In addition, these mirrors have low power consumption and heat generation. Prior to the bonding, the passive layer can be coated with highly reflective coatings, ensuring high power-handling capability. Finally, it has be proven to be compliant with space environment [81].

On the negative side, unimorph DMs are mostly suitable for the correction of low-order aberrations. As a result, any high-order initial surface deformation or print-through that originate from the manufacturing process cannot be actively corrected. Hysteresis and creep are inherent in piezoelectric materials and limit the mirror performance. Hysteresis is discussed in more detail in the next section. The actuator density cannot be increased after a certain limit, defined by the manufacturing process and the required stroke. Finally, the first resonant frequency that defines the achievable actuation fre-

quency is limited by the mirror size and the actuator stroke, and is relatively low in comparison to other DM types.

Thanks to their foremost power-handling capability, unimorph deformable mirrors are applied for intracavity aberration correction in solid-state lasers [80]. Since they can correct low-order aberrations with large stroke, they are a promising technology for active optics systems in future space applications. This potential so far has been explored by two projects funded by the European Space Agency [81–83]. Finally, by optimizing the mirror design and simplifying the electrode pattern, it has recently been demonstrated that such a mirror can provide fast focus shift for laser micromachining [59].

1.4. HYSTERESIS

The main drawback of unimorph deformable mirrors originates from hysteresis and creep. Hysteresis describes a time-independent nonlinearity and creep describes a time-dependent nonlinearity. Hysteresis appears in the thesis title, because it is the connecting point between the two experimental parts conducted in the frame of this PhD project. On the other hand, creep is neglected in the first part, but becomes important in the second part. Therefore, in this section, the focus lies in hysteresis.

Unlike electrostatic and electromagnetic actuators, piezoelectric actuators are hysteretic by nature. Hysteresis is an inherent characteristic of ferroelectric materials, caused by domain-wall switching [84]. As a result, the polarization and strain that are induced by an external electric field depend not only on the actual field strength, but also on the history, on the evolution of its value. Therefore, it is commonly said that a hysteretic system has “memory.”

Figure 1.6 shows an ideal symmetrical strain–electric field hysteresis loop [76]. The loop resembles the shape of a butterfly due to switching and movement of the domain walls [84]. As described in the previous section, the unimorph principle takes advantage of the transverse mechanical strain to deform the mirror structure. Varying the applied electric field (E) changes the strain (S) along the hysteresis loop. Following a path in Fig. 1.6, the strain value depends on the electric field history, whether it is increasing or decreasing. The unimorph deformable mirrors are operated along the designated red dashed loop, approximately in the middle of the electric field range, where the material retains a preferred polarization direction. The operating range should include neither the point where the polarization gets saturated (point 2) nor the point where the dipole moments get randomly polarized and the material has zero net polarization (point 4).

All deformable mirrors used in this thesis are based on PIC 151 from PI Ceramic [59, 81], a modified “soft” lead zirconate titanate ($Pb(Zr,Ti)O_3$ or PZT) polycrystalline material. Soft PZTs are donor-doped and have comparatively high domain mobility [84, 85]. Therefore, they can be easily polarized, which leads to large piezoelectric coefficients and large achievable strokes. On the downside, soft PZTs exhibit higher hysteresis than hard PZTs, that are acceptor-doped.

Hysteresis can be quantified as the ratio between the maximum strain difference for the same value of electric field (shown as ΔS in Fig. 1.6), and the difference of the strains for the extreme values of the electric field (the difference $S_+ - S_-$ in Fig. 1.6). Equivalently, hysteresis is observed and can be measured from the curve that connects the deflection of the mirror center with the applied voltage. Such a hysteresis loop is shown in Fig. 1.7

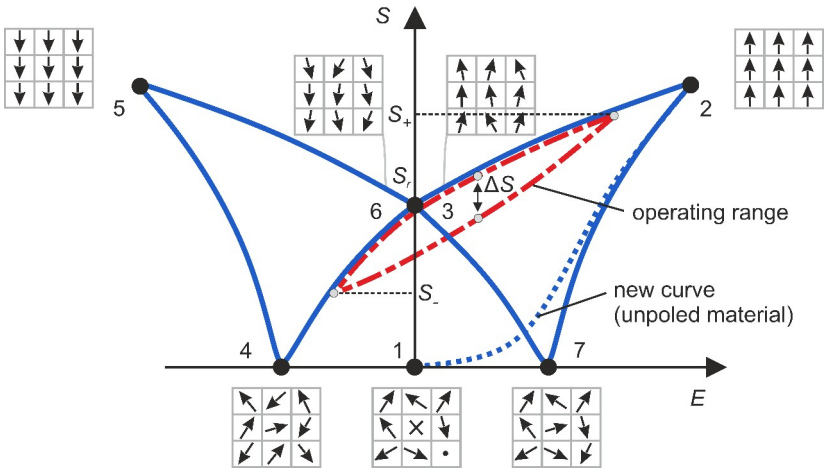

Figure 1.6: A hysteresis loop of the strain (S) relative to the electric field (E). The numbering (1, 2 ... 7) follows the applied electric field to an initially unpoled material (point 1). The insets show the evolution of the electric dipole moments. S_r is the remnant strain for zero electric field and a nonvirgin material (points 3 and 6, depending on the dominant polarization direction). The red dashed loop around point 3 shows the operating range for the unimorph DMs. ΔS is the maximum vertical opening of the loop in the operating range. S_+ and S_- are the strain values for the extreme values of the electric field in the operating range. Figure adapted with permission from Verpoort [76].

for the unimorph deformable mirror used in Chapter 5. This mirror has one central actuator that covers the whole active optical aperture of 14 mm. In this experiment, the central actuator is driven in the voltage range from −150 to +150 V and the deflection of the mirror center is measured with a chromatic confocal sensor in the range from −20 to +20 µm. Both axes have been normalized for clarity. Hysteresis for this loop is measured to be about 23%.

1.5. MOTIVATION OF THE THESIS

Hysteresis is not intrinsically harmful for a system. For example, it is positively exploited in shape-memory alloys with industrial and medical applications. In addition, magnetic hysteresis enables data storage in hard disk drives. Nevertheless, hysteretic behavior is clearly undesirable for deformable mirrors, because it complicates their control.

This thesis explores methods for accurate and precise wavefront control with unimorph deformable mirrors despite their intrinsic hysteresis. There exist two different approaches to compensate the hysteretic nonlinearity. In the feedforward scheme, a mathematical model cancels out the hysteresis in open-loop. In the feedback scheme, the deformable mirror is operated in closed-loop by using a wavefront sensor. These two approaches can be combined for optimal performance.

1.5.1. RESIDUAL FROM OPEN-LOOP COMPENSATION

Assuming hysteresis is rate-independent, i.e., it does not depend on the actuation frequency, it can be modeled by elementary units called hysteresis operators [86]. Such

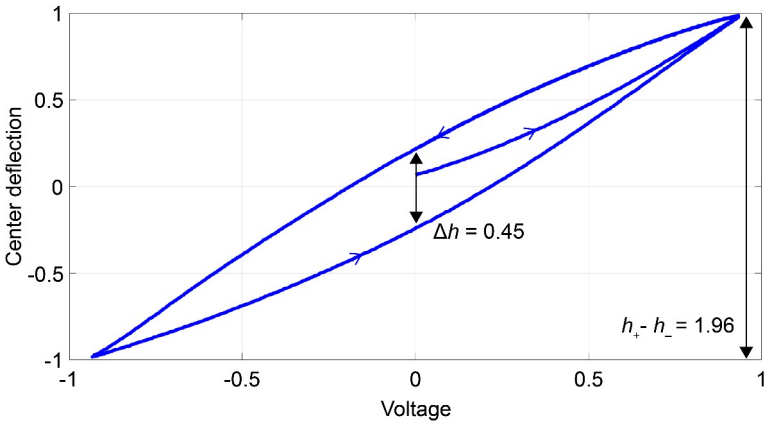

Figure 1.7: A typical center deflection-voltage hysteresis loop for a unimorph deformable mirror made with PIC 151 from PI Ceramic. The axes are normalized to the maximum deflection and the maximum applied voltage. The hysteresis measured at the loop opening for 0 V is $\Delta h/(h_+ - h_-) \approx 23\%$.

operators are used in Preisach and Prandtl-Ishlinskii formalisms. Previous work in the Photonics Laboratory [77] has modeled the hysteresis of the unimorph deformable mirrors with Prandtl-Ishlinskii operators [87, 88], by using measurements of the influence functions for different voltage values. Then, the inverse hysteresis model is applied in open-loop, combined in series with the controller, as shown in Fig. 1.8. In this figure, $\vec{W}_{\text{des}}$ represents the desired mirror shape and $\vec{u}_{\text{in}}$ the voltage vector applied to the mirror actuators. The controller calculates the voltage vector that would be necessary, if the deformable mirror were a linear system. The inverse hysteresis model H^{-1} cancels out the hysteretic nonlinearity of the DM. The saturation unit in-between ensures that all actuator voltages remain inside the operating range. $\vec{W}_{\text{real}}$ is the real mirror shape.

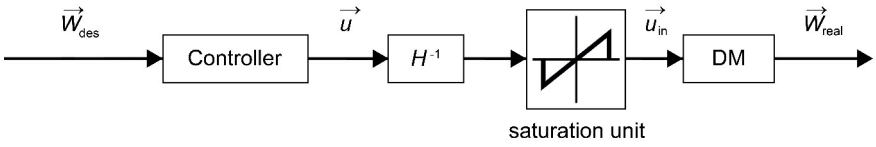

Figure 1.8: Block diagram for compensating hysteresis in open-loop using the inverse hysteresis model H^{-1}. This is a generic approach to controlling rate-independent hysteresis in a static or quasi-static manner.

Such open-loop prefiltering used in the Photonics Laboratory has been proven to reduce the hysteresis from 15% to about 2% [77]. In June 2020, Bos *et al.* reported an electromagnetically actuated DM with a hysteresis of less than 1% [89]. Nevertheless, the residual uncompensated hysteresis still limits the performance of optical systems that have to be almost diffraction-limited.

The first goal of this thesis is to apply image-based feedback control to minimize the residual hysteresis. In contrast to wavefront-based control, wavefront-free control tries to minimize the influence of wavefront aberrations on the optical performance and

does not try to minimize the aberrations *per se*. Wavefront-free and model-free control is a blind optimization, where an algorithm iteratively adapts the surface of the wavefront corrector with the goal to optimize a merit function that evaluates the system performance. Wavefront-free and model-free adaptive optics has been presented for microscopy [52], optical coherence tomography [90], and ophthalmoscopy [91, 92], using a deformable mirror as wavefront corrector.

The term "model-free" is used to distinguish such methods from "model-based" methods which require a model of the optical system. The Electric Field Conjugation (EFC) algorithm of the Roman Space Telescope's[11] coronagraph is a wavefront-free model-based method, because it uses a numerical model of the coronagraph to calculate the DM signals [93, 94]. Several model-based adaptive optics systems have been proposed for imaging [50, 95, 96]. Model-based control is expected to require a few iterations, due to imperfect calibration, modeling errors, and operational drifts. On the other hand, model-free control is inherently iterative, but needs no prior knowledge of the system. Therefore, it is widely applicable for any optical system, if appropriately tuned.

Apart from the residual hysteresis, such control can be beneficial for compensating for any aberration caused by modeling errors and uncertainties. For example, the hysteresis model mentioned before will not be accurate when the conditions change (e.g., temperature, pressure). Finally, even aging and polarization fatigue are expected to deteriorate the long-term performance of active optics based on piezoelectric actuators [84].

The Gaia satellite launched in 2013 uses the Cramér-Rao image-sharpness metric as an on-board diagnostic tool [97]. The wavefront is measured by two Shack-Hartmann sensors [98] and the focus is adjusted with five degrees of freedom (three translations and two rotations) on each secondary mirror of the two main telescopes. The Cramér-Rao image-sharpness metric has been proven to accurately monitor the focus evolution after launch, following the in-orbit alignment, which corrected for launch vibrations and gravity release, and two focus corrections [99]. Image quality criteria have also been considered to model the point spread function (PSF) of the forthcoming James Webb Space Telescope [100]. This thesis explores the potential and the limitations of using such metrics for the feedback control of active optics based on a unimorph deformable mirror.

1.5.2. CLOSED-LOOP CONTROL

In the previous section, hysteresis was assumed to be rate-independent and quasi-static. When the actuation frequency of any system increases, it gives rise to rate-dependent phenomena. Then, a static or quasi-static model may no longer be accurate. In this case, feedback control becomes essential for canceling out modeling errors and dynamics, with a subsequent reduction in operational bandwidth.

Figure 1.9 is a modification of Fig. 1.8, with the addition of a wavefront sensor that detects the real shape of the deformable mirror and feeds it back to the controller. The inverse hysteresis model from the open-loop control is complementarily used to increase the control bandwidth.

[11] The shortened name of NASA's Nancy Grace Roman Space Telescope, formerly known as the Wide Field Infrared Survey Telescope (WFIRST), planned for launch in the mid 2020s.

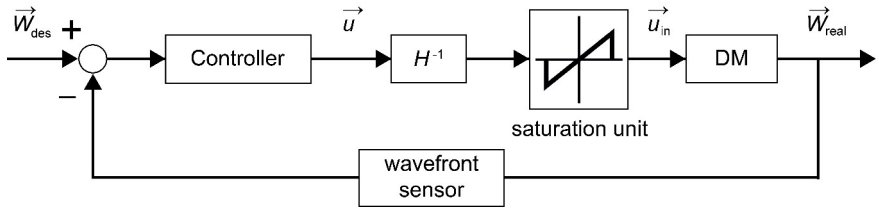

Figure 1.9: Modification of Fig. 1.8, with the addition of a feedback loop. This implementation increases the convergence speed and reduces the steady state error. The controller in this feedback scheme differs from that of the feedforward scheme of Fig. 1.8.

The bottleneck for the closed-loop bandwidth of adaptive optics systems often lies in the wavefront sensor. The bandwidth of wavefront sensors is limited by the readout time and the calculation time, i.e., the estimation of the wavefront from the captured image. Wavefront sensors use CCD (charge-coupled device) or CMOS (complementary metal oxide semiconductor) detectors, arrays of silicon (Si) or indium gallium arsenide (InGaAs) photodiodes, or other special detector types (e.g., EMCCD and sCMOS). Acquisition frequencies can reach 31.8 kHz for Shack–Hartmann WFSs with a small number of subapertures [101]. State-of-the-art adaptive optics for ground-based telescopes using pyramid WFSs push towards closed-loop operation of 4 kHz [102]. On the other hand, autofocus (AF) in microscopy and machine vision is sometimes performed with adaptive lenses in open-loop or more rarely in closed-loop [103, 104]. Multi-point AF control in commercial cameras with phase detection and contrast detection reaches up to 50 Hz acquisition speed [105].

Recently, a unimorph deformable mirror has been developed by the Photonics Laboratory that allows for dynamic focus shift with an actuation rate of a few kHz [59]. Because of hysteresis and creep, this DM has to be operated in closed-loop. Previously, a chromatic confocal sensor measured the deflection of the back side of the mirror with 66 kHz and fed it back to a controller [59]. In the course of this thesis, a novel defocus sensor has been developed that can open the way towards a commercial fast focus-shifter based on this mirror, circumventing the limited bandwidth and the complexity of wavefront sensors.

1.6. ORGANIZATION AND OUTLINE OF THE THESIS

This thesis is divided into two parts that manifest the two activities carried out during this PhD project. The first is the case of image-based aberration correction using extended scenes. This aspires to complement existing technologies for the wavefront control in future space telescopes using active optics. The second is fast defocus sensing for the implementation of a closed-loop focus-shifter, with potential application in laser micromachining.

Both activities share the common of controlling a unimorph deformable mirror. Nevertheless, the feedback for the first comes from the actual imaging detector, whereas the second requires an additional sensor. The two activities also differ in the bandwidth. The first should correct for constant or slow-changing effects and is classified as “active

optics." The second concerns fast focus control, the simplest kind of beam shaping, that falls into the category of "adaptive optics."

1.6.1. EXTENDED-IMAGE-BASED ABERRATION CORRECTION

It is often desirable to state the performance of an optical system by a single number. This immediately allows ranking of different optical systems, optimization of an optical system during its design, or finding the optimum state of an active or adaptive optics system. Examples of performance metrics that deliver a single numerical value are the Strehl ratio (S), the wavefront variance (σ^2), and image-sharpness metrics. Examples of performance metrics that deliver more than a single number, and thus contain more information, are the point spread function (PSF), the modulation transfer function (MTF), wavefront maps, and spot diagrams.

Since all single-number performance metrics lack detailed information about the performance of an optical system, the question arises, which single-number metric is most suitable for a certain imaging scene (e.g., for Earth observation, typical imaging applications are urban areas, forests, and maritime surveillance) and for a certain task (e.g. tracking fast moving objects), and what its limitations are. An image-based metric can be applied in different image regions and thus achieve optimal performance for different field angles. For example, when trying to resolve a double star, the region of interest will be a small region of the image. Thus, active optics should correct a narrow field of view. On the other hand, when observing star clusters and nebulas, a larger image region should be corrected, and the correction via active optics should be balanced over a wide field of view.

The first part of this thesis addresses the case of a deformable mirror in a conjugate plane of the primary mirror in a future large space telescope. A testbed was designed and built to test control strategies for a unimorph deformable mirror that compensates for aberrations generated in a conjugate plane. A considerable amount of time was invested in optimizing the testbed and selecting the appropriate illumination technique and reference object.

The image-based wavefront correction is designed as a blind optimization of a merit function that evaluates the quality of the image obtained from the science camera. The configuration parameters for the correction are: 1. the merit function, 2. the control domain, and 3. the algorithm. The selection for these three parameters is discussed. In addition, a comparison for the control in different control domains is performed. It is proven that the Zernike modes are not orthogonal to each other with respect to a common image-sharpness metric when the aberrations are more than about $\lambda/8$ RMS. Nevertheless, such a metric can be applied for aberration balancing, improving the performance of wavefront-free adaptive and active optics systems by adding specific low-order aberrations in the case of uncorrectable high-order aberrations.

CHAPTER 2

With a view to the next generation of large space telescopes, we investigate guide-star-free, image-based aberration correction using a unimorph deformable mirror in a plane conjugate to the primary mirror. For this purpose, we designed a high-resolution imaging testbed to evaluate control algorithms. In this chapter, we describe the testbed de-

sign and the control of the deformable mirror in three different control domains, and we introduce the used merit function.

This chapter is based on the following publication:
O. Kazasidis, S. Verpoort, O. Soloviev, G. Vdovin, M. Verhaegen, and U. Wittrock, *Extended-image-based correction of aberrations using a deformable mirror with hysteresis*, Optics Express **26**, 27161–27178 (2018) [106].

CHAPTER 3

Image-sharpness metrics can be used to optimize optical systems and to control wavefront-free adaptive optics systems. We show that for an aberrated system the numerical value of an image-sharpness metric can be improved by adding specific aberrations. The optimum amplitudes of the additional aberrations depend on the power spectral density of the spatial frequencies of the object.

This chapter is based on the following publications:
O. Kazasidis, S. Verpoort, and U. Wittrock, *Aberration balancing using an image-sharpness metric*, Journal of the Optical Society of America A **36**, 1418–1422 (2019) [107].
O. Kazasidis, S. Verpoort, and U. Wittrock, *Algorithm design for image-based wavefront control without wavefront sensing*, Proceedings of SPIE **10695**, Optical Instrument Science, Technology 1069502 (2018) [1].

CHAPTER 4

We use an algorithm based on the heuristic hill climbing technique and compare image-based aberration correction in three different domains, namely the voltage domain, the domain of the Zernike modes, and the domain of the singular modes of the deformable mirror. Through our systematic experimental study, we found that successive control in two domains effectively counteracts uncompensated hysteresis of the deformable mirror.

This chapter is based on the following publications:
O. Kazasidis, S. Verpoort, and U. Wittrock, *Algorithm design for image-based wavefront control without wavefront sensing*, Proceedings of SPIE **10695**, Optical Instrument Science, Technology 1069502 (2018) [1].
O. Kazasidis, S. Verpoort, O. Soloviev, G. Vdovin, M. Verhaegen, and U. Wittrock, *Extended-image-based correction of aberrations using a deformable mirror with hysteresis*, Optics Express **26**, 27161–27178 (2018) [106].

1.6.2. SENSOR FOR DYNAMIC FOCUS CONTROL

The second part of this thesis presents the design and manufacturing of a defocus sensor that can be used for fast focus shift in industrial applications, e.g. laser micromachining. Although the main focus of this thesis is on hysteresis, closed-loop operation of adaptive optics systems, such as in Chapter 5, accounts also for creep and mirror dynamics.

CHAPTER 5

The Photonics Laboratory recently presented a novel unimorph deformable mirror that allows for dynamic focus shift with an actuation rate of 2 kHz. Such mirrors suffer from hysteresis and creep. Therefore, they have to be operated in closed-loop. For this purpose, we developed a defocus sensor, based on an astigmatic detection system. In this chapter, we present the sensor design and discuss its performance.

This chapter is based on the following publication:
O. Kazasidis, S. Verpoort, and U. Wittrock, *Sensor for dynamic focus control of a deformable mirror*, Applied Optics **59**, 5625 (2020) [108].

REFERENCES

[1] O. Kazasidis, S. Verpoort, and U. Wittrock, *Algorithm design for image-based wavefront control without wavefront sensing*, in *Optical Instrument Science, Technology, and Applications*, Vol. 10695, edited by N. Haverkamp and R. N. Youngworth, International Society for Optics and Photonics (SPIE, 2018) pp. 1 – 10.

[2] O. Kazasidis, S. Verpoort, and U. Wittrock, *Image-based wavefront correction for space telescopes*, in *International Conference on Space Optics — ICSO 2018*, Vol. 11180, edited by Z. Sodnik, N. Karafolas, and B. Cugny, International Society for Optics and Photonics (SPIE, 2019) pp. 2854 – 2866.

[3] D. L. Simms, *The Legend of Archimedes and the Burning Mirrors of Syracuse*, Fire Research Notes **576** (1964).

[4] T. W. Africa, *Archimedes through the Looking-Glass*, The Classical World **68**, 305 (1975).

[5] D. L. Simms, *Archimedes and the Burning Mirrors of Syracuse*, Technology and Culture **18**, 1 (1977).

[6] J. Scott, *IV.—On the Burning Mirrors of Archimedes, with some Propositions relating to the concentration of Light produced by Reflectors of different forms*, Transactions of the Royal Society of Edinburgh **25**, 123–149 (1868).

[7] A. A. Mills and R. Clift, *Reflections of the 'Burning mirrors of Archimedes'. With a consideration of the geometry and intensity of sunlight reflected from plane mirrors*, European Journal of Physics **13**, 268 (1992).

[8] J. W. Hardy, *Active optics: A new technology for the control of light*, Proceedings of the IEEE **66**, 651 (1978).

[9] H. W. Babcock, *The possibility of compensating astronomical seeing*, Publications of the Astronomical Society of the Pacific **65**, 229 (1953).

[10] R. A. Muller and A. Buffington, *Real-time correction of atmospherically degraded telescope images through image sharpening*, Journal of the Optical Society of America **64**, 1200 (1974).

[11] J. W. Hardy, J. Feinleib, and J. C. Wyant, *Real time phase correction of optical imaging systems*, (1974) topical Meeting on Optical Propagation through Turbulence.

[12] J. W. Hardy, J. E. Lefebvre, and C. L. Koliopoulos, *Real-time atmospheric compensation*, Journal of the Optical Society of America **67**, 360 (1977).

[13] R. W. Duffner, *The Adaptive Optics Revolution: A History* (University of New Mexico Press, Albuquerque, 2009).

[14] R. Wilson, F. Franza, and L. Noethe, *Active Optics I. A system for optimizing the optical quality and reducing the costs of large telescopes*, Journal of Modern Optics **34**, 485 (1987).

[15] L. Noethe, F. Franza, P. Giordano, R. N. Wilson, O. Citterio, G. Conti, and E. Mattaini, *Active Optics II. Results of an experiment with a thin 1 m test mirror,* Journal of Modern Optics **35**, 1427 (1988).

[16] R. N. Wilson, F. Franza, P. Gioroano, L. Noethe, and M. Tarenghi, *Active Optics: the NTT and the Future,* ESO Messenger **53**, 1 (1988).

[17] R. N. Wilson, *"First Light" in the NTT,* ESO Messenger **56**, 1 (1989).

[18] T. Andersen, O. B. Larsen, M. Owner-Petersen, and K. Steenberg, *Active Optics on the Nordic Optical Telescope,* in *European Southern Observatory Conference and Workshop Proceedings*, European Southern Observatory Conference and Workshop Proceedings, Vol. 42 (1992) p. 311.

[19] R. C. Jared, A. A. Arthur, S. Andreae, A. K. Biocca, R. W. Cohen, J. M. Fuertes, J. Franck, G. Gabor, J. Llacer, T. S. Mast, J. D. Meng, T. L. Merrick, R. H. Minor, J. T. Nelson, M. Orayani, P. Salz, B. A. Schaefer, and C. Witebsky, *W. M. Keck Telescope segmented primary mirror active control system,* in *Advanced Technology Optical Telescopes IV*, Vol. 1236, edited by L. D. Barr, International Society for Optics and Photonics (SPIE, 1990) pp. 996 – 1008.

[20] F. Merkle, P. Kern, P. Léna, F. Rigaut, J. C. Fontanella, G. Rousset, C. Boyer, J. P. Gaffard, and P. Jagourel, *Successful tests of adaptive optics,* ESO Messenger **58**, 1 (1989).

[21] G. Rousset, J.-C. Fontanella, P. Y. Kern, P. J. Lena, P. Gigan, F. J. Rigaut, J.-P. Gaffard, C. Boyer, P. Jagourel, and F. Merkle, *Adaptive optics prototype system for infrared astronomy: I. System description,* in *Amplitude and Intensity Spatial Interferometry*, Vol. 1237, edited by J. B. Breckinridge, International Society for Optics and Photonics (SPIE, 1990) pp. 336 – 344.

[22] C. A. Primmerman, D. V. Murphy, D. A. Page, B. G. Zollars, and H. T. Barclay, *Compensation of atmospheric optical distortion using a synthetic beacon,* Nature **353**, 141 (1991).

[23] F. Roddier, *Adaptive Optics in Astronomy*, 3rd ed. (Cambridge University Press, United Kingdom, 2004).

[24] R. H. Dicke, *Phase-contrast detection of telescope seeing errors and their correction,* Astrophysical Journal **198**, 605 (1975).

[25] J. M. Beckers, *Detailed Compensation Of Atmospheric Seeing Using Multiconjugate Adaptive Optics,* in *Active Telescope Systems*, Vol. 1114, edited by F. J. Roddier, International Society for Optics and Photonics (SPIE, 1989) pp. 215 – 219.

[26] R. Ragazzoni, E. Marchetti, and G. Valente, *Adaptive-optics corrections available for the whole sky,* Nature **403**, 54 (2000).

[27] M. D. Lallo, *Experience with the Hubble Space Telescope: 20 years of an archetype,* Optical Engineering **51**, 011011 (2012).

[28] M. D. Lallo, R. B. Makidon, S. Casertano, and J. E. Krist, *Temporal optical behavior of HST: focus, coma, and astigmatism history,* in *Observatory Operations: Strategies, Processes, and Systems*, Vol. 6270, edited by D. R. Silva and R. E. Doxsey, International Society for Optics and Photonics (SPIE, 2006) pp. 527 – 538.

[29] NASA, *Hubble Space Telescope – Advanced Camera for Surveys,* [Online] https://www.nasa.gov/content/hubble-space-telescope-advanced-camera-for-surveys (2017), Last accessed August 21, 2020.

[30] A. Z. Greenbaum, A. Sivaramakrishnan, L. Pueyo, P. Ingraham, S. Thomas, S. Wolff, M. D. Perrin, B. Norris, and P. G. Tuthill, *Wavelength calibration and closure phases with the Gemini Planet Imager IFS using its non-redundant mask,* in *Techniques and Instrumentation for Detection of Exoplanets VI*, Vol. 8864, edited by S. Shaklan, International Society for Optics and Photonics (SPIE, 2013) pp. 671 – 685.

[31] O. Guyon, *Extreme Adaptive Optics,* Annual Review of Astronomy and Astrophysics **56**, 315 (2018).

[32] L. M. Close, J. R. Males, K. Morzinski, D. Kopon, K. Follette, T. J. Rodigas, P. Hinz, Y.-L. Wu, A. Puglisi, S. Esposito, A. Riccardi, E. Pinna, M. Xompero, R. Briguglio, A. Uomoto, and T. Hare, *Diffraction-limited Visible Light Images of Orion Trapezium Cluster with the Magellan Adaptive Secondary Adaptive Optics System (MagAO),* The Astrophysical Journal **774**, 94 (2013).

[33] E. R. Carrasco, M. L. Edwards, P. J. McGregor, C. Winge, P. J. Young, M. C. Doolan, J. van Harmelen, F. J. Rigaut, B. Neichel, G. Trancho, E. Artigau, P. Pessev, F. Colazo, J. Tigner, F. Mauro, J. Lührs, and W. N. Rambold, *Results from the commissioning of the Gemini South Adaptive Optics Imager (GSAOI) at Gemini South Observatory,* in *Adaptive Optics Systems III*, Vol. 8447, edited by B. L. Ellerbroek, E. Marchetti, and J.-P. Véran, International Society for Optics and Photonics (SPIE, 2012) pp. 213 – 230.

[34] N. Jovanovic, F. Martinache, O. Guyon, C. Clergeon, G. Singh, T. Kudo, V. Garrel, K. Newman, D. Doughty, J. Lozi, J. Males, Y. Minowa, Y. Hayano, N. Takato, J. Morino, J. Kuhn, E. Serabyn, B. Norris, P. Tuthill, G. Schworer, P. Stewart, L. Close, E. Huby, G. Perrin, S. Lacour, L. Gauchet, S. Vievard, N. Murakami, F. Oshiyama, N. Baba, T. Matsuo, J. Nishikawa, M. Tamura, O. Lai, F. Marchis, G. Duchene, T. Kotani, and J. Woillez, *The Subaru Coronagraphic Extreme Adaptive Optics System: Enabling High-Contrast Imaging on Solar-System Scales,* Publications of the Astronomical Society of the Pacific **127**, 890 (2015).

[35] ESO, *GALACSI,* [Online] https://www.eso.org/sci/facilities/develop/ao/sys/galacsi.html (2017), Last accessed August 21, 2020.

[36] ESO, *GRAVITY,* [Online] https://www.eso.org/sci/facilities/paranal/instruments/gravity.html (2018), Last accessed August 21, 2020.

[37] M. A. van Dam, D. L. Mignant, and B. A. Macintosh, *Performance of the keck observatory adaptive-optics system,* Applied Optics **43**, 5458 (2004).

[38] J.-U. Pott, J. Woillez, R. L. Akeson, B. Berkey, M. M. Colavita, A. Cooper, J. A. Eisner, A. M. Ghez, J. R. Graham, L. Hillenbrand, M. Hrynewych, D. Medeiros, R. Millan-Gabet, J. Monnier, D. Morrison, T. Panteleeva, E. Quataert, B. Randolph, B. Smith, K. Summers, K. Tsubota, C. Tyau, N. Weinberg, E. Wetherell, and P. L. Wizinowich, *Astrometry with the Keck Interferometer: The ASTRA project and its science,* New Astronomy Reviews **53**, 363 (2009).

[39] D. Schmidt, J. Marino, N. Gorceix, T. Rimmele, L. Johnson, T. Berkefeld, and P. Goode, *From Clear to DKIST: advancing solar MCAO from 1.6 to 4 meters,* in *Adaptive Optics Systems VI*, Vol. 10703, edited by L. M. Close, L. Schreiber, and D. Schmidt, International Society for Optics and Photonics (SPIE, 2018) pp. 716 – 724.

[40] National Solar Observatory (NSO), *Visible Broadband Imager,* [Online] https://www.nso.edu/telescopes/dkist/instruments/vbi/ (2020), Last accessed August 21, 2020.

[41] O. Guyon, F. Martinache, E. J. Cady, R. Belikov, K. Balasubramanian, D. Wilson, C. S. Clergeon, and M. Mateen, *How ELTs will acquire the first spectra of rocky habitable planets,* in *Adaptive Optics Systems III*, Vol. 8447, edited by B. L. Ellerbroek, E. Marchetti, and J.-P. Véran, International Society for Optics and Photonics (SPIE, 2012) pp. 703 – 715.

[42] S. Hippler, *Adaptive Optics for Extremely Large Telescopes,* Journal of Astronomical Instrumentation **08**, 1950001 (2019).

[43] P. A. Lightsey, D. S. Acton, J. S. Knight, and A. Contos, *James Webb Space Telescope first light boresight to spacecraft alignment determination,* in *Space Telescopes and Instrumentation 2012: Optical, Infrared, and Millimeter Wave*, Vol. 8442, edited by M. C. Clampin, G. G. Fazio, H. A. MacEwen, and J. M. Oschmann Jr., International Society for Optics and Photonics (SPIE, 2012) pp. 1232 – 1238.

[44] D. S. Acton, J. S. Knight, A. Contos, S. Grimaldi, J. Terry, P. Lightsey, A. Barto, B. League, B. Dean, J. S. Smith, C. Bowers, D. Aronstein, L. Feinberg, W. Hayden, T. Comeau, R. Soummer, E. Elliott, M. Perrin, and C. W. Starr Jr., *Wavefront sensing and controls for the James Webb Space Telescope,* in *Space Telescopes and Instrumentation 2012: Optical, Infrared, and Millimeter Wave*, Vol. 8442, edited by M. C. Clampin, G. G. Fazio, H. A. MacEwen, and J. M. Oschmann Jr., International Society for Optics and Photonics (SPIE, 2012) pp. 877 – 887.

[45] S. N. Milam, J. A. Stansberry, G. Sonneborn, and C. Thomas, *The James Webb Space Telescope's Plan for Operations and Instrument Capabilities for Observations in the Solar System,* Publications of the Astronomical Society of the Pacific **128**, 018001 (2016).

[46] J. T. Trauger, D. C. Moody, J. E. Krist, and B. L. Gordon, *Hybrid Lyot coronagraph for WFIRST-AFTA: coronagraph design and performance metrics,* Journal of Astronomical Telescopes, Instruments, and Systems **2**, 011013 (2016).

[47] F. Shi, K. Balasubramanian, R. Hein, R. Lam, D. Moore, J. Moore, K. Patterson, I. Poberezhskiy, J. Shields, E. Sidick, H. Tang, T. Truong, J. K. Wallace, X. Wang, and D. Wilson, *Low-order wavefront sensing and control for WFIRST-AFTA coronagraph,* Journal of Astronomical Telescopes, Instruments, and Systems **2**, 011021 (2016).

[48] The LUVOIR Team, *The LUVOIR Mission Concept Study Final Report,* [Online] https://asd.gsfc.nasa.gov/luvoir/reports (2019), Last accessed August 21, 2020.

[49] B. Potsaid, Y. Bellouard, and J. T. Wen, *Adaptive Scanning Optical Microscope (ASOM): A multidisciplinary optical microscope design for large field of view and high resolution imaging,* Optics Express **13**, 6504 (2005).

[50] M. J. Booth, *Adaptive optics in microscopy,* Philosophical Transactions of the Royal Society A: Mathematical, Physical and Engineering Sciences **365**, 2829 (2007).

[51] S. Bonora, Y. Jian, P. Zhang, A. Zam, E. N. Pugh, R. J. Zawadzki, and M. V. Sarunic, *Wavefront correction and high-resolution in vivo oct imaging with an objective integrated multi-actuator adaptive lens,* Optics Express **23**, 21931 (2015).

[52] J. Li, D. R. Beaulieu, H. Paudel, R. Barankov, T. G. Bifano, and J. Mertz, *Conjugate adaptive optics in widefield microscopy with an extended-source wavefront sensor,* Optica **2**, 682 (2015).

[53] R. J. Zawadzki, S. M. Jones, S. S. Olivier, M. Zhao, B. A. Bower, J. A. Izatt, S. Choi, S. Laut, and J. S. Werner, *Adaptive-optics optical coherence tomography for high-resolution and high-speed 3D retinal in vivo imaging,* Optics Express **13**, 8532 (2005).

[54] J. Thaung, P. Knutsson, Z. Popovic, and M. Owner-Petersen, *Dual-conjugate adaptive optics for wide-field high-resolution retinal imaging,* Optics Express **17**, 4454 (2009).

[55] A. Arias and P. Artal, *Wavefront-shaping-based correction of optically simulated cataracts,* Optica **7**, 22 (2020).

[56] M. Ogasawara and M. Sato, *The applications of a liquid crystal aberration compensator for the optical disc systems,* in *Adaptive Optics for Industry and Medicine*, edited by C. Dainty (Imperial College Press, London, 2008) pp. 369–375.

[57] F. M. Dickey and T. E. Lizotte, *Laser Beam Shaping Applications*, 2nd ed., Optical Science and Engineering (CRC Press, 2017).

[58] C. Rosales-Guzmán and A. Forbes, *How to Shape Light with Spatial Light Modulators* (SPIE, 2017).

[59] S. Verpoort, M. Bittner, and U. Wittrock, *Fast focus-shifter based on a unimorph deformable mirror,* Applied Optics **59**, 6959 (2020).

[60] S. Dimitrov, R. Barrios, B. Matuz, G. Liva, R. Mata-Calvo, and D. Giggenbach, *Digital modulation and coding for satellite optical feeder links with pre-distortion adaptive optics,* International Journal of Satellite Communications and Networking **34**, 625 (2016).

[61] C. E. Carrizo, R. M. Calvo, and A. Belmonte, *Intensity-based adaptive optics with sequential optimization for laser communications,* Optics Express **26**, 16044 (2018).

[62] A. Brady, C. Rössler, N. Leonhard, M. Gier, P. Böttner, R. Eberhardt, A. Tünnermann, and C. Reinlein, *Validation of pre-compensation under point-ahead-angle in a 1 km free-space propagation experiment,* Optics Express **27**, 17840 (2019).

[63] M. D. Oliker and M. T. Gruneisen, *How much value does adaptive optics add to a satellite QKD uplink?* in *Quantum Technologies and Quantum Information Science V*, Vol. 11167, edited by M. T. Gruneisen, M. Dusek, P. M. Alsing, and J. G. Rarity, International Society for Optics and Photonics (SPIE, 2019) pp. 10 – 19.

[64] R. H. Freeman, R. J. Freiberg, and H. R. Garcia, *Adaptive laser resonator,* Optics Letters **2**, 61 (1978).

[65] K. E. Oughstun, *Intracavity adaptive optic compensation of phase aberrations. I: Analysis,* Journal of the Optical Society of America **71**, 862 (1981).

[66] P. Welp, H.-M. Heuck, and U. Wittrock, *Intracavity adaptive optics optimization of an end-pumped Nd:YVO_4 laser,* in *Adaptive Optics for Industry and Medicine*, edited by C. Dainty (Imperial College Press, London, 2008) pp. 413–418.

[67] S. Piehler, T. Dietrich, P. Wittmüss, O. Sawodny, M. A. Ahmed, and T. Graf, *Deformable mirrors for intra-cavity use in high-power thin-disk lasers,* Optics Express **25**, 4254 (2017).

[68] L. Sun, L. Huang, M. Yan, J. Fan, Y. Zheng, and C. Sun, *Intracavity deformable mirror for beam quality improvement and power enhancement of a passively Q-switched laser,* Optics Express **26**, 8594 (2018).

[69] X. Wang, B. Lai, S. Meng, L. Dong, Y. Guo, P. Yang, W. Zhao, S. Chen, C. Su, X. Yu, K. Yang, G. Tang, X. He, S. Wang, and B. Xu, *Adaptive optics compensation inside an Nd:YAG unstable ring laser: Tilt correction performance,* Optics Communications **449**, 94 (2019).

[70] S. Nagel, B. Metzger, T. Gottwald, V. Kuhn, A. Killi, and S. Schad, *Thin disk laser operating in fundamental mode up to a power of 4kW,* in *2019 Conference on Lasers and Electro-Optics Europe & European Quantum Electronics Conference (CLEO/Europe-EQEC)* (2019) pp. 1–1.

[71] J. C. Wyant and K. Creath, *Basic wavefront aberration theory for optical metrology,* in *Applied Optics and Optical Engineering*, Vol. 11, edited by R. R. Shannon and J. C. Wyant (Academic Press, Inc., New York, 1992) Chap. 1.

[72] F. Zernike, *Beugungstheorie des Schneidenverfahrens und seiner verbesserten Form, der Phasenkontrastmethode,* Physica **1**, 689 (1934).

[73] V. N. Mahajan, *Aberration Theory Made Simple,* 2nd ed. (SPIE Press, Bellingham, Washington USA, 2011).

[74] D. H. Wolpert and W. G. Macready, *No free lunch theorems for optimization,* IEEE Transactions on Evolutionary Computation **1**, 67 (1997).

[75] P. Welp, *Festkörperlaser mit resonatorinterner Kompensation von Aberrationen durch adaptive Spiegel,* Ph.D. thesis, University of Münster (2008).

[76] S. Verpoort, *Entwicklung neuartiger deformierbarer Spiegel für den Einsatz in Hochleistungslaser,* Ph.D. thesis, University of Duisburg-Essen (2011).

[77] P. Rausch, *Deformierbare Spiegel für Weltraumteleskope und Hochleistungslaser,* Ph.D. thesis, University of Münster (2016).

[78] S. Verpoort, P. Welp, and U. Wittrock, *Novel unimorph deformable mirror for solid state laser resonators,* in *MEMS Adaptive Optics III*, Vol. 7209, edited by S. S. Olivier, T. G. Bifano, and J. A. Kubby, International Society for Optics and Photonics (SPIE, 2009) pp. 171 – 182.

[79] S. Verpoort and U. Wittrock, *Actuator patterns for unimorph and bimorph deformable mirrors,* Applied Optics **49**, G37 (2010).

[80] S. Verpoort, P. Rausch, and U. Wittrock, *Characterization of a miniaturized unimorph deformable mirror for high power CW-solid state lasers,* in *MEMS Adaptive Optics VI*, Vol. 8253, edited by S. S. Olivier, T. G. Bifano, and J. Kubby, International Society for Optics and Photonics (SPIE, 2012) pp. 67 – 78.

[81] P. Rausch, S. Verpoort, and U. Wittrock, *Unimorph deformable mirror for space telescopes: design and manufacturing,* Optics Express **23**, 19469 (2015).

[82] P. Rausch, S. Verpoort, and U. Wittrock, *Unimorph deformable mirror for space telescopes: environmental testing,* Optics Express **24**, 1528 (2016).

[83] M. Gerhards, S. Verpoort, U. Wittrock, M. Freudling, A. Grzesik, and M. Erhard, *Re-designing a deformable mirror for space-qualification at high vibration load,* (2019) November, 2019, Workshop on Innovative Technologies for Space Optics.

[84] D. Damjanovic, *Ferroelectric, dielectric and piezoelectric properties of ferroelectric thin films and ceramics,* Reports on Progress in Physics **61**, 1267 (1998).

[85] PI Ceramic, *Piezoelectric Materials,* [Online] https://www.piceramic.com/en/products/piezoelectric-materials/ (n.d.), Last accessed August 21, 2020.

[86] R. V. Iyer and X. Tan, *Control of hysteretic systems through inverse compensation,* IEEE Control Systems Magazine **29**, 83 (2009).

[87] P. Krejci and K. Kuhnen, *Inverse control of systems with hysteresis and creep,* IEE Proceedings - Control Theory and Applications **148**, 185 (2001).

[88] K. Kuhnen, *Inverse Steuerung piezoelektrischer Aktoren mit Hysterese-, Kriech- und Superpositionsoperatoren* (Shaker, 2001).

[89] A. Bos, S. Kuiper, B. Dekker, W. Jonker, M. Maniscalco, M. Chun, and H. Priem, *Large Adaptive Secondary Mirrors for Ground-based Astronomy,* in *OSA Imaging and Applied Optics Congress* (2020).

[90] S. Bonora and R. J. Zawadzki, *Wavefront sensorless modal deformable mirror correction in adaptive optics: optical coherence tomography,* Optics Letters **38**, 4801 (2013).

[91] Y. N. Sulai and A. Dubra, *Non-common path aberration correction in an adaptive optics scanning ophthalmoscope,* Biomedical Optics Express **5**, 3059 (2014).

[92] D. J. Wahl, Y. Jian, S. Bonora, R. J. Zawadzki, and M. V. Sarunic, *Wavefront sensorless adaptive optics fluorescence biomicroscope for in vivo retinal imaging in mice,* Biomedical Optics Express **7**, 1 (2016).

[93] B.-J. Seo, E. Cady, B. Gordon, B. Kern, R. Lam, D. Marx, D. Moody, R. Muller, K. Patterson, I. Poberezhskiy, C. M. Prada, E. Sidick, F. Shi, J. Trauger, and D. Wilson, *Hybrid Lyot coronagraph for WFIRST: high-contrast broadband testbed demonstration,* in *Techniques and Instrumentation for Detection of Exoplanets VIII*, Vol. 10400, edited by S. Shaklan, International Society for Optics and Photonics (SPIE, 2017) pp. 106 – 126.

[94] D. Marx, B.-J. Seo, B. Kern, E. Sidick, B. Nemati, and I. Poberezhskiy, *Electric field conjugation in the presence of model uncertainty,* in *Techniques and Instrumentation for Detection of Exoplanets VIII*, Vol. 10400, edited by S. Shaklan, International Society for Optics and Photonics (SPIE, 2017) pp. 188 – 196.

[95] M. J. Booth, *Wave front sensor-less adaptive optics: a model-based approach using sphere packings,* Optics Express **14**, 1339 (2006).

[96] H. Yang, O. Soloviev, and M. Verhaegen, *Model-based wavefront sensorless adaptive optics system for large aberrations and extended objects,* Optics Express **23**, 24587 (2015).

[97] A. Mora and A. Vosteen, *Gaia in-orbit realignment: overview and data analysis,* in *Space Telescopes and Instrumentation 2012: Optical, Infrared, and Millimeter Wave*, Vol. 8442, edited by M. C. Clampin, G. G. Fazio, H. A. MacEwen, and J. M. Oschmann Jr., International Society for Optics and Photonics (SPIE, 2012) pp. 609 – 622.

[98] L. L. A. Vosteen, F. Draaisma, W. P. van Werkhoven, L. J. M. van Riel, M. H. Mol, and G. den Ouden, *Wavefront sensor for the ESA-GAIA mission,* in *Astronomical and Space Optical Systems*, Vol. 7439, edited by P. G. Warren, C. J. Marshall, J. B.

Heaney, E. T. Kvamme, R. K. Tyson, and M. Hart, International Society for Optics and Photonics (SPIE, 2009) pp. 316 – 325.

[99] A. Mora, M. Biermann, A. Bombrun, J. Boyadjian, F. Chassat, P. Corberand, M. Davidson, D. Doyle, D. Escolar, W. L. M. Gielesen, T. Guilpain, J. Hernandez, V. Kirschner, S. A. Klioner, C. Koeck, B. Laine, L. Lindegren, E. Serpell, P. Tatry, and P. Thoral, *Gaia: focus, straylight and basic angle,* in *Space Telescopes and Instrumentation 2016: Optical, Infrared, and Millimeter Wave*, Vol. 9904, edited by H. A. MacEwen, G. G. Fazio, M. Lystrup, N. Batalha, N. Siegler, and E. C. Tong, International Society for Optics and Photonics (SPIE, 2016) pp. 781 – 797.

[100] R. B. Makidon, S. Casertano, C. Cox, and R. van der Marel, *The JWST Point Spread Function: Calculation Methods and Expected Properties,* [Online] https://www.stsci.edu/files/live/sites/www/files/home/jwst/documentation/technical-documents/_documents/JWST-STScI-001157.pdf (2007), Technical Report, Doc #: JWST-STScI-001157, SM-12, Last accessed August 21, 2020.

[101] Alpao Wavefront Sensors, *SH-CMOS-fast,* [Online] https://www.alpao.com/adaptive-optics/wavefront-sensors.html (n.d.), Last accessed August 21, 2020.

[102] L. H. Schatz, J. R. Males, L. M. Close, O. Durney, O. Guyon, M. Hart, J. Lumbres, K. Miller, J. Knight, A. T. Rodack, J. D. Long, K. V. Gorkom, M. Jean, and M. Kautz, *Design of the MagAO-X pyramid wavefront sensor,* in *Adaptive Optics Systems VI*, Vol. 10703, edited by L. M. Close, L. Schreiber, and D. Schmidt, International Society for Optics and Photonics (SPIE, 2018) pp. 671 – 679.

[103] M. Blum, M. Büeler, C. Grätzel, and M. Aschwanden, *Compact optical design solutions using focus tunable lenses,* in *Optical Design and Engineering IV*, Vol. 8167, edited by J.-L. M. Tissot, J. M. Raynor, L. Mazuray, R. Wartmann, and A. Wood, International Society for Optics and Photonics (SPIE, 2011) pp. 274 – 282.

[104] M. Bathe-Peters, P. Annibale, and M. J. Lohse, *All-optical microscope autofocus based on an electrically tunable lens and a totally internally reflected IR laser,* Optics Express **26**, 2359 (2018).

[105] Sony digital cameras, *α6400,* [Online] https://www.sony.co.uk/electronics/interchangeable-lens-cameras/ilce-6400 (n.d.), Last accessed August 21, 2020.

[106] O. Kazasidis, S. Verpoort, O. Soloviev, G. Vdovin, M. Verhaegen, and U. Wittrock, *Extended-image-based correction of aberrations using a deformable mirror with hysteresis,* Optics Express **26**, 27161 (2018).

[107] O. Kazasidis, S. Verpoort, and U. Wittrock, *Aberration balancing using an image-sharpness metric,* Journal of the Optical Society of America A **36**, 1418 (2019).

[108] O. Kazasidis, S. Verpoort, and U. Wittrock, *Sensor for dynamic focus control of a deformable mirror,* Applied Optics **59**, 5625 (2020).

2

A TESTBED FOR IMAGE-BASED CORRECTION OF STATIC ABERRATIONS FOR EXTENDED OBJECTS

With a view to the next generation of large space telescopes, we investigate guide-star-free, image-based aberration correction using a unimorph deformable mirror in a plane conjugate to the primary mirror. For this purpose, we design and build a high-resolution imaging testbed to evaluate control algorithms. In this chapter, we describe the testbed design and the control of the deformable mirror in three different control domains, and we introduce the used merit function.

Parts of this chapter have been published in Optics Express **26**, 27161–27178 (2018) [1].

2.1. INTRODUCTION

The Hubble Space Telescope (HST) with a 2.4-m primary mirror had the highest angular resolution in the visible range of all astronomical telescopes for almost 20 years until the early 2010s. The forthcoming James Webb Space Telescope (JWST) has a 6.5-m lightweight, segmented primary mirror, that cannot yield diffraction-limited imaging in the visible. Both HST and JWST have active primary mirrors. The actuators on HST's primary mirror have never been used because its thick mirror turned out to be sufficiently stable, and diffraction-limited resolution was achieved after the COSTAR system was installed [2]. Each of the thin segments of JWST's primary mirror has six actuators for rigid body motions and one actuator for controlling its curvature. JWST will be diffraction-limited in the infrared, but will have an insufficient surface figure for diffraction-limited imaging in the visible.

Space telescopes with angular resolution higher than HST are currently discussed for characterization of exoplanets and for Earth observation from a geostationary orbit. Such telescopes will need to have segmented, lightweight primaries in order to reduce mass and stowed volume. Active optics at the primary mirror and/or in a plane conjugate to the primary mirror will be required. The proposed coronagraph for the RST[1] with a 2.4-m primary mirror, which is planned for mid-2020s launch, will use two high-order deformable mirrors to control both the phase and the amplitude of the wavefront, and to keep the phase stable at picometer level [3], which is not required in this work. One of these deformable mirrors will be conjugated to the system pupil and will additionally correct low-order Zernike modes at 5 mHz [4]. The proposed HDST[2], planned for the 2030s, is envisioned to have a 12-m active segmented primary mirror. The proposed designs for its coronagraph instrument use one or two deformable mirrors [5].

Active and adaptive deformable mirrors often employ actuators which suffer from hysteresis, e.g., piezoelectric actuators. Ground-based astronomical telescopes use natural or artificial guide stars to sense the atmospheric turbulence. Their deformable mirrors are controlled in closed-loop, thereby eliminating the influence of hysteresis. However, it is not possible for every science target to have a sufficiently bright guide star inside the field of view. In addition, direct wavefront sensing using a dedicated wavefront sensor has limited dynamic range and results in non-common path errors.

There exist two main categories of wavefront-sensorless operation, depending on whether the wavefront information is required or not. In the first category, the wavefront information is retrieved by using an indirect iterative method. An example is phase diversity [6–8] that requires two or more measurements of the focal plane intensity taken with different known phase functions physically introduced into the optical system. An estimate for the wavefront is calculated from these measurements and therefore several iterations are required. Finally, the inverse wavefront is applied to the wavefront corrector. In the second category there are completely wavefront-free approaches that do not require the wavefront information, but use the very image captured with the optical sys-

[1] The Nancy Grace Roman Space Telescope, formerly known as the Wide Field Infrared Survey Telescope (WFIRST).

[2] The concept of the High-Definition Space Telescope (HDST) has been transformed to the Large Ultraviolet Optical Infrared Surveyor (LUVOIR), one of the proposals studied for the National Academy of Sciences 2020 Astronomy and Astrophysics Decadal Survey.

tem to directly generate the feedback signal for the wavefront corrector. Although here it is not required for the correction, the original aberrated wavefront can be estimated, provided that the wavefront corrector is linear, when the correction is optimal, i.e., the final corrected wavefront is almost plane. The so-called model-based methods model the influence of aberrations in the imaging system. Booth modeled the imaging of a point source in the presence of aberrations with RMS amplitudes smaller than 1 rad and expressed as series of Zernike modes [9]. He later extended the approach for arbitrarily large aberrations expressed as a series of Lukosz-Zernike functions [10]. Linhai and Rao proposed a general model-based approach insensitive to the selection of the sets of functions [11]. Yang *et al.* further extended the model to imaging of extended objects [12]. Model-based approaches converge fast at the expense of potential errors due to inaccuracy of the model. On the contrary, model-free approaches need no prior knowledge of the system and iteratively optimize a merit function calculated from the image. These approaches commonly require more iterations, but are simpler, free of modeling errors and uncertainties, and have more general applicability. Model-free wavefront-sensorless adaptive optics has been presented for microscopy [13], optical coherence tomography [14], and ophthalmoscopy [15, 16], among others. The configuration parameters for the control of a model-free wavefront-sensorless adaptive optics system are the merit function, the control domain for the wavefront corrector, and the search algorithm. Their selection and combination depend on the system requirements and are critical for the overall performance.

We designed and built a high-resolution imaging system as testbed for control algorithms for image-based optimization. A space-qualified unimorph deformable mirror based on piezoelectric actuation [17] is at the core of our system. However small the modeling errors of the nonlinearities of the deformable mirror (hysteresis, creep) may be, they become significant for a high-resolution imaging system. Therefore, we implement a model-free iterative control method. Aberrations are induced by a nominally identical deformable mirror and are corrected in a conjugate plane. Our system resembles that of Murray *et al.* [18]. They induced Zernike aberrations by a spatial light modulator and corrected them with a membrane deformable mirror using an image sharpness metric and voltage-based global search algorithms. Dong and Yu used a hybrid approach to correct aberrations induced by a trial lens [19]. The correction was carried out in a non-conjugate plane using a membrane deformable mirror. Finally, Agbana *et al.* experimentally validated the model-based approach of Yang *et al.* [12], imaging a point source [20]. They induced aberrations with a phase plate and corrected them with a membrane deformable mirror.

We investigate guide-star-free, image-based correction of the aberrations of a primary mirror using a unimorph deformable mirror. The deformable mirror is placed in a plane conjugate to the primary mirror and it suffers from hysteresis. Section 2.2 presents the testbed and discusses its key characteristics. In Section 2.3, we describe the deformable mirror control in three different domains, namely the voltage domain, the domain of the Zernike modes, and the domain of its singular modes. Finally, in Section 2.4, we introduce the used merit function.

2.2. TESTBED

Our testbed is illustrated in Fig. 2.1. Static aberrations are deliberately induced by a unimorph deformable mirror (called the *aberration generator*). The aberration correction takes place in a plane conjugate to the aberration generator by a second, nominally identical unimorph deformable mirror (called the *aberration corrector*). The deformable mirrors feature a 50 mm aperture and were developed and manufactured at the FH Münster University of Applied Sciences. The design, manufacturing and testing of the deformable mirrors are described in [17, 21]. When the aberration generator positioned in plane B is deformed, an aberrated image is formed in plane A′. The aberration corrector is positioned in plane B′, which is conjugated to plane B, and corrects the aberrations. The corrected image is formed in plane A″ and is detected by the CCD.

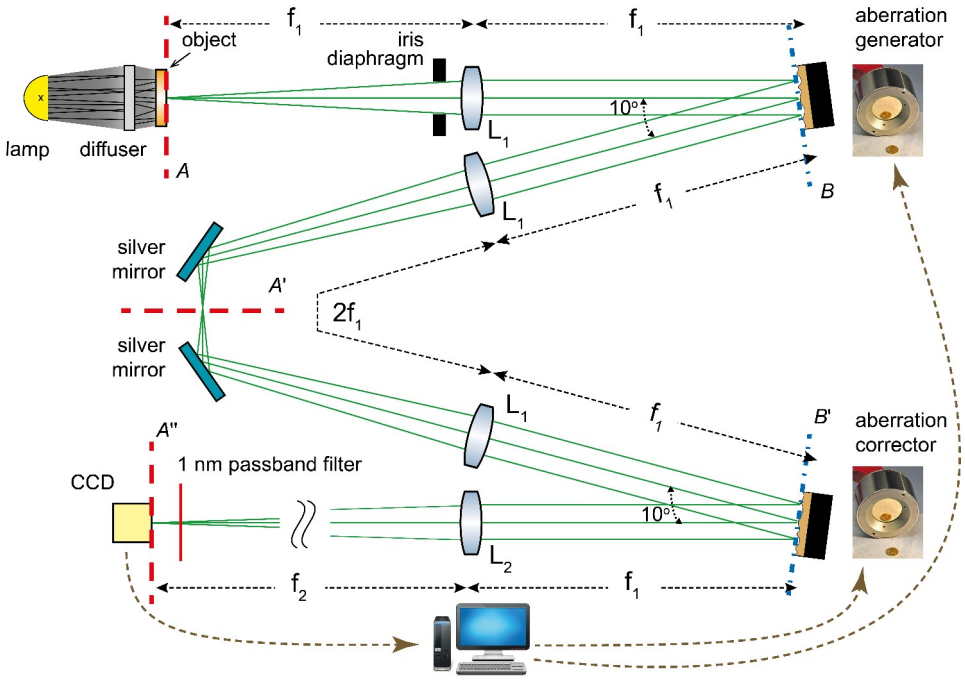

Figure 2.1: Sketch of the testbed. The plane of aberration generation (B) is imaged to the plane of aberration correction (B′) with a 4-f telescope and a magnification of −1. The letters A, A′ and A″ indicate the image-forming conjugate planes. The magnification from plane A to plane A′ is −1, and from plane A′ to plane A″ is −3. The angles of incidence on the deformable mirrors are approximately 5°. Due to the non-perpendicular incidence on the deformable mirrors, we place the two silver mirrors around plane A′ to ensure the correct conjugation between the planes B and B′. Lenses focal lengths: $f_1 = 250$ mm, $f_2 = 750$ mm. An image captured with our testbed is shown in Fig. 2.2.

The object is placed one focal length in front of a converging lens to simulate a distant science target. It is illuminated from the back by a halogen lamp. Homogeneous illumination with a wide spatial frequency content is produced by a ground glass diffuser. Four achromatic doublets from Newport, designed for infinite conjugate ratio,

with 76.2 mm diameter are used for relay-imaging. The first three doublets are identical PAC095 with 250 mm effective focal length. The last doublet is a PAC097 with 750 mm effective focal length, leading to a 3x magnification of the object on the CCD. Although the achromats reduce chromatic aberration, they do not eliminate it completely. Therefore, a narrow-band spectral filter with a center wavelength of 632.8 nm and a full width at half maximum of 1.0 nm is placed directly in front of the CCD. The aberration generator is conjugated to the aberration corrector with a unit magnification, which means that at least in principle the aberrations can be fully compensated for an arbitrary wide field of view.

The two deformable mirrors exhibit approximately 40 nm and 17 nm RMS aberration that cannot be compensated for. It consists of print-through and other high-order aberrations. The aperture of the testbed can be adjusted by the iris diaphragm in front of the first achromat. We have stopped down to f/5.4, the maximum diffraction-limited aperture for the achromats. The theoretical cutoff frequency is 290 lp/mm for the wavelength of 633 nm.

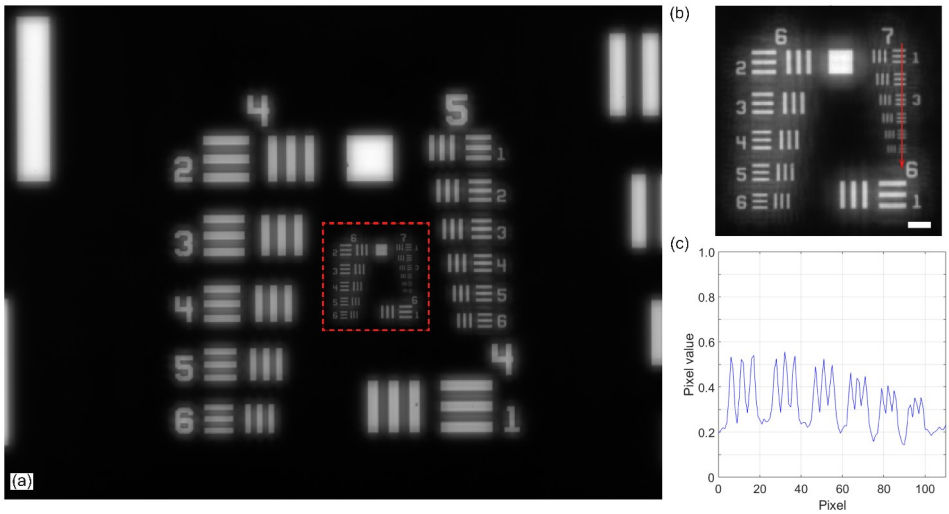

Figure 2.2: (a) The detected image with the negative 1951 USAF test target. (b) Highlighted zoom of the image showing the designated region of interest of (a), with the elements of groups 6 and 7. The white horizontal scale bar in the lower right corner of the image is 31 µm long. (c) The pixel values of the six elements under the red arrow drawn in (b). The three bars of the sixth element shown at the end of the graph have 228 lp/mm density and are resolved with about 10% contrast.

We detect the image with a CCD with 4.65 µm pixel size and 5.9 mm × 4.5 mm sensor size, and calibrate it using a master dark frame and a master flat frame. A calibrated image is shown in Fig. 2.2(a). The limiting resolution of the CCD is 108 lp/mm, which corresponds to 324 lp/mm on the object side. Thus it can detect the theoretical cutoff frequency of the testbed. However, sampling artifacts are expected at spatial frequencies higher than 162 lp/mm in the object [22]. For each experiment we select a region of interest on the CCD, for which we calculate the merit function. ZEMAX calculations for the aberration-free scenario showed that diffraction-limited performance is expected for

the central 2 mm × 2 mm of the object, leading to an area of 6 mm × 6 mm in the image plane, which exceeds the CCD sensor size.

2.3. DEFORMABLE MIRROR CONTROL

The surface of the deformable mirrors is controlled by 44 actuators arranged in a keystone pattern. The actuator pattern has been optimized to reproduce low-order Zernike modes up to Z_{12} (secondary astigmatism 45°) with large stroke [23]. Throughout this thesis, we use the Zernike notation of Wyant and Creath [24], as presented in Section 1.2. The 44 influence functions were captured using a phase-shifting interferometer with 2 nm RMS repeatability and the mirror surface was fitted using 99 Zernike modes [25, 26]. With the same interferometer, we also measured the initial surface deformation of the mirrors and characterized their hysteresis. The influence functions, expressed in 99 Zernike coefficients, are grouped into the columns of the influence matrix ($\boldsymbol{IM}_{99\times44}$). Using the singular-value decomposition (SVD) [27] and applying the Moore–Penrose pseudoinversion we obtain the control matrix ($\boldsymbol{CM}_{44\times99}$):

$$\boldsymbol{IM} = \boldsymbol{U}\,\boldsymbol{S}\,\boldsymbol{W}^T \quad \Rightarrow \quad \boldsymbol{CM} = \boldsymbol{IM}^+ = \boldsymbol{W}\,\boldsymbol{S}^{-1}\,\boldsymbol{U}^T\,, \tag{2.1}$$

where $\boldsymbol{U}$, $\boldsymbol{S}$, and $\boldsymbol{W}$ are the matrices of the SVD. The influence matrix returns the mirror surface in 99 Zernike modes ($\vec{z}_{\text{real}}$) when multiplied by a vector containing the voltages that are applied to the actuators of the mirror. In turn, the control matrix gives the required voltages for a desired mirror surface expressed in Zernike modes ($\vec{z}_{\text{des}}$):

$$\vec{z}_{\text{real}} = \boldsymbol{IM}\,\vec{u} \quad \Rightarrow \quad \vec{u} = \boldsymbol{CM}\,\vec{z}_{\text{des}}\,, \tag{2.2}$$

where $\vec{u}$ is the column vector of the actuators' voltages, and $\vec{z}$ is the column vector of the coefficients of the first 99 Zernike modes that describe the mirror surface. The matrix $\boldsymbol{S}$ of the SVD is diagonal and contains the singular values of the $\boldsymbol{IM}$ in decreasing order. We restrict the condition number (the ratio of the largest singular value to the smallest singular value) of the $\boldsymbol{IM}$ to 200, by truncating the smallest singular values. Thus we keep the pseudoinverse $\boldsymbol{CM}$ well-conditioned. The similarity matrix $\boldsymbol{IM}\cdot\boldsymbol{CM}$ reveals the generation efficiency of the Zernike modes and possible modal cross-talk [28]. The left side of Fig. 2.3 shows the absolute value of the similarity matrix for the first 41 Zernike modes. The generation efficiency is larger than 0.97 for all Zernike modes up to Z_{12} (secondary astigmatism 45°). For higher-order modes, the generation efficiency is lower and modal cross-talk arises. Z_{15} (secondary spherical aberration) is the first Zernike mode for which the generation efficiency drops below 0.5 (see right plot in Fig. 2.3). The left side of Fig. 2.3 shows an example of modal cross-talk: if we want to generate 1 µm of Z_{13} (secondary coma x), we will get a surface with 0.87 µm of Z_{13} and additional higher-order modes, the most prominent of which is Z_{22} (tertiary coma x) with an amplitude of −0.31 µm.

For the correction process we use all the Zernike modes up to the fifth radial order plus some additional higher-order modes up to Z_{32} (quaternary astigmatism 45°). This number is considered to be a good compromise between the generation of sufficiently high spatial frequency deformation that can compensate for hysteresis, and keeping the number of control variables low.

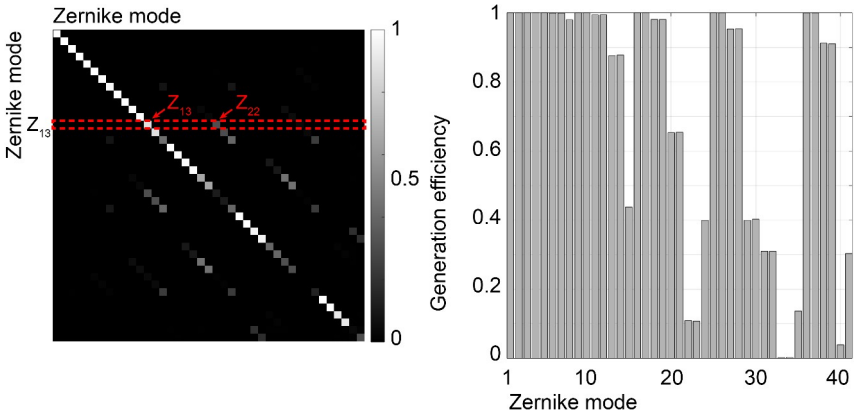

Figure 2.3: Left: The absolute value of the similarity matrix for the first 41 Zernike modes for the deformable mirror used as aberration corrector. The matrix is diagonally dominant. The nonzero off-diagonal elements reveal modal cross-talk. An example is marked with red dashed lines: if we want to generate 1 µm of Z_{13}, we will get a surface with 0.87 µm of Z_{13} and −0.31 µm of Z_{22}. Right: The generation efficiency for the first 41 Zernike modes. These are the diagonal elements of the similarity matrix shown on the left.

The columns of the matrix $\boldsymbol{W}$ of the SVD make up an orthonormal set and are the *singular modes* of the deformable mirror [29]. The singular modes resemble the mechanical eigenmodes of the mirror. The singular values of the matrix $\boldsymbol{S}$ designate the gain of the corresponding singular mode. The singular modes are related to the actuators' voltages:

$$\vec{s}_{\text{real}} = \boldsymbol{S}\,\boldsymbol{W}^T\,\vec{u} \quad \Rightarrow \quad \vec{u} = \boldsymbol{W}\,\boldsymbol{S}^{-1}\,\vec{s}_{\text{des}}\,, \tag{2.3}$$

where $\vec{s}_{\text{real}}$ and $\vec{s}_{\text{des}}$ are column vectors containing the coefficients of the singular modes. Equation (2.3) can be used to find the required voltages for a superposition of the singular modes of the deformable mirror that results in a desired deformation of the mirror. Applying the same restriction for the condition number as above (less than 200), we truncate the 4 singular modes with the smallest gain, leaving 40 singular modes to work with. In contrast to the Zernike modes, the similarity matrix of the singular modes is by definition the identity matrix, leading to a generation efficiency of 1 and no modal cross-talk. In our Zernike representation, the Zernike modes are normalized to the peak-to-valley surface amplitude. For consistency, we also normalized the singular modes to the peak-to-valley surface amplitude. The first 11 singular modes of the aberration corrector are shown in the left plot of Fig. 2.4. In the right plot of Fig. 2.4 the normalized singular values of the aberration corrector are drawn, together with the limiting condition number.

We control the deformable mirrors in three different domains: 1) by directly selecting the actuators' voltages, 2) by selecting a 99-Zernike-modes vector and calculating the voltages via Eq. (2.2), and 3) by selecting a 40-singular-modes vector and calculating the voltages via Eq. (2.3). The piezoelectric hysteresis is compensated open-loop using the Prandtl-Ishlinskii formalism [26], as described in [30, 31]. This reduces the hysteresis from 15% to 2%. However, the residual, uncompensated hysteresis of 2% limits the system performance. The voltages are limited to the range from −380 to +400 V in order to

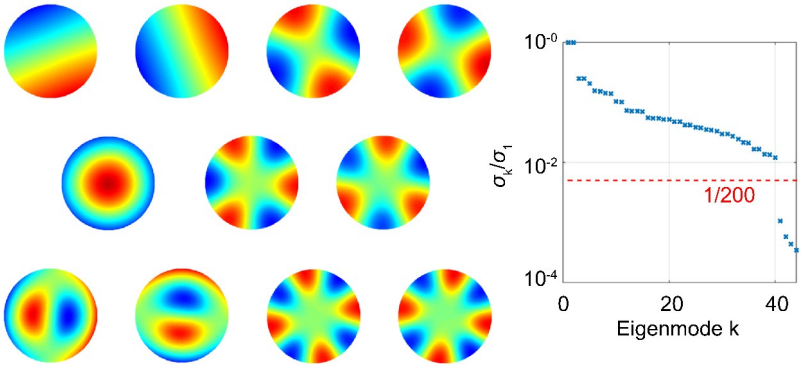

Figure 2.4: Left: The first 11 singular modes of the aberration corrector, ordered with decreasing singular value (i.e., gain) from left to right and from top to bottom. They are very similar to low-order Zernike modes (compare with Fig. 1.1). The singular modes are numerically calculated from the experimentally measured influence matrix. Right: The normalized singular values of the aberration corrector. The dashed red line designates the maximum allowed condition number (200), which leads to truncating the 4 smallest singular values.

protect the actuators. Any voltage vector with values outside this range is rejected using a saturation control.

Figure 2.5 illustrates the control block diagram of our testbed. An aberration is applied to the aberration generator. The image generated by the testbed and detected by the CCD shown in Fig. 2.2(a) is evaluated with the merit function. Our algorithm then selects the next vector to be investigated. Depending on the domain, this can be a voltage vector $\vec{u}$, a Zernike vector $\vec{z}$, or a vector of singular modes $\vec{s}$. The output vector is converted to voltages, which are applied to the aberration corrector after passing the open-loop hysteresis compensation and the saturation control.

2.4. MERIT FUNCTION

The merit function is calculated only for a certain region of interest, which is a user-defined region of the full image captured with the CCD. Our merit function (MF) is an integral measure of the contrast of the image. We have defined it in the following way:

$$\mathrm{MF} = -\frac{\sum_{n_x=1}^{N_x}\sum_{n_y=1}^{N_y} I(n_x,n_y)^2}{\left[\sum_{n_x=1}^{N_x}\sum_{n_y=1}^{N_y} I(n_x,n_y)\right]^2} N_x N_y\,. \tag{2.4}$$

where x and y are the axes of the image coordinate system within the region of interest, N_x and N_y are the numbers of the pixels in each axis, and I is the pixel output. Our MF is a normalized discrete version of the common sharpness metric S_1 presented by Muller and Buffington [32]. The normalization has been proposed to account for intensity variations [15]. We have noticed that the non-normalized version can be easier trapped in local minima in case of strong aberrations. The multiplication by the total number of CCD pixels allows the comparison among images of different number of pixels. The minus sign of the MF converts the sharpness maximization to a minimization problem.

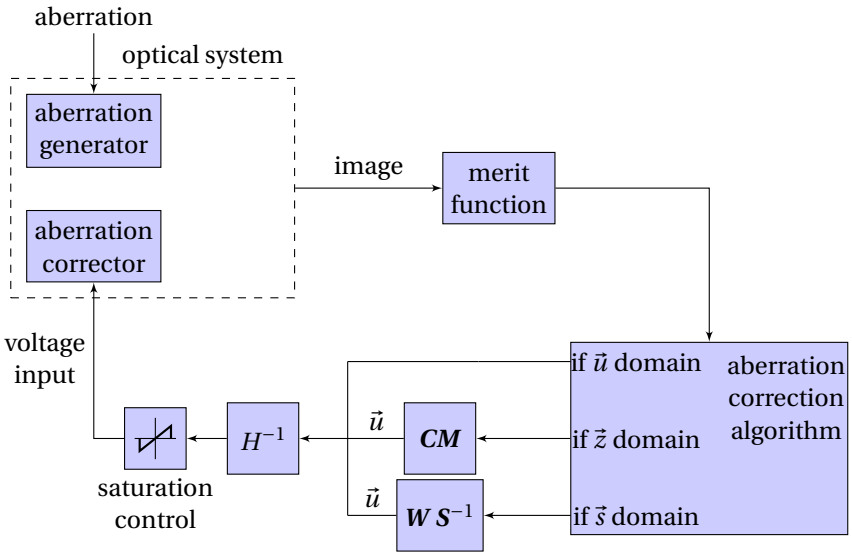

Figure 2.5: The control block diagram for the aberration correction. The aberration correction algorithm can be forced to operate in the domain of voltages ($\vec{u}$), Zernike modes ($\vec{z}$), or singular modes ($\vec{s}$). When operating in the Zernike mode domain or in the singular mode domain, the outputs are converted to voltages by matrix multiplication. The control input for the aberration corrector is generated after passing through the open-loop hysteresis compensation (H^{-1}) and the saturation control.

This merit function is in principle insensitive to image shift. We experimentally determined the random error of our merit function by 300 repetitions of reapplying a specific voltage vector and obtaining the value of the MF when imaging the groups 6 and 7 of the negative 1951 USAF test target. The random error, given by three standard deviations of these 300 values, was $\pm 4.6 \cdot 10^{-3}$ or $\pm 0.3\%$, indicating sufficient repeatability.

The merit function is discussed in more detail in Chapter 3.

REFERENCES

[1] O. Kazasidis, S. Verpoort, O. Soloviev, G. Vdovin, M. Verhaegen, and U. Wittrock, *Extended-image-based correction of aberrations using a deformable mirror with hysteresis,* Optics Express **26**, 27161 (2018).

[2] M. D. Lallo, *Experience with the Hubble Space Telescope: 20 years of an archetype,* Optical Engineering **51**, 011011 (2012).

[3] J. T. Trauger, D. C. Moody, J. E. Krist, and B. L. Gordon, *Hybrid Lyot coronagraph for WFIRST-AFTA: coronagraph design and performance metrics,* Journal of Astronomical Telescopes, Instruments, and Systems **2**, 011013 (2016).

[4] F. Shi, K. Balasubramanian, R. Hein, R. Lam, D. Moore, J. Moore, K. Patterson, I. Poberezhskiy, J. Shields, E. Sidick, H. Tang, T. Truong, J. K. Wallace, X. Wang, and D. Wilson, *Low-order wavefront sensing and control for WFIRST-AFTA coronagraph,* Journal of Astronomical Telescopes, Instruments, and Systems **2**, 011021 (2016).

[5] AURA Report, *From Cosmic Birth to Living Earths,* [Online] `http://www.hdstvision.org/report` (2015), Last accessed August 21, 2020.

[6] B. H. Dean and C. W. Bowers, *Diversity selection for phase-diverse phase retrieval,* Journal of the Optical Society of America A **20**, 1490 (2003).

[7] A. Give'on, B. D. Kern, and S. Shaklan, *Pair-wise, deformable mirror, image plane-based diversity electric field estimation for high contrast coronagraphy,* in *Techniques and Instrumentation for Detection of Exoplanets V*, Vol. 8151, edited by S. Shaklan, International Society for Optics and Photonics (SPIE, 2011) pp. 376 – 385.

[8] M. W. Warmuth, S. W. Parker, A. J. Wilson, K. W. Gleichman, R. G. Paxman, B. J. Thelen, R. J. Murphy, J. D. Hunt, and J. W. LeBlanc, *Operation of phase-diverse adaptive-optics with extended scenes,* in *Advanced Wavefront Control: Methods, Devices, and Applications VI*, Vol. 7093, edited by J. D. Gonglewski, R. A. Carreras, and T. A. Rhoadarmer, International Society for Optics and Photonics (SPIE, 2008) pp. 34 – 44.

[9] M. J. Booth, *Wave front sensor-less adaptive optics: a model-based approach using sphere packings,* Optics Express **14**, 1339 (2006).

[10] M. J. Booth, *Wavefront sensorless adaptive optics for large aberrations,* Optics Letters **32**, 5 (2007).

[11] H. Linhai and C. Rao, *Wavefront sensorless adaptive optics: a general model-based approach,* Optics Express **19**, 371 (2011).

[12] H. Yang, O. Soloviev, and M. Verhaegen, *Model-based wavefront sensorless adaptive optics system for large aberrations and extended objects,* Optics Express **23**, 24587 (2015).

[13] J. Mertz, H. Paudel, and T. G. Bifano, *Field of view advantage of conjugate adaptive optics in microscopy applications,* Applied Optics **54**, 3498 (2015).

[14] S. Bonora and R. J. Zawadzki, *Wavefront sensorless modal deformable mirror correction in adaptive optics: optical coherence tomography,* Optics Letters **38**, 4801 (2013).

[15] Y. N. Sulai and A. Dubra, *Non-common path aberration correction in an adaptive optics scanning ophthalmoscope,* Biomedical Optics Express **5**, 3059 (2014).

[16] D. J. Wahl, Y. Jian, S. Bonora, R. J. Zawadzki, and M. V. Sarunic, *Wavefront sensorless adaptive optics fluorescence biomicroscope for in vivo retinal imaging in mice,* Biomedical Optics Express **7**, 1 (2016).

[17] P. Rausch, S. Verpoort, and U. Wittrock, *Unimorph deformable mirror for space telescopes: environmental testing,* Optics Express **24**, 1528 (2016).

[18] L. P. Murray, J. C. Dainty, J. Coignus, and F. Felberer, *Wavefront correction of extended objects through image sharpness maximization,* in *Fifth International Workshop on Adaptive Optics for Industry and Medicine*, Vol. 6018, edited by W. Jiang, International Society for Optics and Photonics (SPIE, 2006) pp. 369 – 378.

[19] B. Dong and J. Yu, *Hybrid approach used for extended image-based wavefront sensor-less adaptive optics,* Chinese Optics Letters **13**, 041101 (2015).

[20] T. E. Agbana, H. Yang, O. Soloviev, G. Vdovin, and M. Verhaegen, *Sensorless adaptive optics system based on image second moment measurements,* in *Optics, Photonics and Digital Technologies for Imaging Applications IV*, Vol. 9896, edited by P. Schelkens, T. Ebrahimi, G. Cristóbal, F. Truchetet, and P. Saarikko, International Society for Optics and Photonics (SPIE, 2016) pp. 22 – 30.

[21] P. Rausch, S. Verpoort, and U. Wittrock, *Unimorph deformable mirror for space telescopes: design and manufacturing,* Optics Express **23**, 19469 (2015).

[22] G. D. Boreman, *Modulation Transfer Function in Optical and Electro-Optical Systems* (SPIE, 2001).

[23] S. Verpoort and U. Wittrock, *Actuator patterns for unimorph and bimorph deformable mirrors,* Applied Optics **49**, G37 (2010).

[24] J. C. Wyant and K. Creath, *Basic wavefront aberration theory for optical metrology,* in *Applied Optics and Optical Engineering*, R. R. Shannon and J. C. Wyant, eds. (Academic, Inc., 1992, Vol. 11).

[25] J. Perchermeier and U. Wittrock, *Precise measurements of the thermo-optical aberrations of an Yb:YAG thin-disk laser,* Optics Letters **38**, 2422 (2013).

[26] P. Rausch, *Deformierbare Spiegel für Weltraumteleskope und Hochleistungslaser*, Ph.D. thesis, University of Münster (2016).

[27] W. H. Press, S. Teukolsky, W. T. Vetterling, and B. P. Flannery, *Numerical Recipes in C: The Art of Scientific Computing* (Cambridge University, 1992).

[28] M. Booth, T. Wilson, H.-B. Sun, T. Ota, and S. Kawata, *Methods for the characterization of deformable membrane mirrors,* Applied Optics **44**, 5131 (2005).

[29] C. Paterson, I. Munro, and J. C. Dainty, *A low cost adaptive optics system using a membrane mirror,* Optics Express **6**, 175 (2000).

[30] P. Krejci and K. Kuhnen, *Inverse control of systems with hysteresis and creep,* IEE Proceedings - Control Theory and Applications **148**, 185 (2001).

[31] K. Kuhnen, *Inverse Steuerung piezoelektrischer Aktoren mit Hysterese-, Kriech- und Superpositionsoperatoren* (Shaker, 2001).

[32] R. A. Muller and A. Buffington, *Real-time correction of atmospherically degraded telescope images through image sharpening,* Journal of the Optical Society of America **64**, 1200 (1974).

3

MERIT FUNCTION LANDSCAPE FOR IMAGE-BASED WAVEFRONT CONTROL USING ZERNIKE MODES

Image-sharpness metrics can be used to optimize optical systems and to control wavefront sensorless adaptive optics systems. We show that for an aberrated system the numerical value of an image-sharpness metric can be improved by adding specific aberrations. The optimum amplitudes of the additional aberrations depend on the power spectral density of the spatial frequencies of the object.

Parts of this chapter have been published in Journal of the Optical Society of America A **36**, 1418–1422 (2019) [1] and in Proceedings of SPIE 10695 (2018) [2].

3.1. INTRODUCTION

It is often desirable to state the performance of an optical system by a single number. This immediately allows ranking different optical systems, optimizing an optical system during its design, or finding the optimum state of an active or adaptive optics system. The wavefront variance σ^2 is such a single number, calculated from the wavefront W in the exit pupil: $\sigma^2 = \overline{W^2} - \overline{W}^2$. The wavefront variance is a useful measure for the optical performance for systems near the diffraction-limit, i.e., for wavefront aberration of less than about $\lambda/8$ RMS. For such systems, other performance metrics can be approximated from the wavefront variance. One example is the Strehl ratio S with the Maréchal approximation $S \approx \left(1 - 2\pi^2\sigma^2/\lambda^2\right)^2$ [3], where λ is the wavelength. Therefore, near the diffraction-limit, maximizing the Strehl ratio is equivalent to minimizing the wavefront variance.

The measurement of the wavefront variance requires a wavefront sensor, and the measurement of the Strehl ratio requires a point object. Both requirements can be circumvented by using performance metrics directly calculated from the intensity distribution in the image plane $I(\mathbf{x})$, where $\mathbf{x}$ is the position vector in the image plane.

Aberration balancing describes the deliberate addition of specific aberrations to an aberrated system in order to optimize a performance metric, commonly to minimize the wavefront variance [4]. In this chapter, we introduce the concept of aberration balancing for maximizing an image-sharpness metric. Section 3.2 describes the method for simulating the point spread function (PSF) and the imaging of an extended object. In Section 3.3, we employ Fourier optics to derive how the image-sharpness metric depends on the properties of the optical system and the object. In Sections 3.4 and 3.5, we use Zernike modes to explore the landscape of the image-sharpness metric for a point object and for an extended object. We show that for a severely aberrated system, the metric can be improved by adding specific Zernike modes, although this increases the wavefront variance. In Section 3.6, we use the testbed presented in Chapter 2 to experimentally test our findings. Section 3.7 summarizes our results and discusses their implications, especially in controlling severely aberrated wavefront-sensorless adaptive and active optics systems.

3.2. SIMULATION METHOD

3.2.1. PSF SIMULATION

We simulate the wavefront in the exit pupil of an isoplanatic imaging system with a homogeneously illuminated circular pupil in MATLAB over a 300×300 pixel grid. The discussion and the results can be appropriately adapted for a different pupil. Phase aberration is expressed as Zernike modes, with 0.05λ step size for their amplitudes. We use the notation of Wyant and Creath [5], as presented in Section 1.2. The PSF is calculated by applying the 2D fast Fourier transform to the exit pupil function. We choose the width of the diffraction-limited PSF to be 40 pixels, significantly larger than the required width of 5 pixels, according to the Nyquist sampling theorem. Thus, the simulations are free from sampling artifacts. We limit the PSF to a 1201×1201 pixel grid, 30 times larger than the diffraction-limited PSF. The error caused by this truncation is negligible. The aberrated PSFs are normalized to the maximum of the diffraction-limited PSF, to allow compar-

ison among PSFs with different aberrations. Each pixel is sampled with 16-bit depth, which matches the analog-to-digital converter used in the Near Infrared Camera of the upcoming James Webb Space Telescope [6].

3.2.2. IMAGE SIMULATION

An extended object can be regarded as the superposition of many point objects. Therefore, its image is the superposition of the images of all point objects. For the image simulation, we calculate the convolution of the zero-padded object with a PSF. The aberrated images are normalized to the maximum of the diffraction-limited image, to allow comparison among images with different aberrations.

The Rayleigh resolution limit equals the diffraction-limited PSF radius, i.e., 20 pixels. In the case of a bar target as object (an example is shown in Fig. 3.1), the Rayleigh resolution limit corresponds to a linewidth of 10 pixels. The cutoff frequency of the simulated diffraction-limited imaging system s_{cut} corresponds to its Sparrow resolution limit that is about 20% smaller than the Rayleigh limit, i.e., at a linewidth of 8 pixels for a bar target. Figure 3.1 shows the resolution limits. Here the objects are binary sets of three horizontal and three vertical lines with the specified linewidth. The contrast for the Rayleigh resolution limit is 11% and for the Sparrow resolution limit it is 0%.

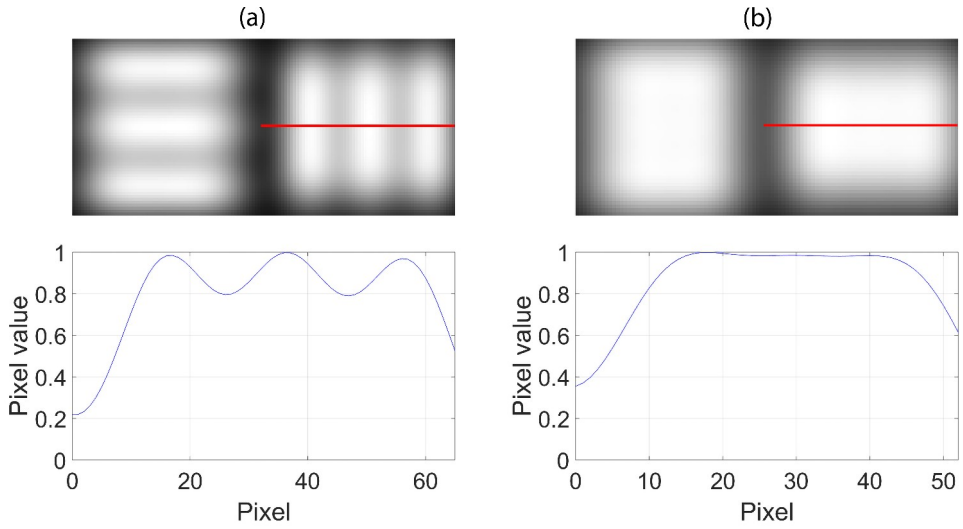

Figure 3.1: (a) The Rayleigh resolution limit with 11% contrast for bars with 10 pixels linewidth. (b) The Sparrow resolution limit with 0% contrast for bars with 8 pixels linewidth.

We create a synthetic extended object that we call the “planet–moon object” and is shown in Fig. 3.2(a). It is a synthesis of two bodies: of an image of the Earth taken by the Earth Polychromatic Imaging Camera on board NASA’s Deep Space Climate Observatory satellite [7] and of an image of the Moon taken by the cameras aboard NASA’s Lunar Reconnaissance Orbiter spacecraft [8]. The images were converted to grayscale to simulate monochromatic imaging. The separation between the centers of the bodies is 80 pixels, which corresponds to 0.1 of the cutoff frequency. Their diameter ratio is about 3.7, equal

to the Earth–moon diameter ratio. The ratio of the mean brightnesses of the bodies is 3.6, equal to the ratio of the geometric albedos of the Earth and of the Moon [9]. The size of the planet–moon object is 300 × 300 pixels. Figure 3.2(b) shows the diffraction-limited image, where some structural characteristics of the planet are apparent. Figure 3.2(c) shows the pixel profiles along the red lines of Figs. 3.2(a) and 3.2(b).

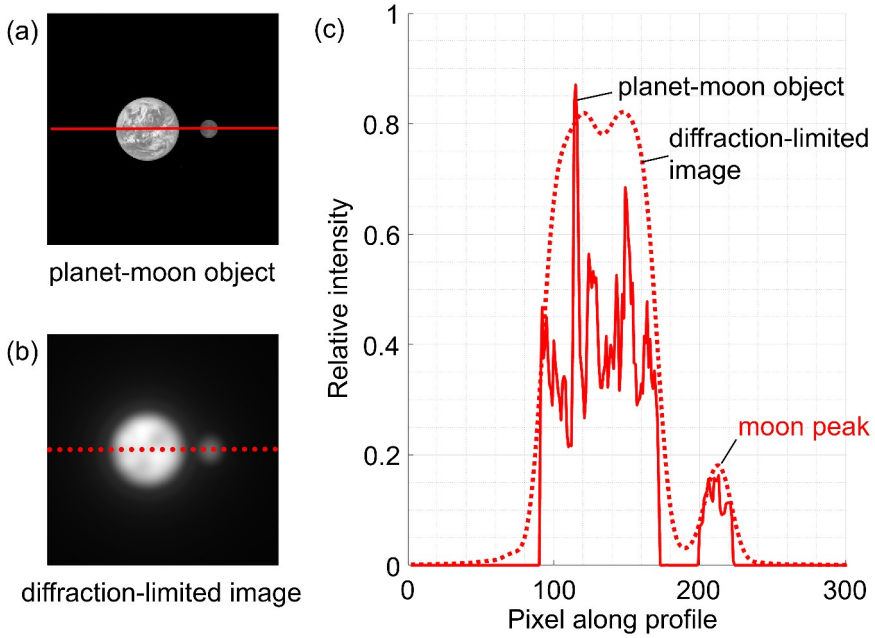

Figure 3.2: (a) The synthetic extended object, comprising a planet and its moon. (b) The simulated diffraction-limited image. The contrast of both images in (a) and (b) has been adjusted with $\gamma = 0.5$ for illustration purposes only. (c) Pixel profiles along the lines of (a) and (b). The high-frequency spatial information of the planet–moon object (solid line) is not transmitted by the system. Nevertheless, the planet and the moon are clearly distinguishable in the diffraction-limited image (dotted line).

3.3. IMAGE-SHARPNESS METRIC

The most common image-sharpness metric is defined as:

$$S_1 \coloneqq \iint I(\mathbf{x})^2 \mathrm{d}\mathbf{x}. \tag{3.1}$$

We found the first references to this metric in Schade [10] and Fellgett [11] for the evaluation of photographic images. We follow the notation of Muller and Buffington who first proposed to use S_1 as a feedback signal in astronomical telescopes to compensate for atmospheric seeing [12]. They used a modified Fresnel–Kirchhoff integral to prove that the global maximum of S_1 is obtained for zero aberration. Hamaker *et al.* offered an alternative proof based on Fourier optics [13]. We first follow Hamaker's line of thought with a different notation. The optical transfer function OTF is the frequency response of

an optical system:

$$\hat{I}(\mathbf{s}) = \mathrm{OTF}(\mathbf{s})\,\hat{O}(\mathbf{s})\,, \tag{3.2}$$

where I and O are the intensity distributions of the image and of the object, respectively, and the symbol $\hat{}$ denotes the Fourier transform. The vector $\mathbf{s}$ denotes the spatial frequency in the 2D frequency domain. Applying Parseval's theorem to Eq. (3.1) and using Eq. (3.2), we get:

$$\begin{aligned} S_1 &:= \iint I(\mathbf{x})^2 \mathrm{d}\mathbf{x} \propto \iint \left|\hat{I}(\mathbf{s})\right|^2 \mathrm{d}\mathbf{s} \\ &\propto \iint \left|\mathrm{OTF}(\mathbf{s})\hat{O}(\mathbf{s})\right|^2 \mathrm{d}\mathbf{s} \propto \iint \mathrm{MTF}(\mathbf{s})^2 \left|\hat{O}(\mathbf{s})\right|^2 \mathrm{d}\mathbf{s}\,, \end{aligned} \tag{3.3}$$

because the modulation transfer function MTF is equal to |OTF|. We use the proportionality symbol $\propto$ to drop any constant multiplication factor. $\left|\hat{O}(\mathbf{s})\right|^2$ is the power spectral density of the spatial frequencies of the object. Hamaker showed that the MTF of an aberrated system for any spatial frequency is always smaller than its diffraction-limited value [13]. This can also be proven by using Schwarz's inequality [14]. Thus, independently of the object, S_1 is maximum for a diffraction-limited system. In this chapter, we further investigate Eq. (3.3) and discuss two aspects: 1. what this equation implicates for an aberrated system and 2. the dependence of S_1 on the power spectral density of the object.

The MTF is zero for frequencies higher than the cutoff frequency s_{cut}. Also, the MTF is an even function symmetric about the origin [3]. Thus, the integration may be restricted to the first quadrant of the frequency domain, and Eq. (3.3) can be written as:

$$S_1 \propto \iint_0^{s_{\mathrm{cut}}} \mathrm{MTF}(\mathbf{s})^2 \left|\hat{O}(\mathbf{s})\right|^2 \mathrm{d}\mathbf{s}\,. \tag{3.4}$$

3.4. BALANCING AN ABERRATED SYSTEM

The power spectral density of a point object is simply $\left|\hat{O}(\mathbf{s})\right|^2 = 1$. The substitution in Eq. (3.4) yields:

$$S_{1,p} \propto \iint_0^{s_{\mathrm{cut}}} \mathrm{MTF}(\mathbf{s})^2 \mathrm{d}\mathbf{s}\,, \tag{3.5}$$

where the subscript p (point) distinguishes it from Eq. (3.4). This equation can be expressed in words as the following:

> When imaging a point object, the image-sharpness metric S_1 is proportional to the volume of the square of the MTF in the first quadrant of the frequency domain.

The Zernike modes are orthogonal with respect to the wavefront variance σ^2, which means that adding a Zernike mode to the wavefront or increasing the amplitude of an

existing Zernike mode will always increase σ^2. As already mentioned, the Strehl ratio S can be calculated from the wavefront variance if the aberration is less than about $\lambda/8$ RMS. Therefore, S is also orthogonal with respect to the Zernike modes near the diffraction-limit.

The situation changes if the aberration is more than $\lambda/8$ RMS. The Maréchal approximation becomes invalid and the Strehl ratio can be multiple-valued for the same wavefront variance [15]. An increase of σ^2 may lead to an increase of S instead of a decrease. This means that if the aberration cannot be fully compensated, the designer or the operator of the optical system may be able to improve the Strehl ratio by inducing further aberration, although this increases the wavefront variance. This technique is called aberration balancing.

To demonstrate aberration balancing with Zernike modes using the image-sharpness metric S_1, we simulate the wavefront for different Zernike modes and calculate the PSF, as described in Section 3.2. From the PSFs we then calculate the merit function (MF) as a negative normalized version of S_1:

$$\mathrm{MF} := -\frac{\iint I(\mathbf{x})^2 \mathrm{d}\mathbf{x}}{\left(\iint I(\mathbf{x})\mathrm{d}\mathbf{x}\right)^2} \iint \mathrm{d}\mathbf{x}. \tag{3.6}$$

This is the opposite of the definition of the structural density factor of an image by Linfoot [16]. The minus sign converts the sharpness maximization to a minimization problem. The merit function of Eq. (3.6) results from dividing S_1 of Eq. (3.1) by the square of the total energy in the image plane, and by multiplying by the area of the image plane. Conservation of energy ensures that the total energy in the image plane remains constant independently of the aberration. This is valid for an infinitely large detector with infinite dynamic range. Due to the finite detector area, the total energy is not constant. It is therefore appropriate to use its square as normalization factor. This normalization can also account for intensity variations and sensitivity fluctuations.

The multiplication by the area of the image plane renders the merit function a dimensionless quantity. After the normalization, MF ≤ 1. MF is worse (maximum for MF = 1) if the intensity distribution is constant, which means that there is no contrast.

The discrete version of the merit function defined in Eq. (3.6) is:

$$\mathrm{MF}_{\mathrm{discrete}} := -\frac{\sum\sum I^2}{(\sum\sum I)^2} N_x N_y, \tag{3.7}$$

where $N_x N_y$ is the image area in pixel^2. The summation occurs over a 1201×1201 pixel grid for the point object. This equation is the same with the definition in Eq. (2.4) of Chapter 2.

We show characteristic results in Fig. 3.3 as color-rendering plots of the merit function. These plots are 2D-cuts in the multi-dimensional Zernike domain, with the color indicating the magnitude of the MF. The global minimum of the merit function is always obtained for zero aberration.

Near the region of the global minimum, the contour lines of the merit function for any pair of Zernike modes are either circles with center at $(0,0)$ [see Fig. 3.3(a)] or ellipses with foci along the Zernike axes and center again at $(0,0)$ [see Figs. 3.3(b) and 3.3(c)]. This

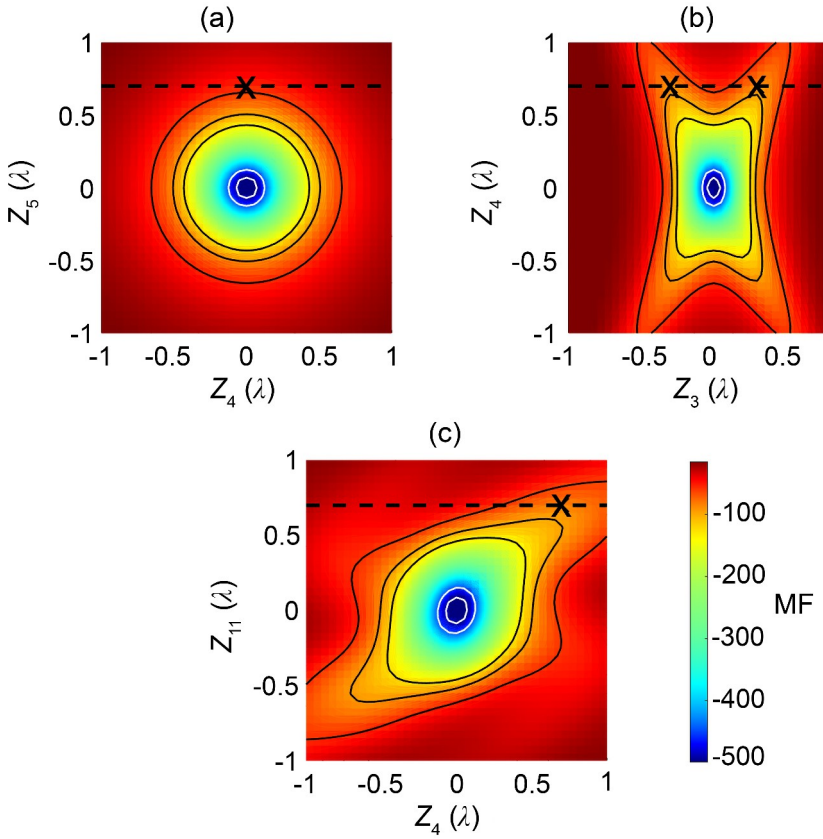

Figure 3.3: Color-rendering plots of the merit function for pairs of Zernike modes when imaging a point object. The white contour lines near the global minimum are always circular or elliptical. The black contour lines for large aberration are circular or elliptical only in (a). (a) The pair Z_4/Z_5. For a constant amplitude of Z_5, MF has a minimum always for $z_4 = 0$ (e.g., the X mark for $z_5 = 0.7\lambda$), and vice versa. (b) The pair Z_3/Z_4. When $|z_4| \geq 0.4\lambda$, MF has two minima for opposite amplitudes of Z_3 (e.g., the two X marks for $z_4 = 0.7\lambda$). (c) The pair Z_4/Z_{11}. When $|z_{11}| \geq 0.25\lambda$, MF has a minimum for a nonzero amplitude of Z_4 (e.g., the X mark for $z_{11} = 0.7\lambda$).

means that the merit function is influenced independently by each Zernike mode, or in other words, that the pairs of Zernike modes are orthogonal to each other with respect to the merit function. Circular contour lines mean that the two Zernike modes have quantitatively the same effect on the merit function, and elliptic contour lines mean that the two Zernike modes have different effect on the merit function. For small aberrations, the Zernike modes are balanced with respect to the Strehl ratio (S), i.e., the effect of each individual Zernike mode on the Strehl ratio is independent of the other Zernike modes [3, 17]. Strehl ratio is a measure of the image quality when imaging a point source. Therefore, it is related to our merit function. According to the Maréchal criterion, the range of small aberrations is defined for Strehl ratio greater than 0.8. For Strehl ratio greater than 0.5 the following approximation is valid: $S \approx \left[1 - 2\pi^2(\sigma/\lambda)^2\right]^2$, where σ is the standard deviation of the wavefront and λ is the wavelength [3].

For the pair of primary astigmatisms Z_4 and Z_5 in Fig. 3.3(a), the contour lines are circular for the whole amplitude range. This is also true for every pair of Zernike modes of the same radial order and opposite azimuthal order, e.g., the two primary comas Z_6/Z_7 , and the two primary trefoils Z_9/Z_{10} (not shown).

For other Zernike pairs, the contour lines may be circular or elliptical only near the global minimum. The color-rendering plots in Figs. 3.3(b) and 3.3(c) show that for the pairs Z_3/Z_4 and Z_4/Z_{11} of sufficiently large amplitudes, the amplitude of one Zernike mode that delivers the minimum merit function depends on the amplitude of the other Zernike mode. For the pair of defocus (Z_3) and astigmatism 0° (Z_4) in Fig. 3.3(b) , we detect an X-shaped valley. When $|z_4| \geq 0.4\lambda$, there exist two local minima of the merit function which are obtained for opposite amplitudes of Z_3. These two defocus Z_3 amplitudes correspond to the two planes of tangential and sagittal focus. Also for the pair of primary astigmatism 0° (Z_4) and secondary astigmatism 0° (Z_{11}) in Fig. 3.3(c), the minimum MF depends on the amplitudes of both Zernike modes. When $|z_{11}| \geq 0.25\lambda$, the minimum merit function value is obtained for a nonzero amplitude of Z_4.

We also calculated the MTF from the PSF. The subsequent calculation of the volume of the square of the MTF in the first quadrant of the frequency domain (not shown) confirmed the results shown in Fig. 3.3 obtained with MF, as expected from Eq. (3.5). Further discussion involving the wavefront, the PSF, and the MTF can be found in [18].

3.5. OBJECT-DEPENDENT ABERRATION BALANCING

Equation (3.4) is the key to understanding aberration balancing and it can be expressed in words as the following:

> The image-sharpness metric S_1 weightens the square of the MTF by the power spectral density of the object, for each spatial frequency. Maximizing S_1, and consequently minimizing the merit function MF of Eq. (3.6), is equivalent to maximizing the weighted volume of $\text{MTF}^2 \left|\hat{O}\right|^2$ in the first quadrant of the frequency domain.

The power spectral density of an extended object is different from that of a point object. This leads to object-dependent aberration balancing. For example, if the object has low power spectral density in a particular range of spatial frequencies, the MTF may be low in this frequency range as well, without severely impacting the merit function.

To demonstrate object-dependent aberration balancing, we use the planet–moon object shown in Fig. 3.2(a) and simulate imaging with different aberrations, as described in Section 3.2. In this case, the summation in the merit function of Eq. (3.7) occurs over a 300×300 pixel grid for the planet–moon object.

Figure 3.4(a) shows the color-rendering plot of the merit function for the Zernike modes of primary astigmatism 0° (Z_4) and secondary astigmatism 0° (Z_{11}) when imaging the planet–moon object. This plot differs from Fig. 3.3(c), because the power spectral density of the planet–moon object differs from that of a point object. The merit function when $z_{11} = 0.7\lambda$ is plotted in Fig. 3.4(b) (black dashed line). It corresponds to the black

dashed line in Fig. 3.4(a). The minimum MF is obtained for $z_4 = 0.6\lambda$. For comparison, we also plot the MF when imaging a point object [red dotted line in Fig. 3.4(b), that corresponds to the black dashed line in Fig. 3.3(c)], which has a minimum for $z_4 = 0.7\lambda$. This clearly demonstrates that, when $z_{11} = 0.7\lambda$, the optimum amplitude of Z_4 depends on the object.

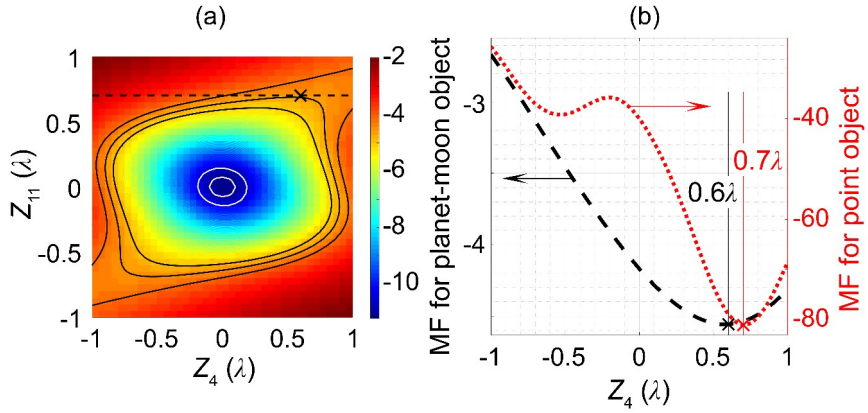

Figure 3.4: (a) Color-rendering plot of the merit function for the pair Z_4/Z_{11}, when imaging the planet–moon object of Fig. 3.2(a). The white contour lines near the global minimum are elliptical. For large aberration the black contour lines are no longer elliptical. (b) The black dashed line plotted against the left y-axis is a cut through the black dashed line in (a) when $z_{11} = 0.7\lambda$. The red dotted line plotted against the right y-axis corresponds to MF when imaging a point object and $z_{11} = 0.7\lambda$. It is a cut through the plot in Fig. 3.3(c). The minima of the two plots (the X marks) are obtained for different amplitudes of Z_4.

In Fig. 3.5, we simulate two aberrated images of the planet–moon object when $z_{11} = 0.7\lambda$. In Fig. 3.5(a), $z_4 = 0$, which corresponds to the best (smallest) wavefront variance. In Fig. 3.5(b), $z_4 = 0.6\lambda$, which corresponds to worse (higher) wavefront variance but to the best (minimum) merit function for uncompensated $z_{11} = 0.7\lambda$ [the X mark of the black dashed line in Fig. 3.4(b)]. Adding primary astigmatism 0° (Z_4) in the presence of secondary astigmatism 0° (Z_{11}) leads to a sharper image. In Fig. 3.5(a), the planet and the moon are indistinguishable. In Fig. 3.5(b), the moon is distinguished from the planet as a small blob. The moon is better identified as a secondary peak in Fig. 3.5(c), which shows the pixel profiles along the red lines of Figs. 3.5(a) and 3.5(b). In addition, structural characteristics of the planet become recognizable in Fig. 3.5(b). These characteristics are clearer in the diffraction-limited image [Fig. 3.2(b)].

Maximizing the MTF for 0.1 s_{cut}, which corresponds to the separation between planet and moon, would lead to a worse (larger) merit function but an even sharper moon peak. However, this would not be appropriate because imaging is about finding something that is not known *a priori*. By minimizing the MF, the moon detection is possible without the preknowledge of its existence.

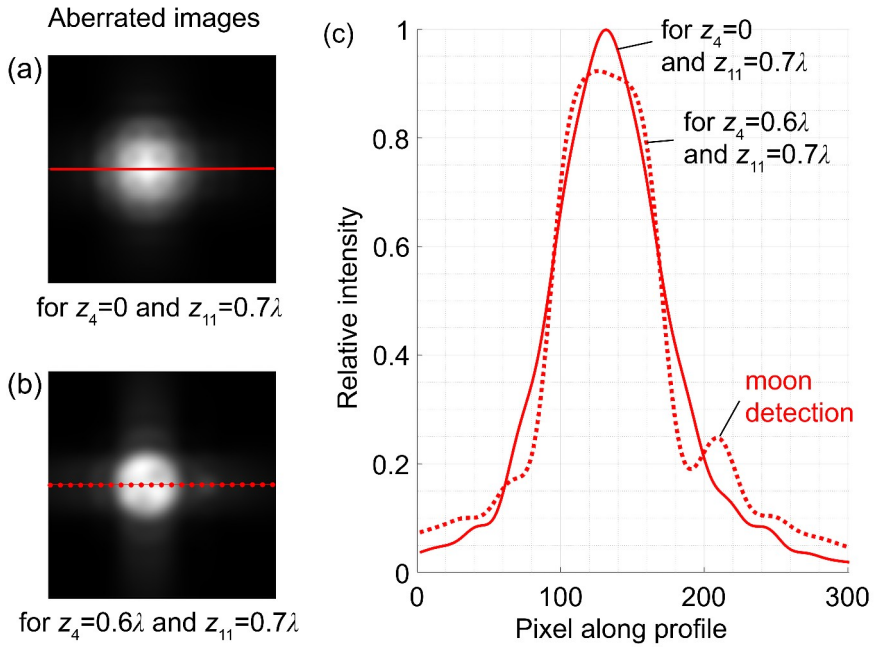

Figure 3.5: Simulated images with 0.7λ of secondary astigmatism 0° (Z_{11}). (a) The amplitudes of all the other Zernike modes are zero. The moon is hidden in the halo of the planet. (b) Adding 0.6λ of primary astigmatism 0° (Z_4), the moon is distinguished from the planet as a small blob. (c) Pixel profiles along the lines of (a) and (b). The moon appears as a secondary intensity peak for the dotted line that corresponds to (b). The image becomes sharper, although the wavefront variance increases by adding Z_4.

3.6. EXPERIMENTAL VERIFICATION

We employ the testbed described in Chapter 2 to test the simulation results. We experimentally use a negative 1951 USAF test target as object. The highest line density of the test target is 228 lp/mm, which should be transmitted by the testbed which has a theoretical cutoff frequency s_{cut} of 290 lp/mm for the wavelength of 633 nm.

To have a close comparison with simulation results, we simulate the incoherent imaging of an extended object, as described in Section 3.2. Our new synthetic object comprises sets of three horizontal and three vertical lines with linewidths of 50 pixels and 20 pixels. The sets of bars with 50 pixels linewidth are rotated by 15° with respect to the object coordinate system. The sets of bars with 20 pixels linewidth are parallel to the object coordinate system and placed near the edges of the object. Thus, we span a wide frequency content in the object. Figure 3.6(a) shows the diffraction-limited image of this extended object. Figure 3.6(b) shows the color-rendering plot of the simulated merit function for the Zernike modes of defocus (Z_3) and spherical aberration (Z_8). The global minimum appears for zero aberration, as expected. An S-shaped valley is detected for $z_8 > 0.4\,\lambda$. This plot is comparable to the one in Fig. 3.4(a), since both show the merit function for Zernike modes of the same azimuthal order and higher radial order [Z_3 and Z_8 in Fig. 3.6(b), Z_4 and Z_{11} in Fig. 3.4(a)].

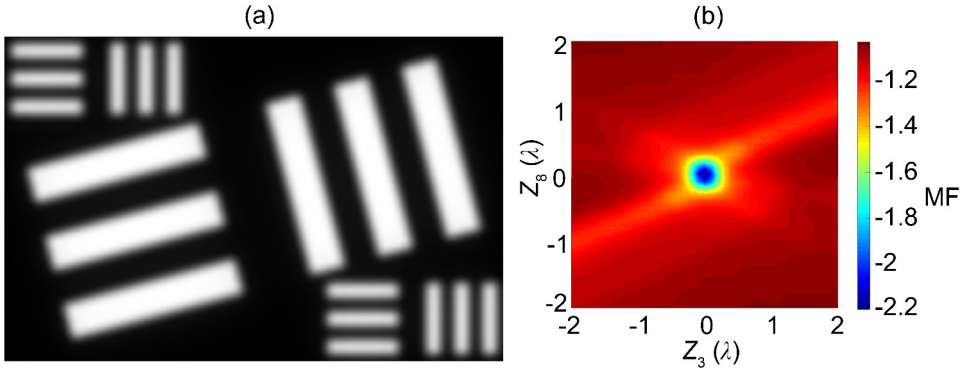

Figure 3.6: (a) The diffraction-limited image of the synthetic extended object used for comparison with the experimental results. This object has sets of three horizontal and three vertical lines with linewidths of 50 pixels and 20 pixels. The contrast is 88% for the bars with 50 pixels linewidth and 64% for the bars with 20 pixels linewidth. The image size is 709 × 461 pixels. (b) Color-rendering plot of the merit function for the pair Z_3/Z_8, when imaging this extended object.

In the experiment, the aberration generator, i.e, the first deformable mirror shown in Fig. 2.1, is kept open-loop flattened. The aberration corrector, i.e., the second deformable mirror, is controlled by selecting a 99-Zernike vector and calculating the voltages via the pseudoinverse of the interferometrically measured influence matrix [19], as described in Section 2.3. There is no simple relation between the optical resolution and the merit function. We find the region of the global minimum by visually ensuring that the highest line density of the test target is resolved (see Fig. 2.2).

Figure 3.7(a) shows cuts through the 2D simulation results of Fig. 3.6(b). When $z_8 = 0.8\,\lambda$, the minimum of the merit function is no longer for $z_3 = 0$, but for $z_3 = 1.4\,\lambda$. The situation is similar for the experimental results, shown in Fig. 3.7(b). When $z_8 = 0.8\,\mu$m, the merit function has two minima, with the global minimum being for $z_3 = 1.9\,\mu$m.

In both the simulation and the experiment, a nonzero value of z_3 delivers the minimum (best) merit function for a sufficiently large value of z_8. This corresponds to the S-shaped valley of the simulated 2D plot of Fig. 3.6(b). The position and the shape of this valley differ between the simulation and the experiment. We control the deformable mirror open-loop by setting its voltages. The piezoelectric hysteresis is compensated open-loop using the Prandtl-Ishlinskii formalism, as described in [20], thus reduced from 15% to 2%. However, the residual, uncompensated hysteresis limits the system performance. Therefore, the real surface of the mirror can deviate from the desired surface. This reduces the repeatability of the merit function and renders the detection of the valley in the merit function difficult. In addition, in the experiment we image the central part of the negative 1951 USAF test target with the elements of groups 6 and 7 (with line densities from 64 lp/mm to 228 lp/mm). Thus, the spatial information of the object differs between the simulation (the diffraction-limited image is shown in Fig. 3.6) and the experiment (an image is shown Fig. 2.2). Further influences for the experimental merit function are the non-normal incidence on the deformable mirror, uncompensated

aberrations, system misalignments, and scenes in the object plane just outside the field stop.

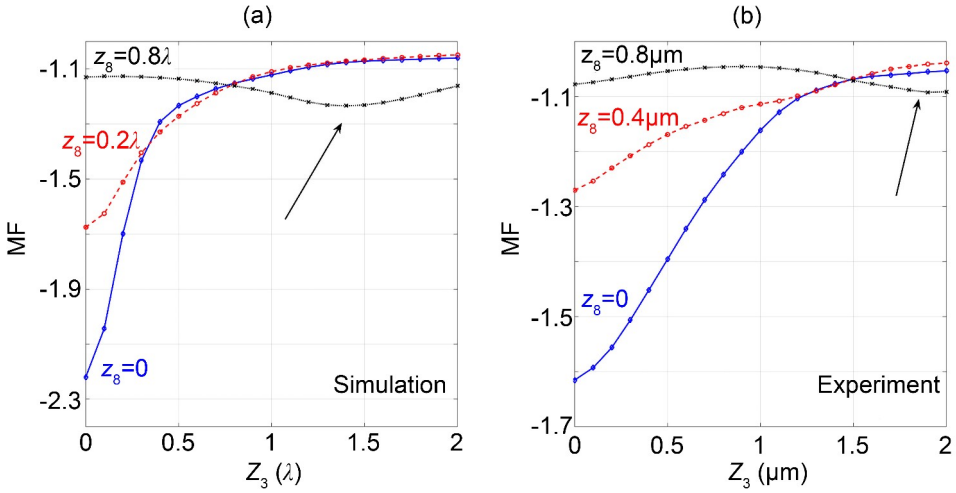

Figure 3.7: The merit function for changing defocus (Z_3) with different values of spherical aberration (Z_8). The arrows in both plots indicate a valley outside the region of the global minimum. (a) Results of numerical simulations, when imaging the artificial extended object whose diffraction-limited image is shown in Fig. 3.6(a). The plots are cuts through the Fig. 3.6(b). (b) Experimental results, when imaging the central part of the negative 1951 USAF test target with the testbed of Fig. 2.1. The step size is 0.1 μm ≈ 0.16 λ.

3.7. CONCLUSIONS

We have demonstrated aberration balancing with Zernike modes using an image-sharpness metric defined as merit function in Eq. (3.6). To date, the term "aberration balancing" has been used to describe the minimization of the wavefront variance by deliberately adding one or more Seidel modes to an aberrated system. Unlike Zernike modes, Seidel modes are not balanced with respect to the wavefront variance. The Zernike modes are orthogonal with respect to our merit function only near the diffraction limit, i.e., for wavefront aberration of less than about $\lambda/8$ RMS. We have shown that for large aberration, the merit function may be improved by adding specific Zernike modes. We also call this effect "aberration balancing," but instead of the wavefront variance, we link it to the minimization of our merit function, i.e., to the maximization of the image-sharpness metric. An experimental demonstration was presented in Section 3.6 for balancing spherical aberration with defocus.

To the best of our knowledge, this is the first study exploring the landscape of an image-sharpness metric away from the global optimum, i.e., in a severely aberrated system. When imaging a point object, the merit function is proportional to the volume of the square of the MTF in the first quadrant of the frequency domain, because the power spectral density of a point object is a constant function. When imaging an extended object, the square of the MTF is weighted by the power spectral density of the object, for each spatial frequency. Therefore, the optimum amplitudes of the additional Zernike

modes depend on the power spectral density of the object, which leads to object-dependent aberration balancing.

Object-dependent aberration balancing is of interest for severely aberrated adaptive and active optics systems, where low-order Zernike modes can partially balance uncorrectable high-order Zernike modes, with amplitudes depending on the object. Using this technique, previously unrecognizable characteristics of the object can become detectable. In the simplified example of Fig. 3.5, inspired by astronomy, a moon that was hidden in the halo of its planet comes into sight.

The image-sharpness metric is calculated from the intensity distribution in the image plane and therefore no additional sensor is required. This also means that this control method is free from non-common path errors, which can affect systems that rely on wavefront sensors.

Our results can be used to immediately improve the performance of wavefront-sensorless adaptive and active optics systems that use the Zernike modes to control the wavefront corrector and have to correct large aberration, i.e., more than $\lambda/8$ RMS. In the simplest case, these systems sequentially optimize the merit function in separate Zernike modes, e.g., in [21]. Figure 3.3 indicates that in the case of large aberration, a single iteration of the Zernike modes is not sufficient to reach the global optimum of this image-sharpness metric. Therefore, the algorithm should be adapted to account for the merit function landscape.

Using this merit function is equivalent to maximizing the power spectral density of the image. Aberration balancing can be also performed using Fourier-based metrics, which allow noise filtering and contrast maximization for a particular range of spatial frequencies.

Spurious resolution, appearing as contrast reversal, leads to decreased MTF for a wide range of spatial frequencies, because the MTF is a continuous function. Our merit function cannot distinguish between positive and negative MTF. Therefore, contrast reversal may lead to a better merit function value. However, this can happen only for objects with unnaturally sharp and narrow peaks in their power spectral density.

REFERENCES

[1] O. Kazasidis, S. Verpoort, and U. Wittrock, *Aberration balancing using an image-sharpness metric,* Journal of the Optical Society of America A **36**, 1418 (2019).

[2] O. Kazasidis, S. Verpoort, and U. Wittrock, *Algorithm design for image-based wavefront control without wavefront sensing,* in *Optical Instrument Science, Technology, and Applications*, Vol. 10695, edited by N. Haverkamp and R. N. Youngworth, International Society for Optics and Photonics (SPIE, 2018) pp. 1 – 10.

[3] C. S. Williams and O. A. Becklund, *Introduction to the Optical Transfer Function* (SPIE Press, Bellingham, Wash., 2002).

[4] V. N. Mahajan, *Aberration Theory Made Simple*, 2nd ed. (SPIE Press, Bellingham, Washington USA, 2011).

[5] J. C. Wyant and K. Creath, *Basic wavefront aberration theory for optical metrology,* in *Applied Optics and Optical Engineering*, Vol. 11, edited by R. R. Shannon and J. C. Wyant (Academic Press, Inc., New York, 1992) Chap. 1.

[6] James Webb Space Telescope User Documentation, *NIRCam Detectors,* [Online] https://jwst-docs.stsci.edu/near-infrared-camera/nircam-instrumentation/nircam-detector-overview (n.d.), Retrieved April 17, 2019; Last accessed August 21, 2020.

[7] NASA, *NASA Captures "EPIC" Earth Image,* [Online] https://www.nasa.gov/image-feature/nasa-captures-epic-earth-image (2015), Retrieved April 17, 2019; Last accessed August 21, 2020.

[8] NASA, *The Near Side of the Moon,* [Online] https://moon.nasa.gov/resources/77/the-near-side-of-the-moon/ (n.d.), Retrieved April 17, 2019; Last accessed August 21, 2020.

[9] NASA, *Moon Fact Sheet,* [Online] https://nssdc.gsfc.nasa.gov/planetary/factsheet/moonfact.html (n.d.), Retrieved April 17, 2019; Last accessed August 21, 2020.

[10] O. H. Schade, *Image Gradation, Graininess and Sharpness in Television and Motion Picture Systems: Part II: The Grain Structure of Motion Picture Images—An Analysis of Deviations and Fluctuations of the Sample Number,* Journal of the Society of Motion Picture and Television Engineers **58**, 181 (1952).

[11] P. Fellgett, *Concerning Photographic Grain, Signal-to-Noise Ratio, and Information,* Journal of the Optical Society of America **43**, 271 (1953).

[12] R. A. Muller and A. Buffington, *Real-time correction of atmospherically degraded telescope images through image sharpening,* Journal of the Optical Society of America **64**, 1200 (1974).

[13] J. P. Hamaker, J. D. O'Sullivan, and J. E. Noordam, *Image sharpness, Fourier optics, and redundant-spacing interferometry,* Journal of the Optical Society of America **67**, 1122 (1977).

[14] J. W. Goodman, *Introduction to Fourier Optics* (McGraw-Hill, 1996).

[15] W. B. King, *Dependence of the Strehl Ratio on the Magnitude of the Variance of the Wave Aberration,* Journal of the Optical Society of America **58**, 655 (1968).

[16] E. H. Linfoot, *Fourier methods in optical image evaluation*, 2nd ed. (The Focal Press, London and New York, 1966).

[17] M. Born and E. Wolf, *Principles of Optics,* (Cambridge University Press, 2005) pp. 522–527, 7th ed.

[18] O. Kazasidis, S. Verpoort, and U. Wittrock, *Image-based wavefront correction for space telescopes,* in *International Conference on Space Optics — ICSO 2018*, Vol. 11180, edited by Z. Sodnik, N. Karafolas, and B. Cugny, International Society for Optics and Photonics (SPIE, 2019) pp. 2854 – 2866.

[19] P. Rausch, S. Verpoort, and U. Wittrock, *Unimorph deformable mirror for space telescopes: design and manufacturing,* Optics Express **23**, 19469 (2015).

[20] P. Krejci and K. Kuhnen, *Inverse control of systems with hysteresis and creep,* IEE Proceedings - Control Theory and Applications **148**, 185 (2001).

[21] S. Bonora and R. J. Zawadzki, *Wavefront sensorless modal deformable mirror correction in adaptive optics: optical coherence tomography,* Optics Letters **38**, 4801 (2013).

4

EXTENDED-IMAGE-BASED CORRECTION OF ABERRATIONS

In this chapter, we design and experimentally test an algorithm for guide-star-free, image-based aberration correction. The algorithm is based on the heuristic hill climbing technique, taking into account the merit function landscape, as explored in Chapter 3. We apply this algorithm in the testbed presented in Chapter 2. We compare the correction in three different domains, namely the voltage domain, the domain of the Zernike modes, and the domain of the singular modes of the deformable mirror. Through our systematic experimental study, we find that successive control in two domains effectively counteracts uncompensated hysteresis of the deformable mirror.

Parts of this chapter have been published in Proceedings of SPIE 10695 (2018) [1] and in Optics Express **26**, 27161–27178 (2018) [2].

4.1. INTRODUCTION

The analysis in Chapter 3 is the basis for the design of the aberration correction algorithm. The algorithm consists of two heuristic routines and is discussed in Section 4.2. We apply this algorithm in the testbed presented in Chapter 2. Section 4.3.1 studies the sensitivity of the merit function near the global minimum with respect to variations of the variables of the three different control domains, i.e., the voltage domain, the Zernike mode domain, and the singular mode domain. In Section 4.3.2, we show the influence of the residual hysteresis of the deformable mirror and demonstrate a combined control scheme that deals with it, accounting for the high dimensionality of the control domains. Section 4.3.3 shows the experimental results of the systematic correction of single Zernike aberrations. In Section 4.3.4, we compare the correction of a random aberration in the Zernike mode domain and in the singular mode domain. Finally, Section 4.4 sums up the experimental results and discusses the advantages of each control domain.

4.2. ABERRATION CORRECTION ALGORITHM

We set an aberrated surface at the aberration generator, i.e, the first deformable mirror shown in Fig. 2.1. The aberration correction algorithm should then find the surface of the aberration corrector, i.e., the second deformable mirror, that delivers the minimum merit function, i.e., that maximizes the image sharpness. Our algorithm uses the heuristic hill climbing technique; or rather, in this case of minimization problem, hill descending. It is a model-free black-box optimization, i.e., the algorithm has no analytic form of the MF in relation to the control variables $\vec{u}$, $\vec{z}$, or $\vec{s}$.

The 2D-cuts of the merit function in the multi-dimensional Zernike space are crucial for the algorithm design, revealing valleys that may slow down or trap the algorithm. The global minimum is for zero aberration. A population-based global search algorithm, such as an evolutionary algorithm, can in principle solve the problem fast and efficient. However, the hysteresis left over after the open-loop compensation, discussed in the previous chapters, leads to low repeatability of the merit function, especially in the steep region of the global minimum. Therefore, the performance of these population-based algorithms in our system is limited. On the other hand, trajectory-based global search algorithms that need large jumps, such as simulated annealing, experience problems, if the actuators have hysteresis.

Our algorithm scans separately each variable, ensuring simple movements inside the search space. We use two routines. The first routine is called *steepest descent in separate variables* and is presented in routine 1 for the case of Zernike modes. This routine first calculates the two-sided univariate differentials of the MF. It then runs a hill descending optimization in the direction of the minimum negative differential, i.e. the steepest descent. When this optimization has converged, this variable is removed from the search space and the routine iterates through the rest of the variables. The steepest descent routine ends when all the variables have been optimized, or when all the two-sided univariate differentials are positive, i.e., the MF of the current point is smaller than the MF of every candidate point.

We select the Zernike mode to be optimized after calculating all the two-sided univariate differentials in order to avoid valleys caused by the nonorthogonality of the

Routine 1 The steepest descent in separate Zernike modes.
N is the number of Zernike modes, $\vec{z}_i$ is the initial point, and $\vec{q}$ is the step size.

procedure STEEPEST DESCENT IN SEPARATE ZERNIKE MODES(N, $\vec{z}_i$, $\vec{q}$)
  define set $E = \{1, ..., N\}$
  $\vec{z}_o = \vec{z}_c = \vec{z}_i$ ▷ optimum, current, and initial point in the Zernike space
  calculate MF($\vec{z}_o$)
  while $E \neq \emptyset$ **do** ▷ Terminate when E is empty
    for $k \in E$ **do** ▷ Find candidate points
      $\vec{z}_{k+} = \left(z_{o,1}, \ldots, z_{o,k} + q_k, \ldots, z_{o,N}\right)$
      $\vec{z}_{k-} = \left(z_{o,1}, \ldots, z_{o,k} - q_k, \ldots, z_{o,N}\right)$
    $\mathrm{MF}(\vec{z}_{k=p}) = \min_k \{\mathrm{MF}(\vec{z}_{k+}), \mathrm{MF}(\vec{z}_{k-})\}$ and $\vec{z}_c = \vec{z}_{k=p}$ ▷ p is the Zernike mode for which the minimum MF among all candidate points is found
    if $\mathrm{MF}(\vec{z}_c) < \mathrm{MF}(\vec{z}_o)$ **then**
      descend hill in Zernike mode p in direction of steepest descent, till no further improvement of MF
      $E = E - p$ and $\vec{z}_o = \vec{z}_c$ ▷ Reduce set of Zernike modes and replace optimum point
    else
      break
  return $\vec{z}_o$, MF($\vec{z}_o$)

Zernike modes with respect to the merit function. Therefore, for example in the case of pure spherical aberration, the algorithm will detect an improvement for changing the defocus, but will prefer changing first the spherical aberration that leads to a larger improvement of the merit function. In the case of large aberrations, the algorithm descends slowly with a zig-zag movement along valleys that are formed for a pair of Zernike modes, e.g., the X-shaped valley for Z_3 and Z_4 shown in Fig. 3.3(b). The algorithm may also be trapped in plateaus if the valley is flattened, or if the step size is not small enough. We can prevent this by first using a global search algorithm to find the valley of the global minimum and then using our steepest descent in separate Zernike modes to detect its exact position.

The second routine is called *cyclic coordinate descent*. In this routine, the MF is also separately minimized with respect to each variable but in a user-defined sequence. The cyclic coordinate descent routine ends when all candidate points of a full cycle have larger MF than the current point.

The first routine needs the two-sided differentials for every variable and chooses the direction of the steepest descent. In the second routine, the user defines the sequence in which the variables are optimized. Therefore, the convergence speed of the second routine strongly depends on the initial point and the variable sequence, and is in general slower than the first routine.

Both routines presented above are deterministic direct local search algorithms. Depending on the MF landscape, the initial point, and the step size, they may get trapped in a local minimum and not return the global minimum. Therefore, in the first experi-

ments of the next section, we study the sensitivity of our MF near the global minimum to detect any other local minima.

4.3. RESULTS AND DISCUSSION

We used as object a negative 1951 USAF test target with an optical density ≥ 6 in the visible. An image captured with our testbed is shown in Fig. 2.2(a). The highest line density of the test target is 228 lp/mm, which should be transmitted by the testbed and is almost equal to its Rayleigh resolution limit (238 lp/mm). We preferred the 1951 USAF pattern over the NBS 1963A pattern because it uses space more efficiently, allowing many spatial frequencies to be in the image simultaneously. The region of interest for the calculation of the merit function is the central part of the image, including the elements of groups 6 and 7, as in Fig. 2.2(b).

4.3.1. MERIT FUNCTION SENSITIVITY

We first studied the sensitivity of the merit function with respect to variations of the variables of the three different control domains (voltage domain, Zernike mode domain, and singular mode domain) of the aberration corrector near the global minimum. For these experiments the aberration generator was open-loop flattened by applying the opposite of its initial surface deformation, which was measured by the phase-shifting interferometer, as described in section 2.3. The global minimum for the aberration corrector was found with a cyclic coordinate descent in the voltage domain, the Zernike mode domain, or the singular modes domain. There is no simple relation between the optical resolution and the merit function of Eq. (2.4). We characterized the region of the global minimum of the MF by visually ensuring that the highest line density of the test target which is near the diffraction-limited resolution limit was resolved. From that initial state, in each experiment one variable was changed stepwise in a predefined range, first increasing to the upper bound, then decreasing to the lower bound, and finally increasing to its initial value. In each step the MF was calculated. Thus, in the resulting 1D-cuts of the MF we can detect possible local minima that may trap a local search algorithm.

We varied the voltages of all 44 actuators by ±20 V from their values at the global minimum of the merit function. This range corresponds to 1/20 of the operational voltage range. The actuators are physically arranged in rings [3]. As can be seen in the inset of Fig. 4.1, the actuator 1 is the inner actuator, the actuators 2 to 9 form the first ring, the actuators 10 to 25 form the second ring, and the actuators 26 to 41 form the third ring, which is outside of the clear aperture of the deformable mirror. Finally, the actuators 42 to 44 are at the outer mounting ring and serve for tip/tilt generation. The voltages of the actuators of the same ring exhibit similar sensitivity. Therefore, only the sensitivity plot for one actuator per ring and all actuators of the outer mounting ring are shown in Fig. 4.1. The MF has a single minimum for U_1 to U_{41}. The sensitivity decreases as we move to the outer rings. Later we discuss the plots for U_{42} to U_{44}.

In the Zernike mode domain, we varied the amplitude of the Zernike modes up to Z_{32} (quaternary astigmatism 45°) in the range of ±1 µm from their values at the global minimum of the merit function. The full sensitivity plot for Z_7 (coma y) is shown in the left side of Fig. 4.2. The MF for decreasing amplitude for each Zernike mode is shown

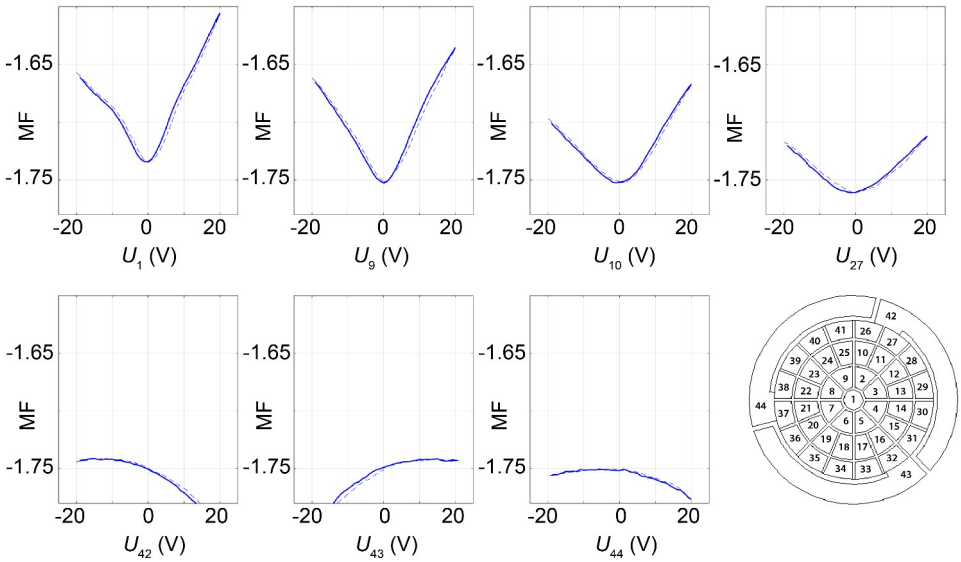

Figure 4.1: The merit function in the voltage domain for the actuators 1, 9, 10, 27, 42, 43, and 44. The plots are centered to the voltage values at the global minimum of the merit function. The solid line corresponds to decreasing amplitude and the dashed line to increasing amplitude. The small difference between the two lines is caused by residual uncompensated hysteresis. The inset at the lower right corner shows the actuator pattern and numbering.

in grayscale in the right side of the figure. The low sensitivity of the MF to image shift is apparent in the rows for Z_1 (tip x) and Z_2 (tilt y).

In the singular mode domain we varied the amplitude of the first 32 singular modes in the range of $\pm 1\mu$m from their values at the global minimum of the merit function. The full sensitivity plot for E_8 is shown in the left side of Fig. 4.3. The MF for decreasing amplitude for each singular mode is shown in grayscale in the right side of the figure. The low sensitivity of the MF to image shift is again apparent in the rows for E_1 and E_2, the first two singular modes which are combinations of tip and tilt, as shown in Fig. 2.4.

We first discuss the influence of image shift. The MF was calculated for the region of interest, defined as a specific part of the CCD. Our MF is insensitive to an image shift on a constant background, but it decreases when the shift moves the image outside the region of interest. The background of our image is not constant and varies spatially, because the nominally black pixels have actually different nonzero values due to limited contrast of the test target, diffraction, and residual aberrations. The MF depends also on the phasing between the image and the CCD pixels, which changes with shift. The above explain the nonconstant sensitivity plots of the MF for U_{42} to U_{44} in Fig. 4.1. The sensitivity plots of the MF for the Zernike modes Z_1 and Z_2, and the singular modes S_1 and S_2 that lead to image shift are also nonconstant, which is not apparent in Figs. 4.2 and 4.3 due to the scaling. Image registration would eliminate the dependence from image shift. However, we do not currently apply it, because of its increased complexity. To minimize the effects of image shift we decouple the correction process from it, excluding the

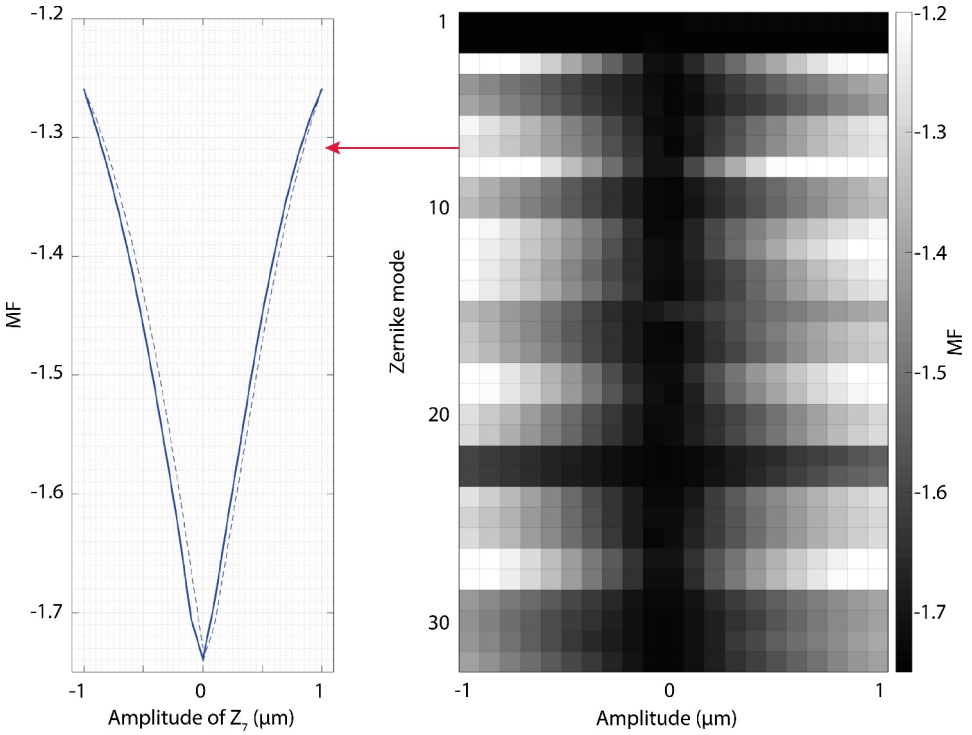

Figure 4.2: The merit function in the Zernike mode domain. Left: The full sensitivity plot for Z_7 (coma y). The solid line corresponds to decreasing amplitude and the dashed line to increasing amplitude. The small difference between the two lines is caused by residual uncompensated hysteresis. Right: The MF for decreasing amplitude from 1 µm to −1 µm in grayscale. Each row of the matrix corresponds to one Zernike mode from Z_1 to Z_{32}.

Zernike modes Z_1 and Z_2, and the singular modes S_1 and S_2 from our algorithm. In the voltage domain, the influence matrix shows that every actuator, except actuator 1, produces image shift. The reason is that all actuators except this one are located off-axis and therefore produce overall tip or tilt. We exclude the voltages $U_{42} - U_{44}$ which contribute almost exclusively to image shift. This procedure conforms with the common practice of image stabilization using a separate tip/tilt mirror, e.g., the fine steering mirror in JWST.

Figures 4.1 to 4.3 show that near the global minimum the 1D-cuts of the merit function exhibit no other local minima and no plateaus. Therefore, our routines presented in section 4.2 are appropriate for the minimization of the MF in all three control domains. In [1] we further studied the merit function landscape, by examining 2D-cuts both numerically and experimentally.

We emphasize the open-loop control of the deformable mirror, as described in section 2.3. The shown voltage values, Zernike mode coefficients, and singular mode coefficients were the inputs of the control system and did not necessarily correspond to the actual mirror state. For the Zernike mode domain in particular, the use of the pseudoinverse $\boldsymbol{CM}$ after truncating the smallest singular values generates a voltage vector $\vec{u}$ that

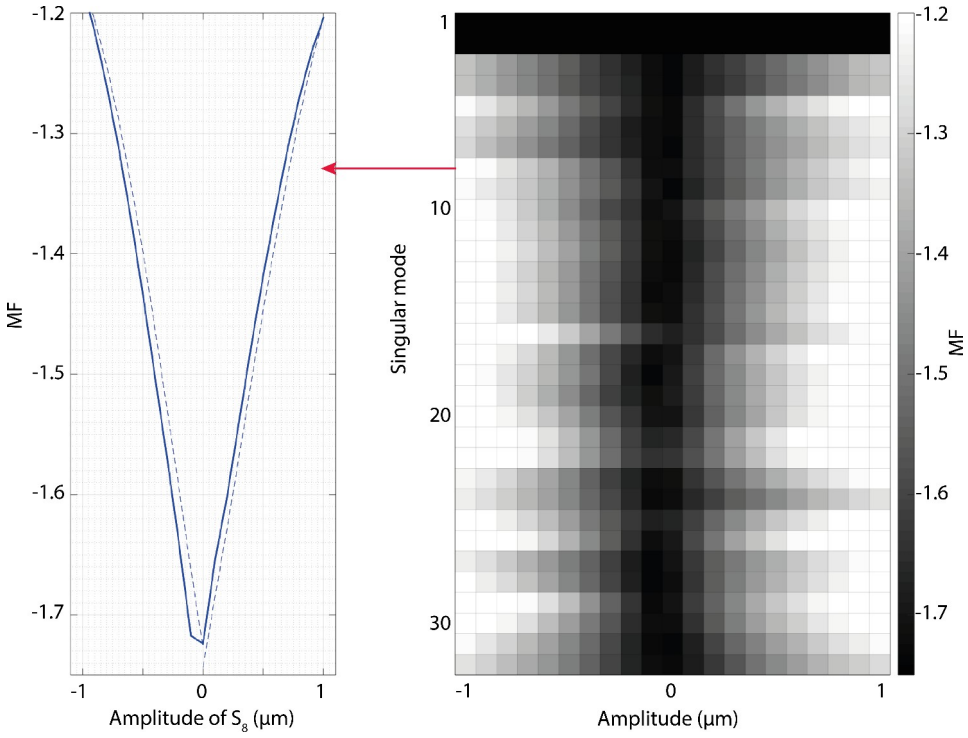

Figure 4.3: The merit function in the singular mode domain. Left: The full sensitivity plot for S_8. The solid line corresponds to decreasing amplitude and the dashed line to increasing amplitude. The small difference between the two lines is caused by residual uncompensated hysteresis. Right: The MF for decreasing amplitude from 1 µm to −1 µm in grayscale. Each row of the matrix corresponds to one singular mode from S_1 to S_{32}. The first 11 singular modes are shown in Fig. 2.4.

corresponds to the least-squares solution for the mirror surface. Therefore, the generated mirror surface in Zernike modes $\vec{z}_{\text{real}} = \boldsymbol{IM}\,\vec{u}$ differs from the desired mirror surface $\vec{z}_{\text{des}}$, and the voltage vector minimizes the residual error $|\boldsymbol{IM}\,\vec{u} - \vec{z}_{\text{des}}|$ [4]. For example, the generation efficiency of the Zernike modes Z_{22} and Z_{23} (tertiary coma x and y, respectively) is just 0.1 (see Fig. 2.3); this leads to the low sensitivity of the MF shown in the corresponding plots in Fig. 4.2.

4.3.2. HYSTERESIS COMPENSATION

The sensitivity plots of the merit function of Figs. 4.1 to 4.3 are at the same time the hysteresis loops of the MF, revealing any residual hysteresis after the open-loop compensation using the Prandtl-Ishlinskii (PI) formalism we mentioned in section 2.3. We quantify the hysteresis by using the 1D-cuts of the merit function near the global minimum. We can use two quantities calculated between the decreasing and the increasing part of the loop: the horizontal shift of the minimum of the MF, and the maximum horizontal opening of the butterfly-like loop. Both quantities are given as ratio with respect to the width of the control variable's range. The loops are rather narrow (maximum hor-

izontal opening of about 2.5%) in the voltage domain, and become slightly wider and more complex for some modes in the Zernike mode domain and in the singular mode domain, because of the concurrent actuation of more than one actuator.

Here we examine the reaction of our algorithm to hysteresis more closely. The left side of Fig. 4.4 shows the sensitivity plots of the MF for the Zernike mode Z_9 (trefoil 0°) with and without the open-loop hysteresis compensation in the range (−2 µm, +2.1 µm) from its value at the global minimum of the merit function. The horizontal shift of the minimum of the MF is 4.9% with the open-loop PI hysteresis compensation, and 17% without the open-loop PI hysteresis compensation. The horizontal shift means that we can counteract the hysteresis by readjusting just the amplitude of the Zernike mode Z_9. The minimum of the MF also shifts vertically. The vertical shift, which is larger without the open-loop PI hysteresis compensation, means that this hysteresis cannot be compensated solely with Z_9. The Zernike modes are orthogonal and the singular modes are orthogonal as well. However, in the presence of hysteresis the voltage patterns that correspond to different Zernike modes are no longer orthogonal and the same holds true for the voltage patterns that correspond to different singular modes. This is obvious because the voltage pattern that creates a certain Zernike mode or singular mode is not unique but depends on the previous state of the mirror. The width of the hysteresis loop and the shift of the minimum of the MF varies among the Zernike modes and depends on the number and the position of the actuated actuators, and on the voltage values. The loop without hysteresis compensation for Z_9 shown in the left side of Fig. 4.4 is the most extreme of all low-order Zernike modes. For Z_4 (astigmatism 0°) we only observed a horizontal shift of the loop. For Z_3 (defocus) and Z_6 (coma x) a relatively small vertical shift was observed.

From the above analysis we deduce that the actuation of a Zernike mode may induce hysteresis that requires other Zernike modes for compensation. Therefore, we cannot significantly reduce the dimensionality of the Zernike mode domain (nor of the singular mode domain) for the aberration correction algorithm. The right side of Fig. 4.4 shows another experiment that further demonstrates the influence of the residual hysteresis on our testbed, which remains after the open-loop PI hysteresis compensation. With the aberration generator open-loop flattened, we found the global minimum of the MF for the aberration corrector with a cyclic coordinate descent in the Zernike mode domain. We then successively set 100 random voltage patterns at the aberration corrector. Such random voltage vectors are used by global search evolutionary algorithms. Finally, we set again the voltages corresponding to the values at the previously found global minimum of the MF. Due to the residual hysteresis, the merit function deviates by approximately 12% from its original minimum. We compensated this deviation by using a cyclic coordinate descent in the Zernike modes Z_3 to Z_5 (defocus and the two primary astigmatisms), followed by another cyclic coordinate descent in voltages. The algorithm in the three low-order Zernike modes Z_3 to Z_5 improved the merit function fast and efficiently by 9%, leaving a 4% deviation from the original minimum. The algorithm in the voltage domain was significantly slower because the voltage search space has a larger dimension than the Zernike mode search space, but converged to a merit function even lower (better) than the original minimum. This is attributed mainly to high spatial frequency deformation that could not be corrected in the Zernike mode domain in the first

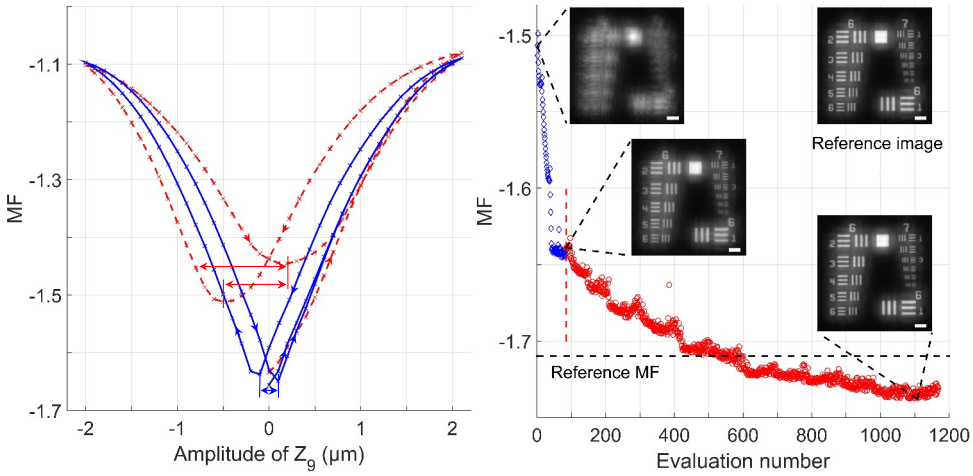

Figure 4.4: Left: Sensitivity plots of the MF for Z_9 (trefoil 0°) with (blue solid line) and without (red dashed line) the open-loop hysteresis compensation. The curves start at $z_9 = 0\,\mu$m, and MF = −1.66 (blue) and MF = −1.63 (red). The horizontal shift of the minimum of the MF is 0.2/4.1=4.9% (blue double-headed arrow) and 0.7/4.1=17% (lower red double-headed arrow), respectively. When the open-loop hysteresis compensation is active, the maximum horizontal opening is equal to the horizontal shift of the minimum, i.e., 4.9% (blue double-headed arrow). When the open-loop hysteresis compensation is inactive, the maximum horizontal opening is 1.0/4.1=24% (upper red double-headed arrow). Right: Compensation of the residual hysteresis with an algorithm in Z_3 to Z_5 (blue diamonds) followed by an algorithm in voltages (red circles). The white horizontal scale bar in the lower right corner of the images is 31 µm long.

search for the minimum. Another, though lesser, influence had the image shift that was discussed in detail in the previous section.

4.3.3. CORRECTION OF ZERNIKE ABERRATIONS

In the next experiments, we show the correction of single Zernike aberrations. Before each experiment, the aberration generator was open-loop flattened and we found the global minimum of the merit function for the aberration corrector, as described in section 4.3.1. An image was taken at this state of the two deformable mirrors and we call this the "reference image." Then, we applied to the aberration generator a single Zernike aberration from the range Z_3 (defocus) to Z_{10} (trefoil 30°) with 1 µm amplitude. Finally, we ran a steepest descent in the Zernike modes Z_3 to Z_{10}, followed by a cyclic coordinate descent in the Zernike modes Z_3 to Z_{32}. The steepest descent corrects the largest part of the aberrations. The cyclic coordinate descent performs the fine-tuning and compensates for residual hysteresis and high-order deformations that cannot be represented by the low-order Zernike modes Z_3 to Z_{10}. The results are summarized in Fig. 4.5. The open-loop, nominally pure single-Zernike aberration produced by the aberration generator was predominantly corrected by the aberration corrector by the same Zernike mode with opposite sign. This mode made up at least 95% of the squared amplitudes of the superposition of Zernike modes that the algorithm produced. The nonzero values of other Zernike modes are attributed to residual hysteresis and errors in the alignment and optical conjugation between the two deformable mirrors. The MF of the corrected images

was up to 55% lower than that of the aberrated images and in very good agreement with the MF of the reference images (2.1% maximum deviation). Only when Z_8 (spherical aberration) had to be corrected there was a 10% residual deviation from the reference image and the test target was not fully resolved. However, there was a 51% improvement from the aberrated image. The generation of Z_8 is expensive in terms of voltage and actuator dynamic range. This led to significant uncompensated hysteresis which included high-order deformation that could not be fully corrected in the Zernike mode domain. We could further improve the MF by using a cyclic coordinate descent in voltages (not shown).

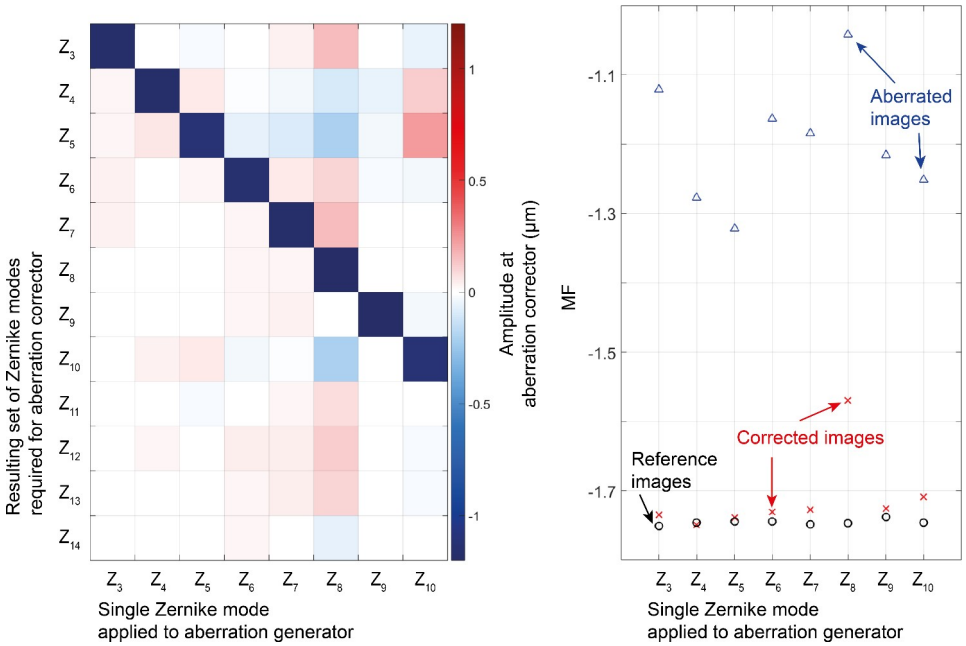

Figure 4.5: The results of the single Zernike aberration experiments of 1 µm amplitude. Left: The output of the correction process in Zernike modes in color code. Each column of the matrix refers to an experiment when a single Zernike aberration was applied to the aberration corrector. Ideally the matrix would be diagonal with all the diagonal elements equal to −1. To save space we do not show the modes Z_{15} to Z_{32}, whose maximum absolute value is 0.1 µm. Right: The merit function of the reference images (black circles), the aberrated images (blue diamonds), and the corrected images (red crosses).

In the next experiment, we set a superposition of Zernike modes at the aberration generator. For the correction we applied two consecutive steepest descents in the Zernike modes Z_3 to Z_{10}, followed by a cyclic coordinate descent in the Zernike modes Z_3 to Z_{32}. In the example shown in Fig. 4.6, we set the aberration vector $\vec{z}_{ab} = -0.8\,\mu\text{m}\,Z_4 + 1.0\,\mu\text{m}\,Z_6 + 0.6\,\mu\text{m}\,Z_9 - 0.5\,\mu\text{m}\,Z_{10}$, i.e., astigmatism 0°, coma x, trefoil 0°, and trefoil 30° with the corresponding amplitudes. The two runs of steepest descent corrected the largest part of the aberrations, improving the MF by 35%. The cyclic coordinate descent fine-tuned the image, further improving the MF by 5.8%. The amplitudes of the Zernike modes of the aberration corrector were almost equal to those of the aberration generator

with opposite sign, as shown in the right plot of Fig. 4.6. The only major exception is Z_5 (astigmatism 45°), whose nonzero value is attributed to hysteresis and system misalignments. The corrected MF was 43% lower (better) than the aberrated MF, and it deviated by 2.6% from that of the reference image (not shown).

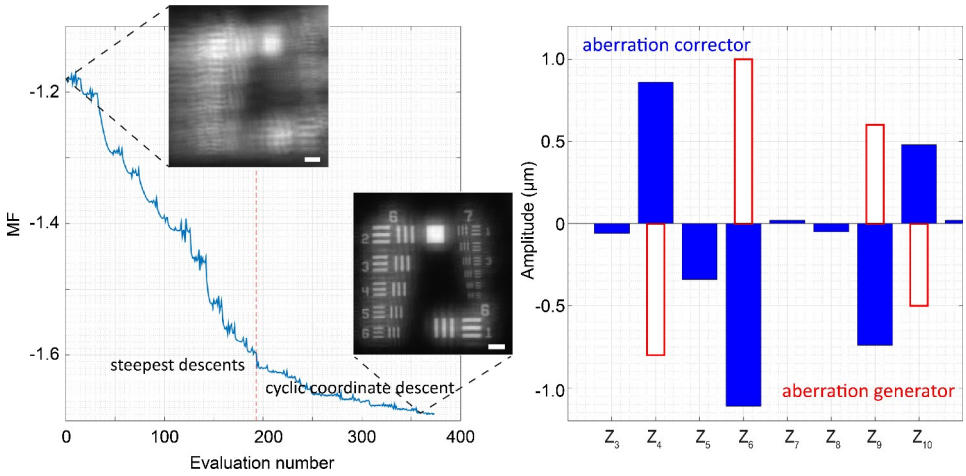

Figure 4.6: Left: Progress of the correction for a combination of Zernike modes. The steepest descents correct fast most of the aberrations and the cyclic coordinate descent fine-tunes the image. The aberrated image and the corrected image are shown. The white horizontal scale bar in the lower right corner of the images is 31 µm long. Right: The coefficient of the Zernike modes for the aberration generator (red unfilled bars) and for the aberration corrector (blue filled bars).

4.3.4. CORRECTION OF ABERRATIONS PRODUCED BY RANDOM VOLTAGES

Here we compare the correction in the Zernike mode domain and in the singular mode domain. As in section 4.3.3, the aberration generator was open-loop flattened before each experiment, the algorithm found the optimum surface for the aberration corrector and a reference image was taken. Then, we added a random voltage vector at the aberration generator to create a superposition of the influence functions. Thus, the initial point of our algorithm was away from the global minimum and we could study the influence of the complexity of the MF landscape on our algorithm. The left plot of Fig. 4.7 shows the voltage values obtained from the uniform random distribution in the interval (−25 V, +25 V). To prevent image shift we used the influence matrix and set the Z_1 (tip x) and Z_2 (tilt y) to zero. In the right plot of Fig. 4.7 we compare the performance of the aberration correction in the Zernike mode domain and in the singular mode domain. In each domain we ran a cyclic coordinate descent for the modes from 3 to 32. The optimum MF obtained in the Zernike mode domain was 16% lower (better) than that of the aberrated image and deviated by 7.7% from that of the reference image (not shown). The optimum MF obtained in the singular mode domain was 24% lower (better) than that of the aberrated image and deviated by just 1.1% from that of the reference image (not shown).

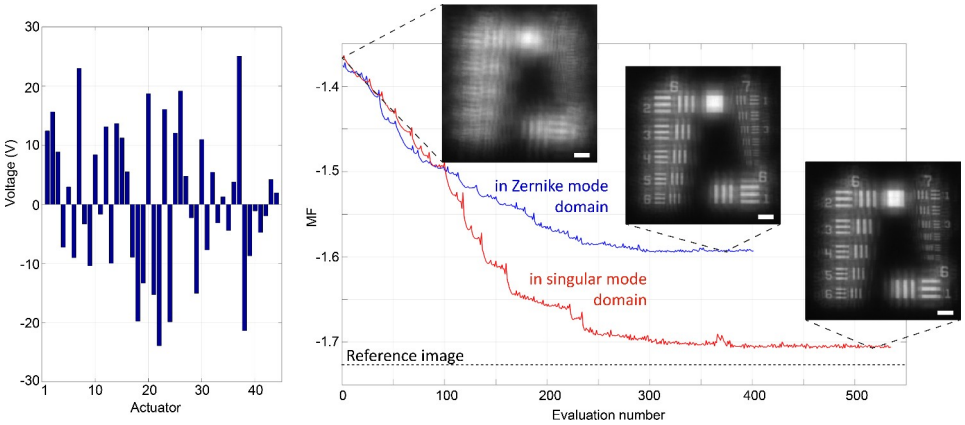

Figure 4.7: Left: The voltages set at the aberration generator, randomly chosen in the interval (−25 V, +25 V). Right: Comparison of the aberration correction in the Zernike mode domain and in the singular modes domain. The correction in the Zernike mode domain requires less evaluations for convergence of the MF, but results in a poorer MF than the correction in the singular mode domain. The white horizontal scale bar in the lower right corner of the images is 31 µm long.

Both the used Zernike mode domain and the singular mode domain have the advantage of reduced dimensionality in comparison to the voltage domain. In the singular mode domain, the selection of the variables and the dimensionality reduction are straightforward. The singular modes contribute to the mirror surface with a gain given by their singular values. Thus, we can select the appropriate singular modes for the correction by inspecting the singular values (see Fig. 2.4) and add modes until we reach the desired accuracy. In the Zernike mode domain, the selection of the variables is not trivial. In this example, we chose all modes up to the Zernike mode Z_{32}. Apparently this was not enough in order to represent the superposition of the influence functions generated by the random voltages of the aberration generator. We can increase the dimensionality of the Zernike mode domain by adding more Zernike modes, at the expense of slower convergence. By intuition we can select only the Zernike modes with high generation efficiency (see Fig. 2.3). However, we thus may still not be able to generate the aberration created by a random voltage vector. There exists no clear indication how many and which Zernike modes we should include in the correction of random aberrations.

On the other hand, there is always the possibility that the algorithm in the Zernike mode domain got trapped in a local minimum. A random voltage vector leads to complex aberrations in the Zernike mode domain and we cannot predict the MF landscape by inspecting the simple 1D-cuts near the global minimum (shown in Figs. 4.1 to 4.3) or even the 2D-cuts (shown in [1]).

4.4. SUMMARY AND CONCLUSIONS

With a view to the next generation of large space telescopes, we designed and built a high-resolution imaging system as testbed for image-based aberration correction. Im-

age-based aberration correction could be an alternative or a complement to wavefront sensing via phase diversity as used by JWST and demonstrated on its testbeds [5, 6].

We reported the results of our systematic experimental study for control in three different domains, namely the voltage domain, the domain of the Zernike modes, and the domain of the singular modes of our deformable mirror. Table 4.1 summarizes the identified advantages of each control domain. The image-sharpness metric applied as merit function has no other local optima near the global optimum, allowing the use of a local search algorithm. We demonstrated a combined control scheme that deals with the residual hysteresis left over by a Prandtl-Ishlinskii compensation and with the high dimensionality of the control domains. Our algorithm corrected aberrations produced by random voltages better when operating in the singular mode domain than in the Zernike mode domain. We used two nominally identical deformable mirrors for aberration generation and aberration correction. This is an idealized, yet in many ways realistic, scenario. The deformable mirror conjugated to the entrance pupil of a large space telescope should be physically designed to compensate for the expected deformation of the primary mirror by matching its singular modes to those of the primary mirror. The required demagnification would in this case restrict the aberration correction to a limited field of view.

Table 4.1: The advantages of each domain for the wavefront-sensorless control of a deformable mirror (DM) with hysteresis in an imaging system.

	Advantages
Voltage domain	- spans the full capability of the DM - directly connected to the hysteresis
Zernike mode domain	- associated with the optical performance - possible, but nontrivial, reduction of search space
Singular mode domain	- connected to the mechanical properties of the DM - possible straightforward reduction of search space

We are currently testing the Data-based Online Nonlinear Extremum-seeker (DONE) algorithm [7] in our testbed for the case of small aberrations. The DONE algorithm was demonstrated for wavefront-sensorless adaptive optics in optical coherence tomography [8] and has already been used with a multi-actuator adaptive lens that suffers from hysteresis [9]. Our control can be further extended by using a model-based approach, e.g., as proposed by Yang *et al.* [10]. Due to the nonlinearities caused by the hysteresis of our deformable mirror, a model-free approach will still be required at the final stage. However, the convergence speed is expected to increase significantly. In addition, other merit functions can be tested, such as the generalized sharpness metrics proposed by Fienup and Miller, which exploit the characteristics of the object [11]. This can become particularly significant in the case of Earth observation, where the sharpness metric can be optimally designed depending on the image type of the application (e.g., urban areas, forests, maritime surveillance). In the current state of our testbed, the deformable mirrors require an external calibration stage for the measurement of their influence functions and the characterization of their hysteresis. A more elaborate wavefront-sensorless approach would be able to calibrate the deformable mirror directly in the testbed,

or in the space telescope after deployment, e.g., by using phase diversity and imaging a well-known target, and thus would not require any direct wavefront measurement.

REFERENCES

[1] O. Kazasidis, S. Verpoort, and U. Wittrock, *Algorithm design for image-based wavefront control without wavefront sensing,* in *Optical Instrument Science, Technology, and Applications*, Vol. 10695, edited by N. Haverkamp and R. N. Youngworth, International Society for Optics and Photonics (SPIE, 2018) pp. 1 – 10.

[2] O. Kazasidis, S. Verpoort, O. Soloviev, G. Vdovin, M. Verhaegen, and U. Wittrock, *Extended-image-based correction of aberrations using a deformable mirror with hysteresis,* Optics Express **26**, 27161 (2018).

[3] S. Verpoort and U. Wittrock, *Actuator patterns for unimorph and bimorph deformable mirrors,* Applied Optics **49**, G37 (2010).

[4] W. H. Press, S. Teukolsky, W. T. Vetterling, and B. P. Flannery, *Numerical Recipes in C: The Art of Scientific Computing* (Cambridge University, 1992).

[5] D. S. Acton, T. Towell, J. Schwenker, J. Swensen, D. Shields, E. Sabatke, L. Klingemann, A. R. Contos, B. Bauer, K. Hansen, P. D. Atcheson, D. Redding, F. Shi, S. Basinger, B. Dean, and L. Burns, *Demonstration of the James Webb Space Telescope commissioning on the JWST testbed telescope,* in *Space Telescopes and Instrumentation I: Optical, Infrared, and Millimeter*, Vol. 6265, edited by J. C. Mather, H. A. MacEwen, and M. W. M. de Graauw, International Society for Optics and Photonics (SPIE, 2006) pp. 215 – 222.

[6] M. D. Perrin, R. Soummer, Élodie Choquet, M. N'Diaye, O. Levecq, C.-P. Lajoie, M. Ygouf, L. Leboulleux, S. Egron, R. Anderson, C. Long, E. Elliott, G. Hartig, L. Pueyo, R. van der Marel, and M. Mountain, *James Webb Space Telescope Optical Simulation Testbed I: overview and first results,* in *Space Telescopes and Instrumentation 2014: Optical, Infrared, and Millimeter Wave*, Vol. 9143, edited by J. M. Oschmann Jr., M. Clampin, G. G. Fazio, and H. A. MacEwen, International Society for Optics and Photonics (SPIE, 2014) pp. 75 – 87.

[7] L. Bliek, H. R. G. W. Verstraete, M. Verhaegen, and S. Wahls, *Online Optimization With Costly and Noisy Measurements Using Random Fourier Expansions,* IEEE Transactions on Neural Networks and Learning Systems **29**, 167 (2018).

[8] H. R. G. W. Verstraete, S. Wahls, J. Kalkman, and M. Verhaegen, *Model-based sensorless wavefront aberration correction in optical coherence tomography,* Optics Letters **40**, 5722 (2015).

[9] H. R. G. W. Verstraete, M. Heisler, M. J. Ju, D. Wahl, L. Bliek, J. Kalkman, S. Bonora, Y. Jian, M. Verhaegen, and M. V. Sarunic, *Wavefront sensorless adaptive optics OCT with the DONE algorithm for in vivo human retinal imaging [Invited],* Biomedical Optics Express **8**, 2261 (2017).

[10] H. Yang, O. Soloviev, and M. Verhaegen, *Model-based wavefront sensorless adaptive optics system for large aberrations and extended objects,* Optics Express **23**, 24587 (2015).

[11] J. R. Fienup and J. J. Miller, *Aberration correction by maximizing generalized sharpness metrics*, Journal of the Optical Society of America A **20**, 609 (2003).

5

SENSOR FOR DYNAMIC FOCUS CONTROL OF A DEFORMABLE MIRROR

The Photonics Laboratory recently presented a novel unimorph deformable mirror which allows for dynamic focus shift with an actuation rate of 2 kHz. Such mirrors suffer from hysteresis and creep. Therefore, they have to be operated in closed-loop. For this purpose, we developed a defocus sensor based on an astigmatic detection system. In this chapter, we present the sensor design and discuss its performance.

Parts of this chapter have been published in Applied Optics **59**, 5625–5630 (2020) [1].

5.1. INTRODUCTION

Conventional focus control relies on moving lenses. A recent innovative concept for laser micromachining employs a galvanometer unit in combination with reflective optics to translate angular movement into focus shift [2]. Adaptive optics (AO) can offer an alternative for dynamic focus control. A deformable mirror with high actuation rate and high defocus stroke would eliminate moving parts and reduce the overall size. We recently presented a novel unimorph deformable mirror that allows for an actuation rate of 2 kHz and produces a focus shift of $\Delta z > 60$ mm using a 250 mm f-theta-lens [3, 4]. The mirror is a highly underdamped system and is oscillating in response to a step impulse. The overshoot and the settling time can be decreased by manipulating the input signal in open-loop. However, piezoelectric creep and hysteresis require closed-loop operation. In the past, we therefore used a chromatic confocal sensor to measure the displacement of the back side of the mirror and fed it back to a PID controller. Now, we present a defocus sensor that can replace the chromatic confocal sensor and open the way towards a commercial fast focus-shifter based on a deformable mirror.

Our defocus sensor is based on the astigmatic method that uses a cylindrical lens and a four-element quadrant photodiode (4-QD) [5]. Astigmatic detection systems are commonly used in optical pickup heads to drive the autofocus servo system. Removing the objective lens, an astigmatic detection system becomes sensitive to curvature instead of displacement. The operation principle of the hybrid curvature and gradient wavefront sensor of Paterson and Dainty [6] is similar to an autofocus servo system.

The standard astigmatic method has a single setpoint. By performing calibration against a known reference, the working range of an astigmatic detection system can be extended. This approach has been already applied for thickness measurement [7] and displacement measurement [8]. In this chapter, we use the same approach for defocus sensing. A 4-QD is placed at the focal plane of a tilted focusing lens, and the acquired signal is calibrated against a reference sensor by fitting a cubic polynomial. We first briefly review the astigmatic method and describe the optical setup for dynamic defocus sensing. Then we discuss the design of our defocus sensor, measure its step response, and perform the calibration. Finally, we test its precision, validate its frequency performance, and comment on its accuracy and noise characteristics.

5.2. ASTIGMATIC METHOD

The astigmatic method is used for real-time autofocus in optical pickup heads. The method is described in detail by Cohen *et al.* in [5]. A collimated laser beam is focused by an objective lens onto a reflective surface. When the surface is at the focal plane of the objective lens, the back-reflected beam is also collimated. Then, a lens focuses this beam onto a detector placed at its focal plane. A displacement of the reflective surface from the focal plane of the objective lens leads to a noncollimated back-reflected beam. In this case, the beam diameter at the detector increases with increasing wavefront curvature, i.e., with increasing displacement of the reflective surface from the focal plane of the objective lens. However, the beam diameter does not give the sign of the wavefront curvature and cannot drive the autofocus servo system. To resolve the ambiguity, a cylindrical lens is placed in the path of the back-reflected beam. The combination of the

cylindrical lens with the focusing lens creates two elongated astigmatic foci with perpendicular orientations. When the reflective surface is in focus, the circular beam profile of the circle of least confusion is detected. The astigmatic foci correspond to opposite displacements. They can be distinguished by using a 4-QD as detector and evaluating the following signal:

$$s_c = \frac{(I_A + I_C) - (I_B + I_D)}{I_A + I_B + I_C + I_D}, \tag{5.1}$$

where I_A, I_B, I_C, and I_D are the currents of the elements of the 4-QD, that are arranged in anticlockwise order, as shown in the insets of Fig. 5.1. The autofocus servo system moves the objective lens in real-time, until the signal of Eq. (5.1) becomes zero, i.e., until the reflective surface is exactly at its focal plane.

If we remove the objective lens and replace the reflective surface by a deformable mirror, the wavefront of the back-reflected beam depends on the curvature of the deformable mirror. This way, the astigmatic method becomes sensitive to curvature instead of displacement. Paterson and Dainty used this principle for their hybrid curvature and gradient wavefront sensor [6] which measures the local curvature of the wavefront in every subaperture of an astigmatic lenslet. That sensor works equivalently to the autofocus servo system, by trying to zero out the signal of Eq. (5.1). Therefore, their sensor is appropriate for closed-loop AO for aberration correction.

The signal of Eq. (5.1) is called position error signal or focusing error signal, in the context of optical pickup heads. We call it curvature signal (s_c) as in [6], deemed more appropriate for our application.

Simulated curvature signals with varying defocus are shown in Fig. 5.1 for three astigmatism values. They all own a characteristic S-shape, being linear at a small range around the focus and becoming nonlinear for a defocus. For a specific range around the focus the curvature signal is a strictly monotonic function of defocus. This range is called the lock-on range and defines the maximum allowed defocus that an autofocus servo system can restore. Outside the lock-on range, the monotonicity of the curvature signal changes, with two different values of defocus leading to the same curvature signal. Due to this ambiguity, the working range of the astigmatic method is restricted to the lock-on range.

As shown in Fig. 5.1, increasing astigmatism leads to wider lock-on range at the cost of lower slope of the curvature signal around zero defocus, i.e., reduced sensitivity.

5.3. EXPERIMENTAL SETUP

Figure 5.2 shows our setup for dynamic defocus sensing. A collimated beam from a 633 nm He–Ne laser is reflected off a unimorph deformable mirror. A commercial chromatic confocal sensor is placed on the backside of the mirror, and measures the displacement of its center. The back-reflected beam is focused onto the center of a 4-QD by a plano-convex lens with a diameter of 2″ and a focal length of 175 mm. The lens is tilted by 23° to induce astigmatism. The astigmatism in the plane of the lens amounts about -21λ, for a plane wavefront of 14 mm diameter, as estimated from ZEMAX. Since the tilted lens creates vertical astigmatism (Z_4 in the used Zernike notation), the 4-QD is rotated by 45°, as shown in the inset of Fig. 5.2. An analog circuit reads out the signals from the 4-QD and manipulates them to produce the curvature signal. For the readout

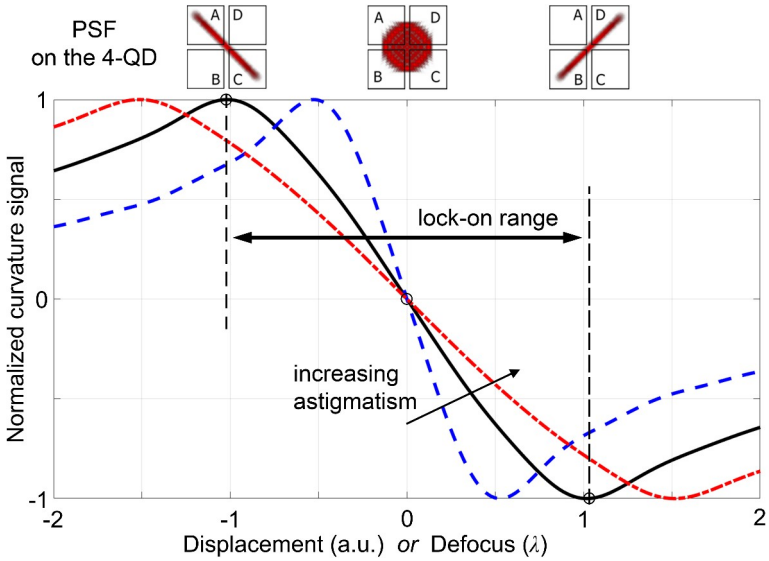

Figure 5.1: Simulated curvature signals for different values of astigmatism 45°, Z_5 using the notation of Wyant and Creath [9], as presented in Section 1.2. The z_5 coefficient is 1λ (blue dashed line), 2λ (black solid line) and 3λ (red dash dot line). The defocus amplitude corresponds to Z_3 in the used Zernike notation. At the top, the PSF is shown in relation to the 4-QD for three defocus values, with constant astigmatism.

of the analog voltages from the chromatic confocal sensor and from our defocus sensor we use a PicoScope 2204A with 8-bit resolution.

The deformable mirror is based on the unimorph mirror technology, which has been developed in the past at the Photonics Laboratory for the correction of aberrations in high-power lasers [10, 11]. The actual deformable mirror has been developed for dynamic focusing in the frame of an industrial project [3, 4]. Its active optical aperture of 14 mm comprises one central actuator, that is used to generate defocus. Eight further actuators in a ring outside the active optical aperture with a width of 6 mm can be used to generate astigmatism. The actuators are driven in the voltage range from −150 V to +150 V. The dielectric HR-coating of the glass substrate has a reflectivity of >99.998% ensuring high power-handling capability.

In this study, we keep all eight actuators of the outer ring grounded and only actuate the central actuator to generate defocus. We couple the actuation of the central actuator with defocus sensing, as measured by the two sensors: our defocus sensor and the chromatic confocal sensor.

5.4. DEFOCUS SENSOR

Our defocus sensor is based on the astigmatic method described in Section 5.2. To the best of our knowledge, this is the first time that the whole lock-on range of the curvature signal is used for defocus sensing. For comparison, the hybrid curvature and gradient wavefront sensor from Paterson and Dainty [6] operates in the approximately linear range around the zero of the curvature signal. The setpoint for a controller using that

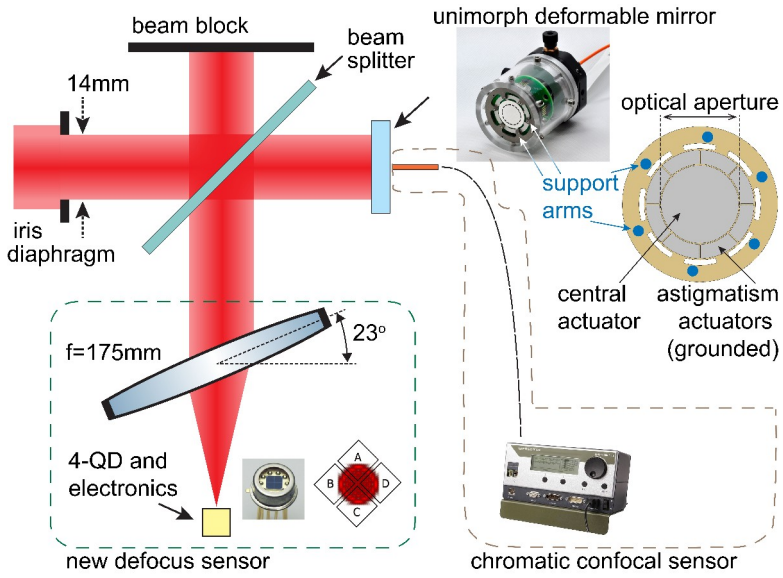

Figure 5.2: Our optical setup for dynamic defocus sensing. The dashed lines enclose the two sensors: our new defocus sensor and the commercial chromatic confocal sensor used for the calibration.

sensor for the feedback signal can take only one value, i.e., for the zero of the curvature signal. Therefore, that sensor is ideal for aberration correction in closed-loop. On the contrary, the specifications for our defocus sensor require a working range instead of a working point. The setpoint for a controller using our sensor can take values from a wide range, each corresponding to a different value of the curvature signal within the lock-on range.

The 4-QD is an off-the-shelf quadrant silicon PIN photodiode with dimensions 3 mm × 3 mm from Hamamatsu [12]. The defocus sensor has to operate at about 10 kHz. Since the bandwidth requirements are relatively moderate, the photodiode is operated in the photovoltaic mode (zero bias) to decrease noise levels. The analog circuit is self-built. The transimpedance amplifier is built around a quad operational amplifier TL074, with gain resistors of 120 kΩ and feedback capacitors of 15 pF, leading to a theoretical cutoff frequency of about 90 kHz. The voltage signals that originate from the four elements of the photodiode are further manipulated to produce a signal proportional to the curvature signal defined in Eq. (5.1). Two summing amplifiers are realized by a dual operational amplifier TL082. The combination of an analog multiplier AD633 and an operational amplifier AD711 in a feedback loop performs the voltage division.

As shown in Fig. 5.1, increasing astigmatism increases the lock-on range. Instead of adding a cylindrical lens, we induce astigmatism by tilting the focusing lens. Apart from astigmatism, the tilting results in additional aberrations, primarily coma. ZEMAX simulations show that these additional aberrations only cause a slight asymmetry in the curvature signal, which is discussed later. The focal length of the focusing lens and the tilt angle are selected based on three criteria. First, the lock-on range of the astigmatic

method should closely match the working range of the deformable mirror. Second, the spot size behind the lens should be large enough for sufficient sensitivity but not exceed the dimensions of the 4-QD. Third, the overall size should be minimum. We found that a focal length of 175 mm and a tilt angle of 23° meet these criteria. The second criterion can be eliminated by producing a 4-QD with the necessary dimensions, should such a defocus sensor become commercialized.

The focusing lens is placed at a distance of 175 mm, equal to one focal length, from the deformable mirror. This way, the waist diameter behind the lens stays constant independently of the mirror defocus. The displacement of the mirror pupil from the lens only has a weak influence on the defocus measurement, as long as the deformable mirror induces only defocus and its distance from the lens is much smaller than the mirror's focal length. Should the focusing lens be placed farther away in the optical path, the deformable mirror should be optically conjugated to the lens. The 4-QD is placed on a linear translation stage to allow focusing, i.e., assigning the zero of the curvature signal to the desired mirror defocus. The kinematic mount of the deformable mirror is adjusted to move the focus spot at the center of the 4-QD. Finally, a 10 nm He–Ne filter in front of the 4-QD eliminates stray light.

5

5.4.1. STEP RESPONSE

By switching the laser on, the step response of our sensor can be measured. In the plot shown in Fig. 5.3, the curvature signal changes from 14.24 V, which is the sensor output for no light, to −1.06 V, which is the curvature signal corresponding to a random mirror defocus. With a sampling rate of about 800 kS/s, we measure a 90%–10% fall time of 19 µs and a settling time of 32 µs, with no oscillation. The step response resembles that of an RC low-pass circuit. Therefore, the cutoff frequency can be calculated as $f_{3dB} \approx$ (0.35/fall time) ≈ 18 kHz, which is sufficient for our application. Our defocus sensor is at least as fast as the values calculated from Fig. 5.3, because we neglected any rise time of the laser power. The achievable bandwidth can be increased by decreasing the feedback capacitance of the transimpedance amplifier and by operating the photodiode in the photoconductive mode (with reverse bias).

5.4.2. CALIBRATION

To characterize the static performance of the deformable mirror, its influence functions are measured with a high-resolution phase-shifting interferometer, and the surface is fitted with 99 Zernike modes using the notation of Wyant and Creath [9], as presented in Section 1.2. Assuming the mirror's response is linear with voltage, the defocus amplitude z_3 per unit voltage is:

$$\frac{\mathrm{d}[z_3]}{\mathrm{d}U} \approx -43.5\,\mathrm{nm/V}, \tag{5.2}$$

where U is the voltage of the central actuator. The RMS deviation from a sphere is calculated to be 0.91 nm/V. For the voltage range from −150 to +150 V, the range of the defocus amplitude is estimated to be ±6.53 µm, and the maximum RMS deviation from a sphere to be 0.14 µm.

The curvature signal inside the lock-on range is a nonlinear function of the defocus (see Fig. 5.1). Therefore, it has to be calibrated against a reference sensor. Our

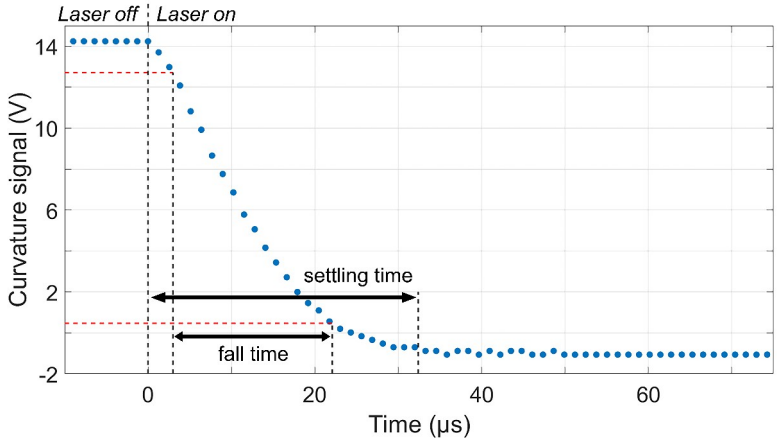

Figure 5.3: Experimentally measured step response of our defocus sensor. No oscillation is observed. The 90%–10% fall time is 19 µs and the settling time is 32 µs.

phase-shifting interferometer is too slow for real-time operation. Therefore, we use the chromatic confocal sensor CHRocodile 2 SE from Precitec [13] as reference sensor. It is placed on the backside of the deformable mirror and measures the displacement h of its center from a reference distance that corresponds to flat mirror, with an axial resolution of <10 nm and a bandwidth of 66 kHz. The calibration against this fast reference sensor allows us to validate the high-frequency performance of our defocus sensor. The calibration could also be performed against a standard wavefront sensor, e.g., a Shack-Hartmann wavefront sensor, with sufficient dynamic range.

The output of the defocus sensor under no illumination is ±14.24 V, which is the saturated output of the voltage division that depends on the supply voltages of the operational amplifiers. The actual maximum and minimum values for the curvature signal depend on the shape of the two elongated astigmatic foci and on the gains of the summing amplifiers. For the calibration, the curvature signal is normalized to its maximum absolute value when the laser is turned on.

To perform the calibration, we actuate only the central actuator at a low actuation frequency (quasi-static operation). Before each voltage step, we try to minimize the hysteresis by erasing the piezoelectric memory of the actuator. At each step, we measure the curvature signal with our defocus sensor and the displacement of the mirror center with the reference sensor. We assign to each measurement the average of 100 samples collected at an interval of 100 µs. As previously discussed, the maximum RMS deviation of the wavefront from a sphere is 0.14 µm when actuating the central actuator. Therefore, to a good approximation, the mirror deformation in its optical aperture is spherical, leading to a linear relation between the displacement of the mirror center h and the defocus amplitude z_3. In our experiments, the electrodes of the outer ring are kept grounded. However, they can also be statically actuated to compensate for the initial surface deformation of the mirror, which is about 20 nm RMS, dominated by primary and secondary astigmatism.

Figure 5.4 shows the results of the calibration experiment. In Fig. 5.4(a), the voltage output of the reference sensor shows a hysteresis of about 4%, an almost six-fold reduction from its original value, when the piezoelectric memory of the central actuator was not erased before each voltage step. The voltage range of $[-10\,\mathrm{V}, 10\,\mathrm{V}]$ for the reference sensor can be linearly translated to the range $[-20\,\mu\mathrm{m}, 20\,\mu\mathrm{m}]$ for the displacement h of the mirror center: $h(\mu\mathrm{m}) = 2\,h(\mathrm{V})$, as defined in the sensor output settings.

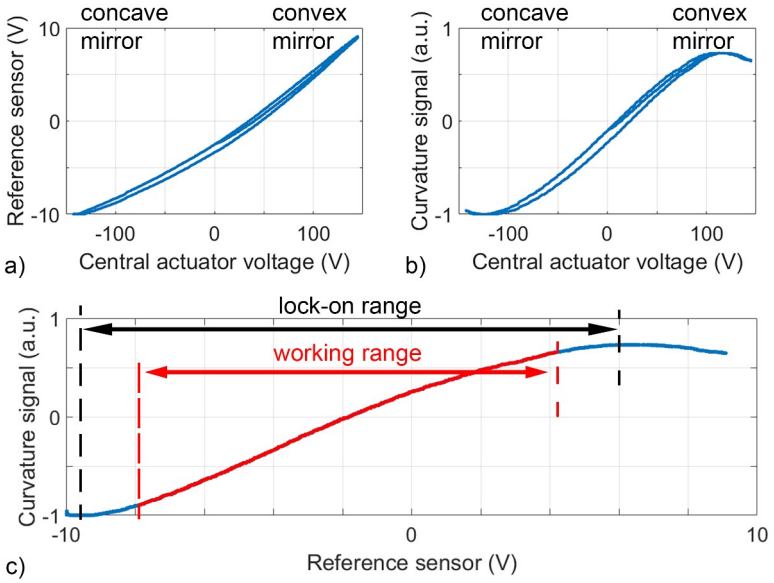

Figure 5.4: (a) and (b) Outputs of the two sensors when the central actuator of the mirror is actuated. (c) The curvature signal as a function of the output of the reference sensor. This curve is used for the calibration of the defocus sensor over its working range (shown in red) which is defined as the inner 90% of the curvature signal range.

From Fig. 5.4(a), the relation between h and the voltage of the central actuator U can be approximated by:

$$\frac{\mathrm{d}[h(\mathrm{V})]}{\mathrm{d}U} \approx 0.068\,\mathrm{V/V}. \tag{5.3}$$

The nonlinearity of the plot in Fig. 5.4(a) is caused by hysteresis. By combining Eqs. (5.2) and (5.3), we come up with an approximate linear relation between the wavefront defocus and h, with slope:

$$\frac{\mathrm{d}[z_3]}{\mathrm{d}[h(\mathrm{V})]} \approx 0.64\,\mu\mathrm{m/V} \approx 1.01\,\lambda/\mathrm{V}. \tag{5.4}$$

In the following, the performance of the defocus sensor is evaluated by h in voltage units, which is measured directly. Equation (5.4) can be used to estimate the corresponding values in terms of wavefront defocus.

Figure 5.4(b) shows the voltage output of our defocus sensor, i.e., the curvature signal, where the hysteresis is also apparent. As verified by ZEMAX simulations, the lens tilting leads to an asymmetry between the two elongated astigmatic foci. This causes the

maximum absolute curvature signal s_c to be larger for a concave mirror, i.e., negative s_c, than for a convex mirror, i.e., positive s_c, and thus leads to an asymmetry as seen in Fig. 5.4(b). However, this asymmetry does not influence the operation of our defocus sensor after the calibration.

In Fig. 5.4(c), the curvature signal is plotted against the output of the reference sensor. This plot can be compared with Fig. 5.1. Assuming that the reference sensor is perfectly linear, the nonlinearity of this curve is only due to the curvature signal. We define the working range of our sensor as the inner 90% of the curvature signal range, which corresponds to about 75% of the lock-on range [shown in red in Fig. 5.4(c)] or a displacement range for the mirror center of about 24 µm. We perform a cubic polynomial regression fit to express the displacement as a function of the curvature signal:

$$h_{\text{fit}}(\text{V}) = 2.2964\, s_c^3 + 2.1327\, s_c^2 + 6.8094\, s_c - 1.8621\,. \tag{5.5}$$

The adjusted coefficient of correlation R^2 of this fit is 99.3%. Combining Eqs. (5.4) and (5.5) the wavefront defocus can be expressed as a function of the curvature signal.

5.4.3. PERFORMANCE

We test the precision of the calibration, by comparing the displacement $h_{\text{fit}}(\text{V})$ calculated from our sensor by the calibration fit of Eq. (5.5), with the displacement $h_{\text{meas}}(\text{V})$ measured by the reference sensor. For each measurement, we again actuate only the central actuator with different voltage steps at a low actuation frequency. The residuals $h_{\text{fit}} - h_{\text{meas}}$ for three repetitions over the whole voltage range of the central actuator are shown in Fig. 5.5. The maximum residual is 114.5 mV. The total RMS error of 41.6 mV is less than one count for the resolution of 78 mV in the voltage range ±10 V of the PicoScope 2204A. The resolution enhancement is due to averaging 100 samples for each measurement. The maximum residual corresponds to less than 1% and the RMS error to less than 0.4% of the sensor working range.

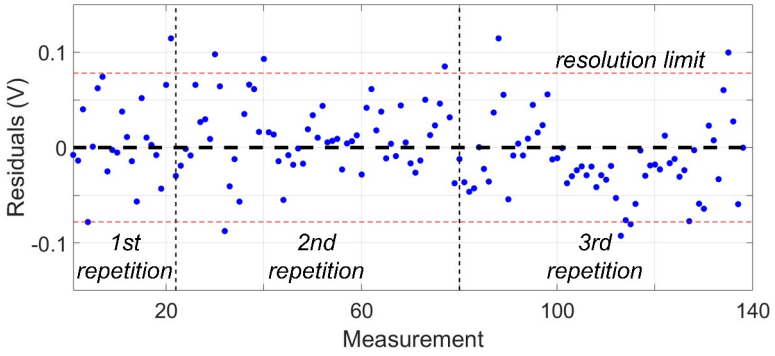

Figure 5.5: Residuals of the calibration for three repetitions. The residuals appear scattered randomly around zero.

Then, we demonstrate the high-frequency performance of our defocus sensor. The deformable mirror is a highly underdamped system. Therefore, we expect that its step response has an oscillating behavior. This is validated in the upper plot of Fig. 5.6 that

shows the outputs of the defocus sensor and the reference sensor, measured at a sampling rate of about 200 kS/s without averaging. The frequency spectra of the sensor outputs shown in the lower plot of Fig. 5.6 are obtained by taking the Fast Fourier Transform (FFT) after applying a Blackman window. The spectra reveal the eigenmodes of the mirror. The spectrum of our defocus sensor strongly resembles that of the reference sensor especially for a frequency up to 4 kHz. The frequencies of the eigenmodes estimated by either sensor coincide. The defocus sensor is noisier, due to additional high-frequency oscillations at about 7.3 kHz and 7.7 kHz, which do not appear in the spectrum of the reference sensor. The source of these oscillations will be studied in the future. A flat-top, Hamming or Gaussian window for the calculation of the FFT all give the same frequencies for the eigenmodes of the mirror. Therefore, their detection is independent of the selection of the window type.

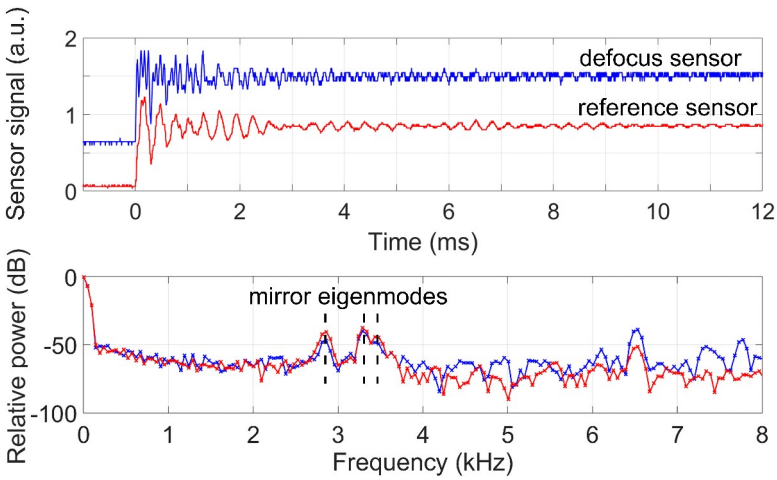

Figure 5.6: Upper: Outputs of the defocus sensor and the reference sensor for step actuation of the mirror. The signals are scaled and transposed in y-axis to increase visibility. Lower: The frequency spectra of the mirror step response as measured by the two sensors reveal eigenmodes of the mirror at 2.86, 3.29, and 3.43 kHz.

Strong oscillations can drive the curvature signal outside the lock-on range of the defocus sensor. Therefore, the overshoot and the oscillating behavior of the mirror step response have to be suppressed. This can be achieved by using a combination of the command shaping and input shaping methods, whose implementation is discussed in detail in [4]. In short, these methods manipulate the input signal of an underdamped system in a way that suppresses the relaxation oscillations.

5.4.4. ACCURACY AND NOISE

The systematic error from the displacement measurement propagates to the curvature signal. If the laser intensity does not change from its value during the calibration, errors due to the photodiode misalignment and nonlinearities due to offset and gain errors of the electronics are eliminated. The systematic error of the displacement measurement is caused by the systematic error of the reference sensor itself, e.g., its linearity error

and pitch error, and by the positioning of the reference sensor, i.e., whether it measures perfectly perpendicularly and exactly at the center of the mirror.

We further investigate the noise of our defocus sensor. For a random mirror defocus, the peak-to-peak voltage of the defocus sensor is 145 mV, with 20.9 mV RMS, measured in the voltage range ±2 V of the PicoScope 2204A. For comparison, under the same measurement conditions the peak-to-peak voltage of the reference sensor is 127 mV, with 16.6 mV RMS. We consider this fluctuation to be white noise, since it has an almost flat frequency spectrum. The peak-to-peak noise for the two sensors differs by just one count for the resolution of 16 mV of the PicoScope in that voltage range. Under a random stepwise mirror actuation, the signal-to-noise ratio of the defocus sensor is 15.64 dB and of the reference sensor is 15.79 dB.

5.5. CONCLUSION

In this chapter, we presented a simple, fast defocus sensor for dynamic focus control of a deformable mirror. The sensor is based on the astigmatic method and its working range can be adjusted to fit the required defocus working range. The sensor requires calibration against a reference sensor.

The sensor meets the performance requirements. In our implementation, it has a bandwidth of at least 18 kHz. Its accuracy depends on the reference sensor, and its precision error is less than 0.4% over its working range, currently limited by the resolution of the measurement device used for the calibration. Its high-frequency performance and noise level are comparable to those of the commercial reference sensor.

Such a defocus sensor opens the way towards an accurate and precise commercial fast focus-shifter based on a deformable mirror.

For a cw-laser, the defocus sensor can be fed with a small percentage of the laser beam, e.g., from the transmittance of an HR mirror, without using the beam splitter shown in Fig. 5.2. Alternatively, the sensing can be realized by using a small coherent laser diode to generate the feedback signal for the closed-loop control of the deformable mirror. In the latter case, the compensation of noncommon path errors between the sensing path and the path of the user laser beam requires an additional calibration method.

Due to the sensor nonlinearity, either the forward calibration model has to be applied in the feedback loop, or the inverse calibration model has to be applied in the reference input. Depending on the bandwidth requirements, the calibration can be implemented by real-time calculation or by a lookup-table. In the case of laser micromachining, an outer feedback loop can validate the proper focusing onto the workpiece and manipulate the reference input for the inner feedback loop, i.e., the setpoint for the deformable mirror defocus.

The used deformable mirror can dynamically adjust defocus and astigmatism, both of which are affected by piezoelectric creep and hysteresis. Although the proposed sensor can effectively track the mirror defocus, a different approach should be developed to allow simultaneous sensing of both mirror defocus generated by the central actuator, and mirror astigmatism generated by the eight actuators of the outer ring. This remains open for future work.

REFERENCES

[1] O. Kazasidis, S. Verpoort, and U. Wittrock, *Sensor for dynamic focus control of a deformable mirror,* Applied Optics **59**, 5625 (2020).

[2] Scanlab, *excelliSHIFT,* [Online] https://www.scanlab.de/en/products/z-axes-3d-add-ons/excelliSHIFT (n.d.), Last accessed August 21, 2020.

[3] A. Brenner, M. Zecherle, S. Verpoort, K. Schuster, C. Schnitzler, M. Kogel-Hollacher, M. Reisacher, and B. Nohn, *Efficient production of design textures on large-format 3D mold tools,* Journal of Laser Applications **32**, 012018 (2020).

[4] S. Verpoort, M. Bittner, and U. Wittrock, *Fast focus-shifter based on a unimorph deformable mirror,* Applied Optics **59**, 6959 (2020).

[5] D. K. Cohen, W. H. Gee, M. Ludeke, and J. Lewkowicz, *Automatic focus control: the astigmatic lens approach,* Applied Optics **23**, 565 (1984).

[6] C. Paterson and J. C. Dainty, *Hybrid curvature and gradient wave-front sensor,* Optics Letters **25**, 1687 (2000).

[7] C.-H. Liu and Z.-H. Li, *Application of the astigmatic method to the thickness measurement of glass substrates,* Applied Optics **47**, 3968 (2008).

[8] W. Hsu, Z. Yu, P. Chen, C. Kuo, and C. Hwang, *Development of the micro displacement measurement system based on astigmatic method,* in *2011 IEEE International Instrumentation and Measurement Technology Conference* (2011) pp. 1–4.

[9] J. C. Wyant and K. Creath, *Basic wavefront aberration theory for optical metrology,* in *Applied Optics and Optical Engineering, vol. 11*, edited by R. R. Shannon and J. C. Wyant (Academic Press, Inc., New York, 1992) Chap. 1.

[10] S. Verpoort and U. Wittrock, *Miniaturized adaptive mirror for solid state laser resonators,* in *Seventh International Workshop on Adaptive Optics for Industry and Medicine* (2009).

[11] S. Verpoort, P. Rausch, and U. Wittrock, *Characterization of a miniaturized unimorph deformable mirror for high power CW-solid state lasers,* in *MEMS Adaptive Optics VI*, Vol. 8253, edited by S. S. Olivier, T. G. Bifano, and J. Kubby, International Society for Optics and Photonics (SPIE, 2012) pp. 67 – 78.

[12] Hamamatsu, *Quadrant Si PIN photodiode S4349,* [Online] https://www.hamamatsu.com/eu/en/product/type/S4349/index.html (n.d.), Last accessed August 21, 2020.

[13] Precitec, *CHRocodile 2 SE,* [Online] https://www.precitec.de/en/products/optical-measuring-technology/chromatic-confocal-sensors/chrocodile-2-s2-se/ (n.d.), Last accessed August 21, 2020.

6

CONCLUSIONS AND RECOMMENDATIONS

This chapter concludes the thesis by summarizing its most important findings and their scientific and technical implications. The last section recognizes limitations of the contributions and proposes future developments.

6.1. CONCLUSIONS

Unimorph deformable mirrors have several features that can be exploited in adaptive and active optics applications, such as scalability, low diffraction losses, and high power-handling capability. Nevertheless, their actuators suffer from piezoelectric hysteresis, which is significantly larger than the hysteretic behavior of most other actuators. In the frame of this thesis, we studied and developed control methods to enhance the performance of adaptive and active optics systems based on unimorph deformable mirrors by reducing the influence of hysteresis, primarily, and of creep. This section is complementary to the conclusion sections of the previous chapters, summarizing their most important findings.

6.1.1. EXTENDED-IMAGE-BASED ABERRATION CORRECTION

Image-sharpness metrics were proposed in the early 1950s to assess the quality of photographic and television images [1, 2]. Since the early days of adaptive optics, such metrics were suggested for image-based aberration correction using a point object or an extended object [3]. However, with the development of more sophisticated methods, such as the phase diversity [4] and other focal plane wavefront sensing techniques, these metrics have more or less fallen into oblivion.

In Chapter 2, we presented the testbed that we built for testing algorithms for image-based aberration correction. In this testbed, a deformable mirror corrected aberrations generated by another deformable mirror at its conjugate plane. This experimental process is an advancement from experiments where the deformable mirror has to correct only a static external aberration or its own random aberration, e.g., as in [5, 6]. It is also a more realistic scenario in comparison to setups where a spatial light modulator (SLM) generates the aberration, e.g., as in [7, 8], because the deformable mirror conjugated to the entrance pupil of a large space telescope should physically match the expected deformation of the primary mirror. In addition, the aberration generated by a nominally identical deformable mirror should in principle be fully correctable.

We extensively studied the most common image-sharpness metric as a merit function for image-based aberration correction. In Chapter 3, we showed how such correction differs from the classical approach of minimizing the wavefront variance. Near the global optimum, i.e., for a diffraction-limited system, the image-sharpness metric is a convex function of the Zernike modes. We showed that this is no longer the case away from the global optimum, i.e., in a severely aberrated system. From the 2D plots of specific pairs of Zernike modes no other local optima or stationary points were detected. Nevertheless, the metric is nonconvex and may be improved by adding specific Zernike modes, i.e., by adding further aberration to the system. We call this effect “aberration balancing” from the namesake effect for the minimization of the wavefront variance.

The sharpness-based aberration balancing is object-dependent, because it depends on the power spectral density of the object. As a result, in a situation where the wavefront corrector cannot produce the required wavefront, image-based and wavefront-free control can find a better solution than wavefront-based methods that measure the aberration and try to compensate it. In the presence of field-dependent aberrations, image-based control can be applied in different image regions and thus achieve optimal performance for different field angles. For example, when trying to resolve a double star,

the region of interest will be a small region of the image. Thus, the active optics should correct a narrow field of view. On the other hand, when observing star clusters and nebulas, a larger image region should be corrected, and the correction should be balanced over a wide field of view. Image-based and wavefront-free control typically requires less optical elements than wavefront-based control, but is slower. However, this is not considered a significant drawback for space active optics, which operate at a bandwidth lower than 0.1 Hz that should align the optical telescope, and correct for constant and slow-changing errors.

These results can improve the performance of wavefront-sensorless adaptive and active optics systems that use the Zernike modes to control the wavefront corrector and have to correct large aberration, i.e., more than $\lambda/8$ RMS. We explained why a single sequential optimization of the image-sharpness metric in separate Zernike modes is not enough to reach the global optimum. The control algorithm should be adapted to account for valleys and plateaus in the merit function landscape. In Chapter 4, we designed such an algorithm based on the heuristic hill climbing technique and used it in our testbed to compare image-based aberration correction in three different control domains, namely the voltage domain, the domain of the Zernike modes, and the domain of the singular modes of the deformable mirror. We showed that the actuation of a Zernike mode may induce hysteresis that requires the actuation of other Zernike modes for compensation. This means that we cannot significantly reduce the dimensionality for control in the Zernike mode domain. We demonstrated a combined control scheme that deals with the residual hysteresis left over by the open-loop compensation and with the high dimensionality of the control domains. Moreover, we experimentally verified and proved the intuition that the control in the domain of the singular modes of the deformable mirror is advantageous for the correction of random aberration in comparison to the domain of the Zernike modes. This result hints against the impetuous use of Zernike modes for any wavefront-sensorless control system. The Zernike modes are arranged in decreasing order of power spectrum, but there exists no clear indication how many and which Zernike modes should be included in the correction of random aberrations. Therefore, the singular modes of the wavefront corrector are a preferable domain, since they are connected with its mechanical properties and offer a straightforward way for dimensionality reduction.

6.1.2. SENSOR FOR DYNAMIC FOCUS CONTROL

In the second part of the thesis, we designed and built a simple and fast defocus sensor. The sensor was presented in Chapter 5. It had a bandwidth higher than 18 kHz and met the performance requirements for dynamically controlling a unimorph deformable mirror that allows for an actuation rate of 2 kHz. The mirror is affected by piezoelectric creep and hysteresis and has to be operated in closed-loop. The sensor's high-frequency performance and noise level were comparable to those of a commercial chromatic confocal sensor. This sensor opens the way towards an accurate and precise commercial fast focus-shifter based on this deformable mirror.

6.2. RECOMMENDATIONS FOR FUTURE WORK

The methods studied and developed in the course of this thesis are by no means self-contained and self-sufficient. This section paves the way forward for implementing these methods in real applications, by summarizing the most important recommendations for future work. This section is also complementary to the conclusion sections of the previous chapters.

6.2.1. EXTENDED-IMAGE-BASED ABERRATION CORRECTION

We studied image-based and wavefront-free control methods under idealized conditions in both simulation and experiment. The robustness of these methods to noise remains to be verified. Our simulations in Chapter 3 have to be repeated using images with random noise. On the other hand, our experiments in Chapters 3 and Chapter 4 were performed with a high-contrast artificial object. Follow-up experiments can make use of a more realistic scene as extended object, i.e., by implementing an OLED display for projecting scenes with various spatial frequency contents and contrast levels. Image-based and wavefront-free control can be combined with image-based wavefront sensing, where first the latter corrects the larger amount of aberrations and then the former performs the fine-tuning.

The James Webb Space Telescope (JWST), currently planned for launch in autumn of 2021, will use imaged-based wavefront sensing. The first relevant techniques were developed in the early 1990s for detecting the wavefront error of the Hubble Space Telescope and designing its corrective optics space telescope axial replacement (COSTAR) instrument [9]. Nevertheless, these techniques will be critical for the successful alignment and the proper operation of the JWST [10]. Although image-sharpness metrics are not planned for the JWST, we argue that they could compliment the wavefront-based control for correcting misalignment and internal errors within each scientific instrument [11]. A more modest but still promising approach would be using image-sharpness metrics to monitor the performance of its Near Infrared Camera (NIRCam), similar to a successful implementation of the Cramér-Rao image-sharpness metric in the astrometric and photometric mission of the Gaia satellite [12]. We consider that such metrics can become an essential part of the active control of segmented mirrors and deformable mirrors in the planned and future large space telescopes.

In our experiments we used two nominally identical deformable mirrors for aberration generation and aberration correction. This is an idealized scenario for the case of a large space telescope, since we neglected the demagnification from the large primary mirror to the small deformable mirror. The required demagnification will restrict the aberration correction to a limited field of view. A formal theoretical and experimental study of any limitations that the image-based and wavefront-free control methods may have in comparison to the wavefront-based ones remains open for future work.

6.2.2. SENSOR FOR DYNAMIC FOCUS CONTROL

The accuracy of the defocus sensor intrinsically depends on its calibration against the reference sensor. Its precision error is currently less than 0.4% over its working range and can be improved by performing the calibration with a higher-resolution measurement device.

The closed-loop control of the deformable mirror using the defocus sensor for the feedback signal remains still to be demonstrated. Depending on the bandwidth requirements, the calibration can be implemented by real-time calculation or by a lookup-table. In principle, strong oscillations can drive the defocus sensor outside its working range. However, prefiltering the actuation signal with the command shaping and the input shaping methods can effectively suppress the overshoot, as discussed in [13]. Thus, the oscillating behavior of the mirror step response is not expected to hinder the sensor's performance.

The used deformable mirror can dynamically adjust astigmatism in addition to defocus. Although the proposed sensor can effectively track the mirror defocus, a different approach should be developed to allow simultaneous sensing of mirror astigmatism alongside defocus. This remains open for future work.

REFERENCES

[1] O. H. Schade, *Image Gradation, Graininess and Sharpness in Television and Motion Picture Systems: Part II: The Grain Structure of Motion Picture Images—An Analysis of Deviations and Fluctuations of the Sample Number,* Journal of the Society of Motion Picture and Television Engineers **58**, 181 (1952).

[2] P. Fellgett, *Concerning Photographic Grain, Signal-to-Noise Ratio, and Information,* Journal of the Optical Society of America **43**, 271 (1953).

[3] R. A. Muller and A. Buffington, *Real-time correction of atmospherically degraded telescope images through image sharpening,* Journal of the Optical Society of America **64**, 1200 (1974).

[4] A. Blanc, L. M. Mugnier, and J. Idier, *Marginal estimation of aberrations and image restoration by use of phase diversity,* Journal of the Optical Society of America A **20**, 1035 (2003).

[5] B. Dong and J. Yu, *Hybrid approach used for extended image-based wavefront sensor-less adaptive optics,* Chinese Optics Letters **13**, 041101 (2015).

[6] T. E. Agbana, H. Yang, O. Soloviev, G. Vdovin, and M. Verhaegen, *Sensorless adaptive optics system based on image second moment measurements,* in *Optics, Photonics and Digital Technologies for Imaging Applications IV*, Vol. 9896, edited by P. Schelkens, T. Ebrahimi, G. Cristóbal, F. Truchetet, and P. Saarikko, International Society for Optics and Photonics (SPIE, 2016) pp. 22 – 30.

[7] L. P. Murray, J. C. Dainty, J. Coignus, and F. Felberer, *Wavefront correction of extended objects through image sharpness maximization,* in *5th International Workshop on Adaptive Optics for Industry and Medicine*, Vol. 6018, edited by W. Jiang, International Society for Optics and Photonics (SPIE, 2006) pp. 369 – 378.

[8] Q. Yang, J. Zhao, M. Wang, and J. Jia, *Wavefront sensorless adaptive optics based on the trust region method,* Optics Letters **40**, 1235 (2015).

[9] J. E. Krist and C. J. Burrows, *Phase-retrieval analysis of pre- and post-repair Hubble Space Telescope images,* Applied Optics **34**, 4951 (1995).

[10] D. S. Acton, J. S. Knight, A. Contos, S. Grimaldi, J. Terry, P. Lightsey, A. Barto, B. League, B. Dean, J. S. Smith, C. Bowers, D. Aronstein, L. Feinberg, W. Hayden, T. Comeau, R. Soummer, E. Elliott, M. Perrin, and C. W. Starr Jr., *Wavefront sensing and controls for the James Webb Space Telescope,* in *Space Telescopes and Instrumentation 2012: Optical, Infrared, and Millimeter Wave*, Vol. 8442, edited by M. C. Clampin, G. G. Fazio, H. A. MacEwen, and J. M. Oschmann Jr., International Society for Optics and Photonics (SPIE, 2012) pp. 877 – 887.

[11] D. S. Acton and J. S. Knight, *Multi-field alignment of the James Webb Space Telescope,* in *Space Telescopes and Instrumentation 2012: Optical, Infrared, and Millimeter Wave*, Vol. 8442, edited by M. C. Clampin, G. G. Fazio, H. A. MacEwen, and J. M. O. Jr., International Society for Optics and Photonics (SPIE, 2012) pp. 1185 – 1192.

[12] A. Mora, M. Biermann, A. Bombrun, J. Boyadjian, F. Chassat, P. Corberand, M. Davidson, D. Doyle, D. Escolar, W. L. M. Gielesen, T. Guilpain, J. Hernandez, V. Kirschner, S. A. Klioner, C. Koeck, B. Laine, L. Lindegren, E. Serpell, P. Tatry, and P. Thoral, *Gaia: focus, straylight and basic angle,* in *Space Telescopes and Instrumentation 2016: Optical, Infrared, and Millimeter Wave*, Vol. 9904, edited by H. A. MacEwen, G. G. Fazio, M. Lystrup, N. Batalha, N. Siegler, and E. C. Tong, International Society for Optics and Photonics (SPIE, 2016) pp. 781 – 797.

[13] S. Verpoort, M. Bittner, and U. Wittrock, *Fast focus-shifter based on a unimorph deformable mirror,* Applied Optics **59**, 6959 (2020).

ACKNOWLEDGEMENTS

Each PhD project may be only one small step for the science as a whole, but it's definitely one huge leap for the researcher themselves. I hope that my work has been at least a small contribution towards the right direction. This time period has been the darkest of my life so far. In retrospect, I recognize that it couldn't have been much different.

First and foremost, I am grateful to my dear Paraskevi for her understanding and empathy during all these years. I am looking forward to the future challenges that we will have to overcome together, using the vital lessons that we've hopefully already learned.

My gratitude goes to my brother Marios for denying conforming to my restrictive norms and for being a wise judge for every step I've made.

I have been blessed for having Koula for mother. Her inherent kindness and holistic world view keep my light on when I am most vulnerable.

I thank my father Stavros, my close family and friends for their support and their kind words. A special thanks to my new friends that have come along the way, especially Sebastian, Abbie, Yria, Spyros, Iris, and Christos. Your arrival brings new meaning and hope to my heart that is fed up with the endless cruelty of the world.

Though it's true that scientists can see further by standing on the shoulders of giants, it's also true that sometimes the giants become an unbearable burden on the shoulders of a scientist. I thank my promotor and mentor Prof. Dr. Ulrich Wittrock from the FH Münster University of Applied Sciences for believing in me and for placing the appropriate amount of weight on my shoulders. I thank my promotor Prof. Dr. Michel Verhaegen for the cooperation and for giving me the chance to work in a multidisciplinary team. My gratefulness to my colleagues in the Photonics Laboratory for support and numerous discussions, namely Dr. Sven Verpoort, Dr. Peter Rausch, Dr. Christian Vorholt, Sinje Leitz, and Torben Fiehler, as well as all current and former members of the group, in particular Agnes Frieling for her tireless commitment and generosity. My thanks to Dr. Gleb Vdovin and Dr. Oleg Soloviev from Delft Centre for Systems and Control for discussion and advice. A special thanks to Dr. Judith Verstegen for the assistance with the Dutch version of the summary.

I gratefully acknowledge financial support from the funding programme for graduate students „*Qualifizierungsstelle*“ of the FH Münster University of Applied Sciences and the STIBET completion grant from the DAAD. I also thank Jasmin Biedermann from the Graduate School of the FH Münster, Mascha Toppenberg from the Graduate School 3mE of the TU Delft, as well as the International Office of the FH Münster.

Immersing into art has always been my refuge for leisure and solace, for pleasure and inspiration. My deep appreciation and eternal gratitude go to all the artists whose works have accompanied me during this journey, particularly – but not exclusively – to Playground Noise, Orestis Ntantos, Electric Litany, Social Waste, Killah P, No Clear Mind,

Queens of the Stone Age, Sufjan Stevens, Vetusta Morla, Pink Floyd, Ólafur Arnalds, Craig Armstrong, Anohni, The Twilight Sad, Hidden Orchestra, Tame Impala, Algiers, Coldplay, Damon Albarn, Edward Sharpe and the Magnetic Zeros, Woodkid, Get Well Soon, Manu Chao, Richard Marx, and Jóhann Jóhannsson. I also thank Marietta Kondou for her inspiring book; I am looking forward to get my hands on its German version. I warmheartedly acknowledge the whole team of Mix Grill for providing a safe space for expression and ideas.

My huge appreciation goes to individuals, groups, movements and organizations that embrace and promote diversity, push for social justice and environmental protection, and fight against racism. Finding modern-day heroes is tough; but they might just be around the corner.

Próxima estación...

Orestis Kazasidis
Münster, September 2020

CURRICULUM VITÆ

Orestis KAZASIDIS

Email orestis.kaza@gmail.com
May 20, 1985 Born in Athens, Greece.

EDUCATION

2021 PhD in Engineering Physics (expected)
Photonics Laboratory, FH Münster University of Applied Sciences, Germany
Cooperating university: Delft University of Technology, The Netherlands
Thesis: *Methods for controlling deformable mirrors with hysteresis*
Main topics: active and adaptive optics, optical system design, image processing, control engineering, mathematical optimization

2014 Master of Science in Photonics
FH Münster University of Applied Sciences, Germany
Thesis: *Interferometric measurement of thermo-optical properties of Pr:YLF laser crystals in the temperature range 20°C–80°C*

2011 Diploma in Electrical and Computer Engineering (Master equivalent)
National Technical University of Athens, Greece
Thesis: *Study of alternations in electroencephalogram during the exposure to electromagnetic signal with third generation characteristics: Computational dosimetry assessment of study with human volunteers*

2003 High school graduation, Athens, Greece

ACHIEVEMENTS / AWARDS

2020 DAAD scholarship, STIBET completion grant, FH Münster University of Applied Sciences, Germany.

2017 Funding programme for graduate students „*Qualifizierungsstelle,*“ FH Münster University of Applied Sciences, Germany.

2011 Scholarship „*Deutschlandstipendium,*“ FH Münster University of Applied Sciences, Germany.

2009 Erasmus scholarship for studying at Barcelona School of Informatics (FIB), National Technical University of Athens, Greece.

2003 Eurobank EFG Award for obtaining the highest University Entrance Examination score in the High School, Athens, Greece.

COMPETENCES

LANGUAGE SKILLS

Greek: Native speaker
English: Fluent–C2, Certificate of Proficiency, University of Cambridge (2000)
Spanish: Fluent–C2, Diploma de Español Nivel Superior (2010)
German: Advanced–C1, DSH 2, University of Münster (2014)
French: Intermediate–C1, Certificat pratique de langue française Paris Sorbonne (2001)
Italian, Catalan: Basic knowledge

COMPUTER SKILLS

Programming languages: MATLAB, Python, HTML, Arduino
Software: LaTeX, Microsoft Office, Zemax, Illustrator, Photoshop, InDesign

LIST OF PUBLICATIONS

JOURNAL PUBLICATIONS

1. **O. Kazasidis** and U. Wittrock, *Interferometric measurement of the temperature coefficient of the refractive index dn/dT and the coefficient of thermal expansion of Pr:YLF laser crystals*, Optics Express 22, 30683-30696 (2014).

2. **O. Kazasidis**, S. Verpoort, O. Soloviev, G. Vdovin, M. Verhaegen, and U. Wittrock, *Extended-image-based correction of aberrations using a deformable mirror with hysteresis*, Optics Express 26, 27161-27178 (2018).

3. **O. Kazasidis**, S. Verpoort, and U. Wittrock, *Aberration balancing using an image-sharpness metric*, Journal of the Optical Society of America A 36, 1418-1422 (2019).

4. **O. Kazasidis**, S. Verpoort, and U. Wittrock, *Sensor for dynamic focus control of a deformable mirror*, Applied Optics **59**, 5625 (2020).

CONFERENCE PROCEEDINGS

1. M. Christopoulou, **O. Kazasidis**, and K. S. Nikita, *Numerical Assessment of EEG Electrode Artifacts during EMF Exposure in Human Provocation Studies*, 2nd International ICST Conference on Wireless Mobile Communication and Healthcare (MobiHealth 2011), Lecture Notes of the Institute for Computer Sciences, Social Informatics and Telecommunications Engineering, vol 83. Springer, Berlin, Heidelberg (2012).

2. **O. Kazasidis** and U. Wittrock, *Simultaneous interferometric measurement of the temperature coefficient of the refractive index dn/dT and the coefficient of thermal expansion of laser crystals*, paper CE-7.5, European Conference on Lasers and Electro-Optics (CLEO Europe) (2015).

3. **O. Kazasidis**, S. Verpoort, and U. Wittrock, *Algorithm design for image-based wavefront control without wavefront sensing*, Proceedings of SPIE 10695, Optical Instrument Science, Technology, and Applications, 1069502 (2018).

4. **O. Kazasidis**, S. Verpoort, and U. Wittrock, *Image-based wavefront correction for space telescopes*, Proceedings of SPIE 11180, International Conference on Space Optics — ICSO 2018; 111807Z (2019).

5. **O. Kazasidis**, S. Verpoort, and U. Wittrock, *Fast focus and astigmatism control*, 12th Workshop on Adaptive Optics for Industry and Medicine (2019).